BRNO UNIVERSITY OF TECHNOLOGY
VYSOKÉ UČENÍ TECHNICKÉ V BRNĚ

FACULTY OF MECHANICAL ENGINEERING
FAKULTA STROJNÍHO INŽENÝRSTVÍ

INSTITUTE OF PHYSICAL ENGINEERING
ÚSTAV FYZIKÁLNÍHO INŽENÝRSTVÍ

SPIN WAVE EXCITATION AND PROPAGATION IN MAGNONIC CRYSTALS PREPARED BY FOCUSED ION BEAM DIRECT WRITING
EXCITACE A ŠÍŘENÍ SPINOVÝCH VLN V MAGNONICKÝCH KRYSTALECH PŘIPRAVENÝCH PŘÍMÝM ZÁPISEM FOKUSOVANÝM IONTOVÝM SVAZKEM

MASTER'S THESIS
DIPLOMOVÁ PRÁCE

AUTHOR AUTOR PRÁCE	**Bc. Viola Křižáková**
SUPERVISOR VEDOUCÍ PRÁCE	**Ing. Michal Urbánek, Ph.D.**

BRNO 2018

BRNO UNIVERSITY OF TECHNOLOGY
FACULTY OF MECHANICAL ENGINEERING

Master's Thesis Assignment

Institut:	Institute of Physical Engineering
Student:	**Bc. Viola Křižáková**
Degree programm:	Applied Sciences in Engineering
Branch:	Physical Engineering and Nanotechnology
Supervisor:	**Ing. Michal Urbánek, Ph.D.**
Academic year:	2017/18

As provided for by the Act No. 111/98 Coll. on higher education institutions and the BUT Study and Examination Regulations, the director of the Institute hereby assigns the following topic of Master's Thesis:

Spin wave excitation and propagation in magnonic crystals prepared by focused ion beam direct writing

Brief description:

Magnonic crystals represent a new class of metamaterials with periodically modulated magnetic properties. Similarly, to the propagation of electromagnetic waves in photonic crystals the propagation of collective spin waves in magnonic crystals is subject to the existence of allowed frequency ranges, alternated with forbidden band gaps additionally tunable by external magnetic fields. Magnonics offers great opportunity to design and exploit a new generation of spin logic devices, filters, and waveguides operating in the GHz frequency range.
Metastable face-centered cubic Fe thin films are good templates for fabrication of magnonic crystals, because they are nonmagnetic at room temperature and nanometer patterns can be transformed by focused ion-beam irradiation to ferromagnetic body-centered cubic Fe.

Master's Thesis goals:

- Perform a literature search and describe the current state of the art in the field of magnonic materials and magnonic crystals.
- Perform a research study on the preparation of metastable fcc FeNi thin films.
- Prepare metastable FeNi thin films on different substrates.
- Measure magnetic and magnetodynamic properties of prepared thin films and compare them with other materials commonly used for magnonic structures (e.g. permalloy).
- Fabricate magnonic crystals from metastable FeNi films by focused ion beam direct writing together with a suitable spin wave source.
- Perform an experimental study of spin wave propagation in the fabricated crystals.

Recommended bibliography:

CHUMAK, A. V. et al., Magnon spintronics. Nat. Phys., 11 (2015).

NEUSSER, S., SpinWaves in Antidot Lattices: From Quantization to Magnonic Crystals. Technische Universität München (2011) [Doctoral thesis].

CHUMAK, A. V., SERGA, A. A., HILLEBRANS, B., Magnonic crystals for data processing J. Phys. D Appl. Phys 50 (2017).

DEMIDOV, V. E. et al. Excitation of coherent propagating spin waves by pure spin currents. Nat. Commun., 7 (2016).

Students are required to submit the thesis within the deadlines stated in the schedule of the academic year 2017/18.

In Brno, 8. 11. 2017

DĚKANÁT
L. S.
⑪

prof. RNDr. Tomáš Šikola, CSc.
Director of the Institute

doc. Ing. Jaroslav Katolický, Ph.D.
FME dean

Abstract

Paramagnetic Ni-stabilized fcc Fe thin films epitaxially grown on Cu(100) are known for their capability to undergo ion-beam-induced phase transformation into ferromagnetic bcc phase. To bring these metastable films closer to the application, a Cu(100) substrate can be further substituted by Si(100) with a Cu(100) buffer layer. With the use of a focused ion beam, magnetic properties of the films can be locally tailored and modulated. Moreover, this alternative approach to the preparation of media suitable for spin-wave guidance provides patterning possibilities unattainable by conventional lithography techniques. Magnetic structures prepared in this way are studied by all-electrical spin-wave spectroscopy. This thesis covers the entire process from the metastable thin film growth, through the patterning, to structural studies and static and dynamic magnetic characterization. A broadband ferromagnetic resonance and propagating spin wave spectroscopy experiments are performed on focused-ion-beam-transformed continuous layers and microstructures. Microscale coplanar waveguides are used for inductive excitation and detection of spin waves with defined wavevectors. Magnetic properties such as saturation magnetization and damping are extracted from the ferromagnetic resonance measurements and characteristics of the propagating modes such as spin-wave decay length or group velocity are studied and compared with common ferromagnetic materials.

Abstrakt

Paramagnetické niklem stabilizované tenké vrstvy plošně centrovaného kubického Fe, epitaxně narostené na monokrystalickém substrátu Cu(100) jsou známy svou schopností strukturní a magnetické fázové přeměny při ozáření iontovým svazkem, a to do prostorově centrované kubické struktury charakteristické feromagnetickými vlastnostmi. Monokrystalický Cu(100) substrát je možné také nahradit Si(100) s mezivrstvou Cu(100). Pomocí fokusovaného iontového svazku lze dále snadno lokálně modifikovat magnetické vlastnosti ozařované vrstvy. Tato metoda přímého zápisu magnetických struktur je alternativou k běžným litografickým technikám, nabízející nové jimi nedosažitelné možnosti. Připravené magnetické struktury následně využíváme k propagaci spinových vln. V práci je představen celý proces od růstu vrstev, přes přípravu mikrostruktur, až po studium jejich struktury a statických i dynamických magnetických vlastností. S využitím vektorového síťového analyzátoru studujeme ve vrstvách a v mikrostrukturách připravených fokusovaným iontovým svazkem feromagnetickou rezonanci a propagující se spinové vlny. Zdrojem spinových vln o definovaných vlnových vektorech jsou litograficky připravené koplanární vlnovody, sloužící také k induktivní detekci vln. Pomocí feromagnetické rezonance kvantitativně určujeme materiálové charakteristiky jako jsou saturační magnetizace a parametr útlumu a ze spekter propagujících módů následně určujeme charakteristiky spinových vln, které porovnáváme s dalšími feromagnetickými materiály.

Keywords

magnonics, spin wave excitation and detection, ferromagnetic resonance, propagating spin-wave spectroscopy, metastable thin films, magnetic phase transformation

Klíčová slova

magnonika, excitace a detekce spinových vln, feromagnetická rezonance, spektroskopie propagujících se spinových vln, metastabilní tenké vrstvy, magnetická fázová přeměna

KŘIŽÁKOVÁ, V. *Spin wave excitation and propagation in magnonic crystals prepared by focused ion beam direct writing.* Brno: Brno University of Technology, Faculty of Mechanical Engineering, 2018. 83 s. Supervised by Ing. Michal Urbánek, Ph.D.

I hereby declare that I have written my master's thesis on the theme of *Spin wave excitation and propagation in magnonic crystal prepared by focused ion beam direct writing* independently, under the guidance of the master's thesis supervisor, Ing. Michal Urbánek, Ph.D., and using the technical literature and other sources of information which are all properly quoted in the thesis and detailed in the list of literature at the end of the thesis.

Bc. Viola Křižáková

I would like to express my gratitude to those people whose guidance, support, shared experience, advice and other contributions were essential during this work. I wish to express my sincere gratitude to:

Ing. Michal Urbánek, Ph.D., who has been my supervisor, for his guidance, inspiring ideas, his patience and interest, and for his comments to the text.

Ing. Jonáš Gloss, who introduced me to the practice of the UHV and who prepared many samples which were crucial for the work. He has been both great colleague and teacher, who shared with me his experience with the metastable thin film preparation.

Ing. Lukáš Flajšman, especially for his advice and many inspiring ideas, but also for the technical support, and for the great contribution to the magneto-structural and the anisotropy studies.

Ondřej Wojewoda, for the calculations on magnonic crystals and related discussions, and for his help with the software. His enthusiasm and his constant efford to help were a great support.

Ing. Igor Turčan, for his support during my first attempts at the waveguide preparation, for his concern, and for his shared experience with the spin-wave spectroscopy.

Dr. Ing. Michal Staňo, for initial introducing me to the group and to magnetism, and for proof-reading of the text.

Ing. Marek Vaňatka, for his valuable advice and discussions on lithography techniques.

Bc. David Pokorný, for preparation of the samples.

Bc. Štěpán Kovařík, for his help and valuable suggestions relevant to all kinds of problems I encountered in the laboratory, and even more importantly, for being a great support to me in many aspects.

My parents and my family

Bc. Viola Křižáková

Financial support from the Thermo Fisher Scientific is gratefully acknowledged.

Part of the work was carried out with the support of CEITEC Nano Research Infrastructure (ID LM2015041, MEYS CR, 2016–2019), CEITEC Brno University of Technology.

Contents

Introduction **3**

1 Spin waves in thin magnetic films and periodic media **5**

1.1 Introduction to magnonics 5
  1.1.1 Motivation 6
  1.1.2 Spin-wave excitation and detection 6
  1.1.3 Materials for magnonic application 7
  1.1.4 Magnonic devices 8
1.2 Theoretical background 9
  1.2.1 Energy formulation of ferromagnetism 9
  1.2.2 Magnetization dynamics 12
  1.2.3 Spin waves 14
1.3 Magnonic crystals 17
1.4 All-electrical spin-wave spectroscopy 20
  1.4.1 Vector network analyzer 20
  1.4.2 Microwave excitation and detection 21
  1.4.3 Scattering parameters 23
  1.4.4 Broadband ferromagnetic resonance technique 24
  1.4.5 Propagating spin-wave spectroscopy 25

2 Metastable FeNi thin film preparation in ultra-high vacuum **26**

2.1 Introduction to ultra-high vacuum techniques 26
  2.1.1 Epitaxial growth 27
  2.1.2 Low energy electron diffraction 28
  2.1.3 X-ray photoelectron spectroscopy 28
2.2 Epitaxial iron films on copper 29
  2.2.1 Metastable thin iron films 29
  2.2.2 Stabilization of paramagnetic phase 30
  2.2.3 Transformation by ion beam irradiation 31
2.3 Preparation of FeNi films on different substrates 33
  2.3.1 Copper single crystal 33
  2.3.2 Hydrogen-terminated silicon 34
  2.3.3 Perovskite oxides and diamond 40

3 Preparation of spin wave source and propagation media **42**

3.1 Ion beam direct writing 42
3.2 Thin films pre-characterization 43
  3.2.1 Transformation efficiency 43
  3.2.2 Morphology of the thin films 47
  3.2.3 The effect of anisotropy 48
3.3 Sources and detectors nanofabrication 50
  3.3.1 Prepared waveguides 52
3.4 Experimental setup 53

4 Experimental results and discussion 56
4.1 Broadband ferromagnetic resonance 56
    4.1.1 Magnetodynamic properties measurements 58
4.2 Propagating spin wave spectroscopy in plain films 61
    4.2.1 Propagation in YIG film 61
    4.2.2 Propagation in metastable thin films 62
4.3 Spin waves in modulated magnetic media 66

Conclusion 70

References 71

List of abbreviations 83

A Vector network analyzer calibration i
A.1 Calibration techniques i
A.2 On-wafer calibration iii

B Measured spin wave spectra iv
B.1 Broadband ferromagnetic resonance in ferromagnetic films iv
B.2 Propagating spin waves in YIG v
B.3 Characteristics of spin waves propagating in Permalloy film vi
B.4 Propagating spin waves in metastable thin film vi

Introduction

Magnetism is a complex and extraordinary quantum-mechanical phenomenon, which despite all efforts still has not been entirely understood. Even though, it remains in the center of the basic and the applied research for decades, as it has already brought significant progress in many branches of applied science. Especially in information technologies, different magnetic phenomena found broad application, from data storage to recent advances in magnetic random access memories.

Nowadays, utilization of electron spin and its wave properties is getting to the forefront of many studies. The emerging field investigating the properties of spin waves towards their potential application in low-power-consumption information technologies is called magnonics [1]. Metamaterials with periodically modulated magnetic properties – magnonic crystals – play a crucial role in magnonics. They provide a possibility of formation of allowed frequency ranges and band gaps in the spin-wave frequency spectra, which are necessary for performing logic operations [2]. The main requirements on the materials from which is a magnonic crystal made of are high saturation magnetization, low attenuation properties and ease of preparation. Hence, there is an ongoing search for novel materials and related patterning possibilities.

Potential candidates for application as magnonic crystals are nickel-stabilized face-centered-cubic iron (FeNi) thin films epitaxially grown on copper [3]. These films are paramagnetic at room temperature and they are capable of undergoing ion-beam-induced phase transition to the ferromagnetic body-centered-cubic structure. Therefore, magnetic patterns can be directly-written into the films by focused ion beam irradiation.

The objective of this thesis is to investigate these metastable FeNi thin films and to explore their potential as a novel material for magnonics.

In Chapter 1, we begin with an introduction to magnonics. We summarize its key aspects, basic principles of spin wave excitation and detection, the most commonly used materials and the prospects of magnonics for its future application in practice. To understand the topics covered by this thesis, we also provide the relevant theoretical background to the micromagnetism, including the magnetization dynamics and the spin wave phenomena. In the last section of the chapter, we present the most basic insight into the all-electrical spin-wave spectroscopy. This method deals with inductive spin-wave excitation and detection via microscale coplanar waveguides or microwave antennas, and with use of a vectorial network analyzer [4], it allows studying spin waves in the frequency domain.

In Chapter 2, we provide a review of the previous investigation of the metastable thin films; from the Fe/Cu(100) system towards the Ni-stabilized Fe thin films grown on a hydrogen-terminated silicon substrate. The section summarizes progress that was made mainly at TU Wien, Austria, our collaborator within a joint project which this thesis is a part of. As one of the joint project goals is transferring the film growth from TU Wien to Central European Institute of Technology Brno, Czech Republic, a substantial part of the chapter is devoted to the preparation of the samples in our laboratory in Brno. We introduce relevant growth and characterization techniques used for the thin film preparation in ultra-high vacuum conditions. Next, we describe the substrate preparation procedure and the following FeNi film growth.

The prepared films provide a unique combination of structural and magnetic properties, valuable for the application in magnonics. Therefore, they are further studied in ambient conditions to fully explore their potential. A focused ion beam is used for the patterning; the atomic force, scanning electron and Kerr microscopies are employed for the investigation. Apart from the magnetic material, we prepare coplanar waveguides acting as spin wave sources and detectors in further studies. They are fabricated by electron beam lithography technique. All the preparation procedures are finalized and by the end of Chapter 3, the samples are prepared for all-electrical spin-wave spectroscopy.

Chapter 4 is fully concentrated on the final experimental part and discussion of the results. First measurements are carried our in order to determine magnetodynamic properties of the investigated material. This is realized through a broadband ferromagnetic resonance technique. Then we perform propagating spin-wave spectroscopy to study the propagating modes in the prepared continuous as well as in micro-patterned films. We compare all the results with commonly used ferromagnetic materials. Finally, we discuss the observed phenomena and possible outlooks.

1 Spin waves in thin magnetic films and periodic media

In this chapter, an introduction to problematics and a brief theoretical background to magnonics are given. Sec. 1.1 reviews state of the art in the field of magnonics. Before properly introducing magnetic spin waves, the basics of the theory of micromagnetism are recalled in Sec. 1.2. Covered topics include the energy formulation of ferromagnetism, a solution of the linearized equation of motion, and a mathematical description of spin waves and their propagation. In Sec. 1.3, different types of periodic magnetic media i.e. magnonic crystals are presented in more detail. And finally, Sec. 1.4 provides a brief introduction to all-electrical spin-wave spectroscopy which is for characterization of magnetic properties within this thesis.

1.1 Introduction to magnonics

Spin wave (SW) is a disturbance of time-independent state in local magnetic ordering propagating across a magnetic medium. As the name suggests, it is connected with a collective oscillation of electronic spin systems in magnetically ordered materials in form of a wave [1, 5]. Described by the classical approach, a SW can be interpreted as a phase-coherent precession of magnetization vector of the magnetic medium, which is characterized by relevant energy density contributions. The wave is further derived from an equation of motion as a small signal disturbance of the quiescent state [6], this approach is used later in this thesis. Equivalently, SWs can be treated using the microscopic approach [7, 8]. In that case, there are introduced SW quanta called *magnons*, which behave as weakly interacting quasiparticles.

The concept of SWs was first introduced by F. Bloch already in 1930 [9] and the waves have been studied ever since by many groups in both theoretical and experimental research works. The first one who directly observed SWs in case of spatially uniform spin precession was J. H. E. Griffiths in 1946 [10], but it was not until 1966 when SWs with a finite wavelength were observed by P. Fleury et al. [11].

It was proven that SWs can be compared with electromagnetic or acoustic waves and can be regarded as their magnetic analogy, as they show many similarities with each other. Different means of SW observation showed they can be excited, guided by a waveguide, reflected [12, 13] or refracted [12] at an interface, polarized [14], self-focused [15] or diffracted [16]. SWs also report quantum tunneling [13] and interference [16]. These waves with wavelengths at the nanometer-scale can carry information in the form of an angular momentum [2]. All the aforementioned effects indicate a possibility of employing the SWs as potential data carriers in computing devices; therefore, SWs present a great interest for the application and the study of their utilization for information processing and storage have become a cornerstone of the emerging field called *magnonics* [1, 5].

1.1.1 Motivation

Microelectronic industry nowadays faces problems resulting from the demand of the market for further and further downscaling of logic devices. The continuous shrinking of the elements causes tremendous difficulties in the effort to reduce the energy consumption and power dissipation of electronic circuits. Besides, the increasing density of devices causes complications with interconnection wiring itself. Whereas maintaining the current trend is still more challenging, there is an urgent practical need for novel devices capable to overcome these constraints inherent to the electron-charge-current-based technology [17]. One of the possible routes for solving the problems is the implementation of magnon logic. This rather progressive way would be a revolutionary solution necessarily comprising redesigning of the entire systems with new more efficient mechanisms, but it could open brand new possibilities benefiting from their wave properties.

Possible SW wavelengths vary in a wide range from nanometers up to coherent oscillations. Especially the short wavelength SWs are a suitable candidate to use as novel information carriers, as they inherently propose utilization of devices even in sub-10 nm scale [2]. Moreover, simultaneous use of SWs with different frequencies and their superposition allows parallel operations. Guided by magnetic waveguides across macroscopic distances, the waves can transfer spin information without charge transfer that normally leads to the generation of Joule heating induced energy loss. The SW signal can be modulated by application of an external magnetic field and it can as well be easily introduced into the material and then converted again to voltage via inductive coupling.

There are also certain drawbacks of magnon logic already known. It is a relatively high attenuation and rather a small group velocity of magnons in the first place. On the other hand, both of these are being less significant with the shrinkage of the devices. Yet, not only SW propagation and manipulation has been studied widely in recent years, but the best suitable materials allowing fast and low damping SW propagation are being searched for as well.

1.1.2 Spin-wave excitation and detection

The excitation and the detection of SWs still remains a significant technological challenge of magnonics, as both high frequencies and precise localization of SWs are essential. SWs can be generated by several means including thermal, magneto-optical and inductive excitation and also excitation via spin-transfer torque [18]. The most common and straightforward technique is the inductive excitation by utilization of microwave antennas [19–23]. This is a powerful technique for generation of rather long wavelengths SWs, and it is anticipated to be applicable up to 100 GHz frequencies [24]; however, more complex solutions are needed in order to excite SWs in the terahertz range. It also becomes increasingly difficult to couple microwaves to metallic waveguides, as the largest possible wavevector transferred by a waveguide scales with the inverse width of its signal line [1]. Therefore, different solutions beneficially using magnetic exchange interactions and spin-transfer torque have been proposed. For example an emission of short-wavelength SWs from vortex core upon its reversal [25–27] or emission from periodic modulation of magnetic anisotropy in thin film [28], coherent SW emission from pinned magnetic domain walls [29] or magnetic multilayers [30–32], and generation of SW by spin-torque nano-oscillators [33–36] – tunable nanometer-size microwave oscillators designed to excite highly localized magnetization precession. The last are currently in the center of interest as they enable efficient directional SW transmission and offer possibility to be utilized as nanoscale emitters. Finally, an alternative compromise approach is based on wavelength conversions in the vicinity of microwave antennas such as using tapered waveguides [37], diffraction grating couplers [38], or increased effective field near edges of patterned antidot structures [39].

Similarly, there exists a wide range of methods enabling diverse possibilities for SWs detection. They vary from each other in sensitivity, spatial and temporal resolution and in the range of detectable SW wavelengths. An overview summarizing selected attributes of different approaches can be found in Ref. [2]. Most of the methods can be classified into following types: inductive [19, 20], spintronic [40–42] and optical detection. The optical detection includes Brillouin light scattering [23, 33, 34, 37, 43–45] the most used method for SW observation nowadays and time-resolved scanning Kerr microscopy [22, 46, 47]. Furthermore, many other kinds of detection have been proposed such as x-ray-detected ferromagnetic resonance [48], time-resolved scanning transmission x-ray microscopy imaging [27] or thermoelectric detection via anomalous Nernst effect [21].

1.1.3 Materials for magnonic application

For successful implementation of magnonic device technologies, the choice of magnetic material plays a crucial role. The attributes essential for the selection are: low attenuation properties to allow spin-wave propagation at long distances, high saturation magnetization, which is needed in order to reach high SW frequencies and group velocities, and sufficiently high Curie temperature to ensure thermal stability of magnons. Above all, the material has to be easily prepared and modified as the waveguides fabrication must be simple and less expensive for its future employment.

The most promising candidate both for study and development of magnonic logic elements has been considered a ferrimagnetic insulator $Y_3Fe_5O_{12}$ (YIG) due to its extremely large propagation lengths and spin-wave lifetime [49–51]. However, this material is connected with major complications in its growth, not compatible with current devices on semiconductors. Another extensively used material is polycrystalline $Ni_{80}Fe_{20}$ alloy called Permalloy. It offers relatively low SW attenuation sufficient for many experiments, together with good availability and easy deposition and patterning [37, 52, 53]. Similar advantages are offered by CoFeB [20] which is commonly used in magnetic tunnel junctions. Recently, also half-metallic Heusler compounds drew an attention [54]. These alloys comprise two transition or rare-earth metals and a main group element, they provide very large SW group velocities, and even SW propagation over 100 μm was detected in Co_2MnSi [55].

However, there is still need for novel materials with significantly reduced attenuation properties, which would be compatible with advanced nanofabrication techniques. Depending on the particular choice of magnetic material, different techniques are used for waveguides and logic elements fabrication: from photolithography often used for YIG processing, through focused ion beam milling, to electron beam lithography widely used to modify, for instance, Permalloy films. These micro- and nanopatterning methods are usually followed by etching or lift-off processes.

Before the functional element fabrication process itself, the magnetic media can be nanopatterned, giving rise to artificial materials of novel properties and opening brand new possibilities for utilization. In patterned magnetic materials, properties of SWs can differ with respect to those of SWs in homogeneous magnetic media. Especially, periodically modulated materials are of particular interest as the SW band structure of such patterned media is modified; allowed states and forbidden frequency gaps, where no magnonic states are allowed, are induced in the spectrum. Many experimental studies have been made on the topic recently, as the introduction of a band gap in SW spectra is essential to enable utilizing of magnons in logic devices.

1.1.4 Magnonic devices

Magnonic devices offer the possibility to be easily manipulated by the applied magnetic field and whereas they are magnetic particles, they can with benefit be used as non-volatile memory elements. Therefore, they can give rise to devices re-programmable at the sub-nanosecond timescale [1]. They can be integrated within present microwave electronics, but with the benefit of shorter wavelength compared with electromagnetic waves at the same frequency range, hence offering better possibilities for subsequent downscaling [1].

The field of magnonics has made significant progress in recent years including a demonstration of first magnonic logic devices. The first experimentally demonstrated prototype of a spin-wave based logic device was a spin-wave NOT gate [56] followed by NOR and NAND gates [57] both based on Mach–Zehnder-type spin-wave interferometer. These devices are operational at room temperature in the GHz frequency range and use the SW amplitude as a logic output [17]. Similarly, the SW phase can be used as the logic output such as in a proposed three-terminal device proposing a solution for NOT and Majority gates [58]. Similar and more advanced designs have been proposed and demonstrated using different materials. For example, a valve transistor combining YIG and cobalt magnetic layers [59], which is able to compare SWs being transmitted between both layers either in parallel or in antiparallel alignment. Similarly, a magnon valve made of two separated YIG layers with magnon conductance controlled by their relative magnetization orientation and an adjacent platinum layer converting magnons to readable voltage [60], or a YIG-platinum transistor allowing magnons spin conductance control by spin-current [61] and other.

Fabrication of these magnon valves that remain in open, or closed state without continually applied an external magnetic field is an important step forward to fully magnon-based circuitry. Notwithstanding the recent great progress, there are still many technological challenges related for example to miniaturization of the devices which are rather macroscopic so far. There is plenty or unexplored paths and opportunities to be seized, giving magnonics a significant potential towards application in the near future.

1.2 Theoretical background

In this section, we will recall the fundamentals of magnetism and the basic formulation of micromagnetism as a continuum theory. Micromagnetism forms an interconnection between quantum mechanic approach and Maxwell's theory of electromagnetic fields. It operates with small continuum entities at the nanoscale – elements of the size of at least a few interatomic distances. Therefore, it is used to describe the magnetic behavior of nanostructures, including phenomena such as magnetic domains and domain walls [62], or to determine hysteresis behavior. Micromagnetism assumes that magnetization – the fundamental quantity of magnetism defining the density of magnetic moment – is a smoothly varying function in space and time. Moreover, it supposes constant magnitude of the magnetization vector over the whole homogeneous magnetic material, allowing it to change only the orientation.

Following text describes the behavior of magnetization in magnetic materials in accordance with the micromagnetic theory[1].

1.2.1 Energy formulation of ferromagnetism

Magnetic materials are classified by magnetic susceptibility $\hat{\chi}$, a tensor quantity relating their magnetization $\mathbf{M}$ with magnetic field strength $\mathbf{H}$

$$\mathbf{M} = \hat{\chi}\mathbf{H}. \tag{1.1}$$

In general, the susceptibility tensor enables the transition between $\mathbf{M}$ and $\mathbf{H}$, which both can be time and position variable and do not need to be collinear to each other. In the special case of a linearity of the two vectors, $\hat{\chi}$ reduces to a scalar. According to its magnitude and sign, magnetic materials can be classified as diamagnetic ($\chi < 0$), paramagnetic ($\chi > 0$), ferri- or ferromagnetic ($\chi \gg 0$) and antiferromagnetic ($\chi \approx 0$)

---

[1] Deeper insight into the problematics provide Ref. [62–64].

materials. Within the scope of this thesis, we restrict ourselves to ferromagnetic materials, namely iron (Fe), nickel (Ni), cobalt (Co) and their alloys Permalloy and $Fe_{78}Ni_{22}$ (FeNi).

The magnetic field **B** is defined by

$$\mathbf{B} = \mu_0(\mathbf{M} + \mathbf{H}) = \mu_0(\chi + 1)\mathbf{H}, \tag{1.2}$$

where μ_0 is magnetic permeability of vacuum, being $4\pi \times 10^{-7}\,\frac{\mathrm{V\cdot s}}{\mathrm{A\cdot m}}$. The expression in parentheses is the permeability of the material.

The origin of spontaneous magnetization and hysteresis of ferromagnets lies in the variations in free energy contributions in the material. These are the temperature dependent Helmholtz and Gibbs free energies. An increase of temperature consequently causes a decrease of magnetic moment and magnetization. In micromagnetism, however, we mainly work with processes at zero thermodynamic temperature. Therefore, the temperature dependence is not considered while building the theory of micromagnetism. The free energy consists of several contributions. The most important of them will be explained in brief.

The first contribution is the Heisenberg exchange interaction, which arises from Coulomb interaction between atoms with unpaired electrons, as a consequence of Pauli exclusion principle prohibiting two electrons to be in the same quantum state [65]. The exchange energy of a pair of spins **S** is given by Hamiltonian $\hat{\mathcal{H}}_{\mathrm{ex}} = -2J_{ij}\mathbf{S}_i \cdot \mathbf{S}_j$. The exchange integral J_{ij} quantifies the strength of the exchange interaction and it is positive (negative) in the case of parallel (antiparallel) spin alignment. In accordance with the $\hat{\mathcal{H}}_{ex}$, the density of **exchange energy** of a magnetic body can be written in a form of

$$\mathcal{E}_{\mathrm{ex}} = -J\sum_{i,j}\mathbf{S}_i \cdot \mathbf{S}_j. \tag{1.3}$$

Moreover, an anisotropic exchange term may arise from the lack of inversion symmetry in specific cases e.g. at the heavy-metal/ferromagnet interface or within certain materials of the non-centrosymmetric crystal lattice. This so-called Dzyaloshinskii-Moriya interaction favors a non-collinear spin configuration unlike the Heisenberg exchange (1.3) and it can be expressed using the strength of the interaction **D** as

$$\mathcal{E}_{\mathrm{DMI}} = -\mathbf{D}\sum_{i,j}\mathbf{S}_i \times \mathbf{S}_j. \tag{1.4}$$

The second contribution is given by **magnetic anisotropy**, the energetic inequality between different orientations of spontaneous magnetization. More mechanisms of an anisotropy exist. It can be caused by the crystallography or the shape of the magnetic body, or induced by an external influence. The first case is referred to as a magnetocrystalline anisotropy and its microscopic origin lies in the spin-orbit coupling and the dipole-dipole interaction. The coupling of electron orbitals with the crystal lattice causes that magnetization can be stabilized in some directions (planes) on the expense of the others. The first are called easy exes (planes), the latter hard axes (planes). For its directionality, it is customary to express the anisotropy energy in a sine series using anisotropy constants K_i. In materials with one easy (hard) axis such as hexagonal or orthorombic crystals, or in thin films, we talk about *uniaxial* anisotropy and write

$$\mathcal{E}_{\mathrm{A,uni}} = K_{\mathrm{u}} \sin^2\theta + K_{\mathrm{u2}} \sin^4\theta + \ldots, \tag{1.5}$$

where θ is the angle between the vector of magnetization and the anisotropy axis. In cubic crystals, we express the *cubic* anisotropy by the direction cosines of the magnetization vector with respect to the anisotropy axes α_i

$$\mathcal{E}_{\mathrm{A,cubic}} = K_1(\alpha_x^2\alpha_y^2 + \alpha_y^2\alpha_z^2 + \alpha_z^2\alpha_x^2) + K_2\alpha_x^2\alpha_y^2\alpha_z^2 + \ldots. \tag{1.6}$$

In the case of thin magnetic films, additional anisotropy term which is associated with the symmetry breaking at interface may arise. Since its magnitude scales inversely with thickness t and it has the easy axis oriented perpendicular to the film plane, it is often written as

$$\mathcal{E}_{\mathrm{A},\perp} = \frac{K_\perp}{t}\alpha_z^2. \tag{1.7}$$

Spins inside a magnetized material interact with each other by a long range dipole-dipole interaction. This third contribution and also the source of shape (magnetic) anisotropy is called **demagnetization energy**. Its density can be written as

$$\mathcal{E}_{\mathrm{d}} = -\frac{\mu_0}{2V}\int_V \mathbf{M}(\mathbf{r}) \cdot \mathbf{H}_{\mathrm{d}} \mathrm{d}V, \tag{1.8}$$

where $\mathbf{H}_{\mathrm{d}}$ is demagnetization field which is caused by magnetization inside the material. The $\mathbf{H}_{\mathrm{d}}$ depends on distribution of spins within the magnetized body and it may generally be complicated to calculate. The proportion between magnetization and the induced $\mathbf{H}_{\mathrm{d}}$ is demagnetization tensor $\hat{N}$ depending on the shape of the magnetized body

$$\mathbf{H}_{\mathrm{d}} = \hat{N}\mathbf{M}, \tag{1.9}$$

The demagnetization tensor trace $\mathrm{tr}(\hat{N}) = N_{xx} + N_{yy} + N_{zz} = 1$ [65]. In a special case of a sphere, $N_{xx} = N_{yy} = N_{zz} = \frac{1}{3}$. For a thin magnetic film in the xy plane, $N_{xx} = N_{yy} = 0$ and $N_{zz} = 1$.

The fourth energy contribution, induced by placing a magnetic body into an external magnetic field $\mathbf{H}_{\mathrm{ext}}$, is called **Zeeman energy**. Its density is written as

$$\mathcal{E}_{\mathrm{Z}} = -\frac{\mu_0}{V}\int_V \mathbf{M}(\mathbf{r}) \cdot \mathbf{H}_{\mathrm{ext}} \mathrm{d}V \tag{1.10}$$

and it is minimized by orientation of spins in direction parallel with the $\mathbf{H}_{\mathrm{ext}}$.

All these energy contributions compete in order to minimize the total energy of the system $\mathcal{E}_{\mathrm{total}}$. This can result in the formation of magnetic domains and particular spin configurations inside the system [62, 64]. Finding the energy minimum gives an effective field $\mathbf{H}_{\mathrm{eff}}$, defined as

$$\mathbf{H}_{\mathrm{eff}} = -\frac{1}{\mu_0}\frac{\delta\mathcal{E}_{\mathrm{total}}}{\delta\mathbf{M}}, \tag{1.11}$$

which can be used to describe this overall effect experienced by the spin.

1.2.2 Magnetization dynamics

To obtain a response of a magnetic system to the application of an external magnetic field, the equation of motion needs to be solved. In the following, we assume a continuous variation of spin alignment and its representation via the magnetization vector – the macrospin model. When a strong static field is applied, all spins are aligned parallel with the field according to the Zeeman energy (1.10) minimization and the magnetization vector precesses around the direction. The equation of motion, proposed by L. Landau and E. Lifshitz reads [66]

$$\frac{\partial\mathbf{M}}{\partial t} = -\gamma\mu_0\mathbf{M}\times\mathbf{H}_{\mathrm{eff}}, \tag{1.12}$$

where γ is the gyromagnetic ratio. For a free electron, $\gamma = g|e|/(2m_{\mathrm{e}})$ with g being a dimensionless g-factor, e the electron charge and m_{e} its mass. However, γ differs for different materials, see Tab. 1.1. The equation of motion describes the change of the magnetization upon an action of a torque $\mathbf{T}$ caused by the field $\mathbf{H}_{\mathrm{eff}}$

$$\mathbf{T} = \mathbf{M}\times\mathbf{H}_{\mathrm{eff}}, \tag{1.13}$$

leading to the precession of the magnetization around the effective field. The Eq. (1.12) describes an ideal case of an undamped precessional motion. However, damping is observed in experiments. Hence, a phenomenological damping term can be included and the equation of motion becomes

$$\frac{\partial\mathbf{M}}{\partial t} = -\gamma_{\mathrm{LL}}\mu_0\mathbf{M}\times\mathbf{H}_{\mathrm{eff}} - \frac{\lambda}{M_{\mathrm{S}}^2}\mathbf{M}\times(\mathbf{M}\times\mathbf{H}_{\mathrm{eff}}). \tag{1.14}$$

Yet, it is only observed suitable for small values of a damping parameter λ in units of s^{-1}. Alternatively, a different damping term depending on the magnetization time derivative can be used. The so-called Landau-Lifshitz-Gilbert equation of motion then reads as

$$\frac{\partial\mathbf{M}}{\partial t} = -\gamma_{\mathrm{G}}\mu_0\mathbf{M}\times\mathbf{H}_{\mathrm{eff}} - \frac{\alpha_{\mathrm{G}}}{M_{\mathrm{S}}}\left(\mathbf{M}\times\frac{\partial\mathbf{M}}{\partial t}\right), \tag{1.15}$$

where α_{G} is a dimensionless phenomenological Gilbert damping parameter. The relation between the gyromagnetic ratios and the damping parameters can be expressed as

Tab. 1.1: Gyromagnetic ratios for selected magnetic materials [64, 68].

material	$\gamma/2\pi$ (GHz/T)	material	$\gamma/2\pi$ (GHz/T)	material	$\gamma/2\pi$ (GHz/T)
Fe	29.1	Gd	27.3	YIG	28.1
Co	30.4	Ni	30.5	Permalloy	29.3

$\gamma_{\mathrm{LL}} = \gamma_{\mathrm{G}}/(1+\alpha_{\mathrm{G}}^2)$ and $\lambda = \alpha_{\mathrm{G}}\gamma\mu_0 M_{\mathrm{S}}$. Thus for small values of α_{G}, both damped equations of motion (1.14) and (1.15) are the same [67]. Within the framework of this thesis, we do not distinguish between gyromagnetic ratio and damping parameter in both models and write γ and α, respectively.

It is not possible to find an analytical solution for the equation of motion in its general form. Therefore, in order to solve it, its linearization has to be done first. To do so, we use following assumptions.

We assume thin magnetic film infinitely extended in the xy-plane, hence leaving only one non-zero component of the demagnetization tensor $N_z = 1$. To properly describe the crystalline character of the studied material, we consider possible four-fold magnetic anisotropy with two perpendicular easy axes in the film plane and a surface perpendicular magnetic anisotropy. However, we restrict the anisotropy contribution to values lower than those induced by the demagnetization field [69]. Such magnetic film is placed in a homogeneous external magnetic field pointing in the x direction $H_{\mathrm{ext}}\hat{\mathbf{e}}_x$, strong enough to ensure saturation of the film in this direction, and small homogeneous ($k = 0$) excitations along the y axis: $\mathbf{h}_{\mathrm{ext}}(t) = h_{\mathrm{ext}} \exp(i\omega t)\hat{\mathbf{e}}_y$ with angular frequency ω. Considering Eq. (1.1), the Eq. (1.15) can be solved following the calculation in Ref. [70].

The solution is provided in the form of χ_{yy} component of the susceptibility tensor

$$\chi_{yy} = \frac{\omega_{\mathrm{M}}(\omega_{\mathrm{H}} + \omega_{\mathrm{eff}} - i\alpha\omega)}{\omega_{\mathrm{res}}^2 - \omega^2 - i\alpha\omega(2\omega_{\mathrm{H}} + \omega_{\mathrm{eff}})}. \tag{1.16}$$

Here, we use

$$\omega_{\mathrm{M}} = \gamma\mu_0 M_{\mathrm{S}};\, \omega_{\mathrm{H}} = \gamma\mu_0 H;\, \omega_{\mathrm{eff}} = \gamma\mu_0 M_{\mathrm{eff}}, \tag{1.17}$$

where

$$H = \gamma\mu_0\left(H_{\mathrm{ext}} + \frac{2K_1}{\mu_0 M_{\mathrm{S}}}\right);\, M_{\mathrm{eff}} = M_{\mathrm{S}} - \frac{2K_\perp}{\mu_0 M_{\mathrm{S}} t} \tag{1.18}$$

and the resonance frequency given by

$$\omega_{\mathrm{res}}^2 = \omega_{\mathrm{H}}(\omega_{\mathrm{H}} + \omega_{\mathrm{eff}}). \tag{1.19}$$

The equation (1.19) is a special case of so-called Kittel formula [71], a field dependent resonance of thin magnetic film placed in a homogeneous magnetic field

$$\omega_{\mathrm{res}}^2 = (\omega_{\mathrm{H}} + (N_y - N_x)\omega_{\mathrm{M}})(\omega_{\mathrm{H}} + (N_z - N_x)\omega_{\mathrm{M}}) \tag{1.20}$$

for $\omega_{\mathrm{M}} \to \omega_{\mathrm{eff}}$ and $N_x = N_y = 0$ and $N_z = 1$.

The χ_{yy} in Eq. (1.16) can be split apart into real and imaginary parts

$$\mathbb{R}(\chi_{yy}) = \frac{\omega_\mathrm{M}(\omega_\mathrm{H}+\omega_\mathrm{eff})(\omega_\mathrm{res}^2-\omega^2)}{(\omega_\mathrm{res}^2-\omega^2)^2+\alpha^2\omega^2(2\omega_\mathrm{H}-\omega_\mathrm{eff})^2}, \tag{1.21}$$

$$\mathbb{I}(\chi_{yy}) = \frac{\alpha\omega\omega_\mathrm{M}\left[\omega^2+(\omega_\mathrm{H}+\omega_\mathrm{eff})^2\right]}{(\omega_\mathrm{res}^2-\omega^2)^2+\alpha^2\omega^2(2\omega_\mathrm{H}^2-\omega_\mathrm{eff}^2)^2}. \tag{1.22}$$

The imaginary part can be approximated by a Lorentzian function and its maximum is found for $\omega = \omega_\mathrm{res}$ giving the equation for the so-called ferromagnetic resonance (FMR) frequency

$$f_\mathrm{res} = \frac{\omega_\mathrm{res}}{2\pi} = \frac{\gamma\mu_0}{2\pi}\sqrt{H(H+M_\mathrm{eff})}. \tag{1.23}$$

The linewidth $\Delta\omega$ of the Lorentzian peak is connected with the damping parameter α. Considering $\Delta\omega \ll \omega_\mathrm{res}$, a full width at half maximum (FWHM) of ω gives [72]

$$\Delta\omega = \alpha(2\omega_\mathrm{H}+\omega_\mathrm{eff}). \tag{1.24}$$

The linewidth $\Delta\omega$ is also observed to be connected with the linewidth ΔH, which can be interpreted in terms combining the inhomogeneous broadening ΔH_0 and Landau-Lifshitz (1.14) or Gilbert (1.15) damping model [73]. Then

$$\Delta H = \Delta H_0 + \frac{4\pi\alpha f_\mathrm{res}}{\gamma}. \tag{1.25}$$

where α is the Landau-Lifshitz or Gilbert damping parameter in the dimensionless form. From this expression, the damping parameter independent of the inhomogeneous broadening in a field can be obtained. The α can also be determined from Δf dependency after conversion of the expression (1.25) into a frequency domain [74]. For $k=0$:

$$\Delta f = \left(\frac{\gamma\mu_0}{2\pi}\Delta H_0 + 2\alpha f_\mathrm{res}\right)\sqrt{1+\left(\frac{\gamma\mu_0 M_\mathrm{S}}{4\pi f_\mathrm{res}}\right)^2}. \tag{1.26}$$

1.2.3 Spin waves

In the previous section, we discussed uniform magnetic excitations only, i.e. the case when all magnetic moments precess at the same phase. Such behavior can be described as a SW of infinite wavelength and thus the wavevector $k=0$. In the following section, a case of non-zero k SWs is addressed.

The frequency spectrum of SWs can be divided according to the wavevector into two parts: the SWs with a long wavelength and small k values dominated by the dipolar interaction usually called *magnetostatic waves*, and the SWs with a short wavelength and large k values known as *exchange dominated spin waves*. The former are discussed in more detail in this section. Finally, a spatial confinement can lead to the emergence modes called *standing spin waves.*

In order to analyze the magnetostatic modes in different geometries, magnetoquasistatic approximation which is presented in more detail in Ref. [75] can be used.

We start with the magnetoquasistatic approximation to Maxwell's equations in the absence of currents:

$$\boldsymbol{\nabla} \cdot \mathbf{B} = 0 \tag{1.27a}$$

$$\boldsymbol{\nabla} \times \mathbf{H} = 0 \tag{1.27b}$$

$$\boldsymbol{\nabla} \times \mathbf{E} = i\omega\mathbf{B} \tag{1.27c}$$

and suppose the absence of anisotropy and exchange interaction. Since $\boldsymbol{\nabla} \times (\boldsymbol{\nabla}\Psi) = 0$ for any analytical function Ψ, it can be written $\mathbf{H} = -\boldsymbol{\nabla}\psi$ from Eq. (1.27b). Using both Eq. (1.2) and (1.27a) and considering a wave propagating in an angle θ with respect to the bias field $H_{\text{ext}}\hat{\mathbf{e}}_z$, a wave equation of the spatial part of the scalar potential ψ can be written as

$$(1+\chi)\left(\frac{\partial^2\psi}{\partial x^2} + \frac{\partial^2\psi}{\partial y^2}\right) + \frac{\partial^2\psi}{\partial z^2} = 0. \tag{1.28}$$

This, so-called *Walker* equation, is the basic equation for magnetostatic modes in homogeneous media and its solution is referred to as the magnetostatic modes.

First, assuming plane wave propagation $\psi = \exp(i\mathbf{k}\cdot\mathbf{r})$ in infinite magnetic medium, the Eq. (1.28) simplifies to

$$(1+\chi)(k_x^2 + k_y^2) + k_z^2 = 0. \tag{1.29}$$

Solving the equation for a wave propagating along $\hat{\mathbf{e}}_z$, dispersion relation of plane wave magnetostatic modes can be explicitly expressed in terms of frequency [75]:

$$\omega = \sqrt{\omega_{\text{H}}(\omega_{\text{H}} + \omega_{\text{M}}\sin^2\theta)}. \tag{1.30}$$

It is worth to notice that the result is independent of k. This degeneracy can be removed either by introducing boundaries, such as in thin films, or considering the exchange interaction. The latter can be done by addition of the exchange term $\omega_{\text{M}}\lambda_{\text{ex}}k^2$ to ω_{H} of the magnetostatic plane wave in Eq. (1.30).

The same results as those we obtained from the macrospin model here and in Sec. 1.2.2 can be derived by the microscopic approach which is thoroughly explained in Ref. [75, 76].

The dispersion relations of distinct magnetostatic modes in finite media can be derived by solving the Walker equation (1.28) with a different choice of boundary conditions. We start by defining the group velocity v_{g} and the phase velocity v_{p} of a SW as

$$v_{\text{g}} = \frac{\partial\omega}{\partial k} \quad \text{and} \quad v_{\text{p}} = \frac{\omega}{k}. \tag{1.31}$$

According to the sign of v_g and v_p, the modes showing the same (opposite) directions are called *forward* (*backward*) modes. In order to solve the Walker equation for a thin film, it is distinguished between the case of the film magnetized in-plane and out-of-plane. The magnetostatic modes are then classified by the relative orientation of the magnetization $\mathbf{M}$ with respect to the film surface and to the wavevector $\mathbf{k}$.

Magnetostatic surface waves

Magnetostatic surface spin wave (MSSW), known also as Damon-Esbach (DE) mode [77] are observed in the in-plane magnetized film with a perpendicular alignment of the $\mathbf{k}$ with respect to the $\mathbf{M}$. When the film is magnetized along the x-axis, the SW propagates along the y-axis, hence $\mathbf{k} \perp \mathbf{M}$. The dispersion relation obtained by solving Eq. (1.28) is given by

$$\omega^2_\mathrm{MSSW} = \omega_\mathrm{H}(\omega_\mathrm{H} + \omega_\mathrm{eff}) + \frac{\omega^2_\mathrm{eff}}{4}(1 - \mathrm{e}^{-2k_\parallel t}). \tag{1.32}$$

Here the $k_\parallel$ is an in-plane component of the wavevector $\mathbf{k}$ and t is the film thickness. The name of the mode comes from the fact that its amplitude decays exponentially from the film surface. The dispersion relation and the group velocity are plotted in Fig. 1.1.

Magnetostatic backward volume waves

Magnetostatic backward volume waves (MSBVW) are the mode with the wavevector parallel with the magnetization direction $\mathbf{k} \parallel \mathbf{M}$ and both lying in the film plane. The dispersion relation for the lowest order can be given explicitly by

$$\omega^2_\mathrm{MSBVW} = \omega_\mathrm{H}\left[\omega_\mathrm{H} + \omega_\mathrm{eff}\left(\frac{1 - \mathrm{e}^{-k_\parallel t}}{k_\parallel t}\right)\right]. \tag{1.33}$$

On the contrary with the MSSW, the amplitude of the waves does not decay within the volume of the film and the group velocity is negative, whereas the phase velocity stays positive. Hence, this mode is a backward wave.

Magnetostatic forward volume waves

Magnetostatic forward volume waves (MSFVW) concern a normally magnetized thin film and a spin wave propagating in the film plane. Therefore, the wavevector $\mathbf{k} \perp \mathbf{M}$ and the wave propagation is independent of the $k_\parallel$ orientation in the plane. The lowest order dispersion relation can be written as

$$\omega^2_\mathrm{MSFVW} = \omega_\mathrm{H}\left[\omega_\mathrm{H} + \omega_\mathrm{eff}\left(1 - \frac{1 - \mathrm{e}^{-k_\parallel t}}{k_\parallel t}\right)\right]. \tag{1.34}$$

Both the group and the phase velocities are positive, which implies a forward mode and the amplitude is again uniformly distributed throughout the volume of the film.

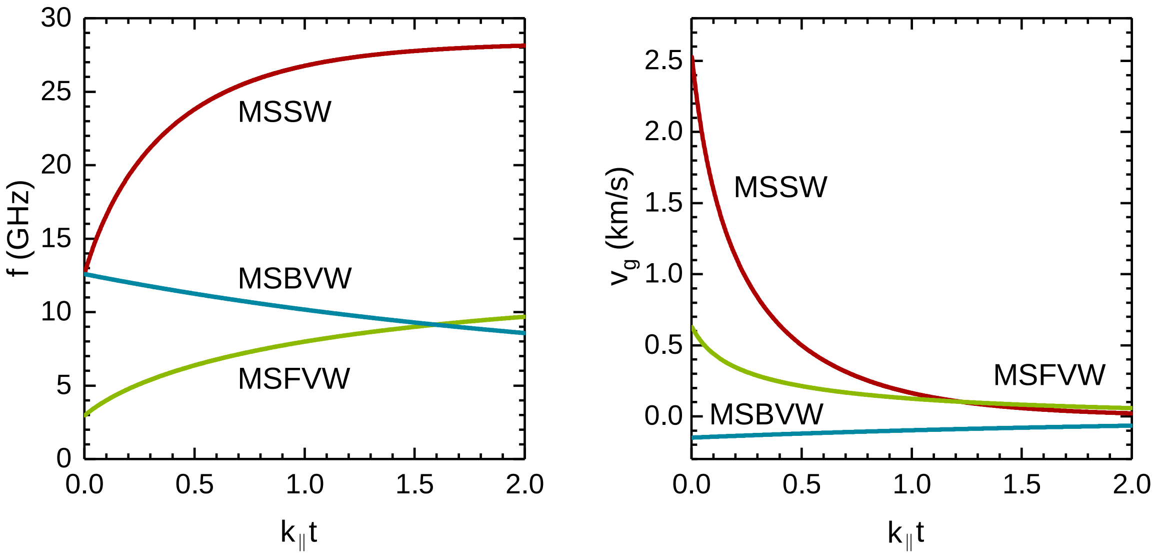

Fig. 1.1: Spin-wave dispersions calculated using Eq. (1.32), (1.33) and (1.34) and group velocities calculated by differentiating the equations according to the Eq. (1.31). Material parameters are set to correspond with studied FeNi thin films: $\mu_0 M_\mathrm{S} = 1.76\,\mathrm{T}$, $\gamma/(2\pi) = 29.5\,\mathrm{GHz/T}$ and $t = 8\,\mathrm{nm}$ at $\mu_0 H = 0.1\,\mathrm{T}$.

The lowest order dispersion relations and corresponding group velocities obtained by its differentiation are plotted for all the three modes in Fig. 1.1.

The so far mentioned modes describe *propagating* spin waves. It is apparent as they always have a non-zero group velocity, the energy is being transferred. The other existing possibility are the standing SWs that transfer neither energy nor information while having $|v_\mathrm{g}| = 0$. As in an electromagnetic wave analogy, a standing SW is the result of interference between two waves propagating in the opposite directions. Moreover, the possibility of formation of the standing waves arises from a spatial confinement. This can be induces in magnetic nanostructures or periodic magnetic media serving as potential wells [74] for the SW. However, even an in-plane magnetized thin film can host a perpendicular standing spin wave (PSSW) [72, 78] with the perpendicular wavevector component $k_\perp$ limited by the boundary conditions, such as that only integer multiplies p of the half of the corresponding wavelength can fit into the film thickness. The dispersion of the PSSW is given by

$$\omega_\mathrm{PSSW}^2 = \left[\omega_\mathrm{H} + \omega_\mathrm{eff} + \frac{2A\gamma}{M_\mathrm{S}}\left(\frac{p\pi}{t}\right)^2\gamma\right]\left[\omega_\mathrm{H} + \frac{2A\gamma}{M_\mathrm{S}}\left(\frac{p\pi}{t}\right)^2\gamma\right], \tag{1.35}$$

where A is the exchange stiffness and t is the thickness of the film.

1.3 Magnonic crystals

Magnonic crystals (MC) are artificial crystals created by periodical variation of different materials or modulation of material parameters, which modify the SW propagation within. Detailed overviews of state of the art MCs were recently presented by Krawczyk et al.

[79] and Chumak et al. [2]. Here, we will summarize different kinds of MCs and available approaches to their preparation.

Concept of magnonic crystals

As presented in the Sec. 1.1, MCs are needed to process information in form of magnons and implementation of magnon logic into the circuitry. The SW band structure can be tailored to induce bandgaps and allowed minibands, which enables the realization of integrated SW logic.

A periodic modulation of magnetically ordered materials, from arrays of etched grooves or pits to the variation of saturation magnetization, magnetic anisotropy, or internal magnetic field is of special interest. The band structure is affected both by periodic patterning and by the spatial arrangement of the magnetization vector. The modulation provides an extra degree of freedom for tailoring of the SW properties.

MCs are classified depending on whether their properties can or cannot be changed in time. Static MCs, properties of which are constant over time, can be integrated into the magnonic circuitry as passive elements e.g. microwave filters, resonators and delay lines for generation of microwaves. Reconfigurable or dynamic MCs – artificial crystals with adaptable band structure – are suitable candidates to use as active devices in SW-based technology allowing e.g. tunable filtering, time reversal or frequency conversion.

There are two mechanisms responsible for band formation in a periodically modulated media. The first is a coherent scattering and Bragg reflection in a periodic media. The second is described by confined(standing) modes in resonators, arranged in such way that they support propagation of SWs of discrete frequencies from one to another. In both cases, the phase and the velocity of propagating SWs are determined by geometrical parameters of the MC.

Based on the geometry, MCs can be divided into thin-film and bulk crystals. In both categories their properties can be modulated in one- [80], two- [81] or three-dimensions [82]. The last type has been so far studied theoretically, but the first two types have already been experimentally demonstrated in numerous investigations using different materials and fabrication concepts.

Static magnonic crystals

The most straightforward approach for the preparation of static MC is patterning of a homogeneous film or a waveguide. By using lithography and etching techniques, it is possible to create arrays of grooves, holes and stripes or different structures resulting in periodic variation of the film thickness [83–85]. The one-dimensional MCs prepared from grooved YIG waveguides, for instance, were studied both theoretically and experimentally [86, 87]. The frequency width of rejection band and its rejection efficiency of MSBVW and MSSW modes has been found to be a function of the grooves dimensions, increasing with both their width and depth. Another similar case is a spatial variation of SW waveguide width, which was initially proposed using Permalloy nano-wires structured in a step-like manner [88]. Later, SW spectra in nano-wires with continuous (periodic) width modulation were studied and distinct resonance modes were observed for various film thicknesses [89].

A different approach employs the saturation magnetization as a tunable parameter in MC preparation. The existence of the SW localized modes with the frequency lying inside band gaps of a one-dimensional MC with alternating saturation magnetizations was predicted by numerical calculations [90]. Crystals combining stripes of two ferromagnetic materials (such as Co and Permalloy) [91] or single-material waveguides with locally reduced saturation magnetization [92] were introduced. It was as well observed, that even a slight variation of the saturation magnetization results in a decrease of the SW transmission about an order of magnitude [93] and that the band gap width can be tailored by changing the width of the stripes.

Combination of both approaches (modulation of the saturation magnetization and the geometry) gives rise to MCs comprising two different nanostructured magnetic materials, which provide even better adjustability of the SW spectra [84].

Moreover, not only the ferromagnetic material itself has to be structured to induce band gaps in the SW spectrum. It was proposed and experimentally confirmed that MCs can be prepared by periodic metalization of a ferromagnetic layer [50].

Reconfigurable and dynamic magnonic crystals

More recent studies have been carried out on the preparation of MCs with properties adjustable in time, which are called reconfigurable. In the case that timescale of the reconfiguration is shorter than the time of the SW propagation through the MC, the crystal is called dynamic.

Different methods of reconfigurable MCs fabrication were introduced. For instance, thermal gradients can be created by laser illumination, resulting in local modulation of the saturation magnetization [94]. These variations in the magnetization distribution lead to the formation of band gaps in the SW transmission spectrum. The band gap positions are given by the crystal geometry, whereas their widths in the frequency spectrum are adjustable by the intensity of the laser illumination.

Besides the thermo-optically induced modulation of saturation magnetization, another means of MCs control was proposed by using electric field or current. It was proposed for instance using heterostructures with perpendicular magnetic anisotropy controllable by applied voltage [95] or utilizing a cavity in antidot crystal with a defect, which can act as a SW resonator upon injection of spin-polarized current in the vicinity of the defect [96]. Another recently proposed and experimentally investigated alternative is based on utilization of surface-acoustic-wave in YIG [97]. Also, a novel approach, which has been theoretically studied, is dynamic crystal based on magnetic domain wall nucleation and annihilation [98].

Dynamic MCs are currently getting into the center of interest as they hold potential for signal-processing and sensors applications. A special interest is currently paid to the electric-field-controlled MCs which enable further operation under low energy consumption when compared to the optically controlled crystals.

Spin waves in periodic systems

Calculation of SW dispersion relations in periodically modulated media can be performed using the plane-wave method. It has been widely used as a technique for solving Maxwell's equations in last decades and became very popular in the application in photonics. It has also become a common tool to calculate the dispersions of SW in two dimensions [99] and later it has been extended to describe also three-dimensional MCs [82].

In general, the technique numerically solves eigenvalue problems in systems with spatial periodicity by their transformation into the reciprocal space via Fourier transformation. It starts from the linearized equation of motion converted into the reciprocal space. Then, exploiting periodic boundary conditions to describe the problem, the technique uses the ansatz of plane waves to find the solution. More detailed description of the plane-wave method can be found in Ref. [74].

1.4 All-electrical spin-wave spectroscopy

In the framework of the thesis, the SW investigation is performed via inductive techniques, namely by the broadband ferromagnetic resonance (FMR) and by the propagating spin-wave spectroscopy (PSWS). To introduce the measurement process, we present an experimental basics to the inductive techniques using a vector network analyzer (VNA) and the most important concepts of high-frequency (hf) engineering[2]. Especially Ref. [4] may be found very instructive to the understanding of the VNA instrument and its operation principle. Plus, the theoretical background of associated techniques is thoroughly explained in Ref. [72].

1.4.1 Vector network analyzer

Nowadays, the VNA has found a wide application potential in hf measurement techniques. It is used to characterize a vast range of hf passive components including cables, couplers, filters, attenuators or antennas, and active devices such as transistors or amplifiers. It is, however, necessary that these devices operate only in their linear mode of operation. Then, their characterization is performed by measurement the network or *scattering* parameters, the so-called S-parameters, as a function of frequency.

In the most basic concept, the VNA is used to measure the impedance. Such examination is very simple at low frequencies, since a common voltmeter, an ammeter, and

---

[2] By the designation hf, we refer to a range of radio frequencies approx. 10^7-10^{11} Hz.

a sine-wave generator can be employed to measure the ratio between voltage and current, to calculate the impedance. However, the measurement of incident and reflected waves to obtain the impedance becomes more complicated at hf. In that case, the VNA is used to measure an impedance response of a device under test (DUT) to a sine-wave stimulus. With the use of a signal separation hardware and a pair of receivers, signals from the waves incident to and reflected from the DUT are measured. The impedance response characterized by the S-parameters is obtained in its complex form, as both phase and amplitude of the signal are acquired. Hence, the designation “vector”. For comparison scalar network analyzers, which were developed earlier, provide the response only as scalar quantities.

An important part of the measurement process is a calibration. This is required in order to eliminate systematic errors of the measurement system and also to exclude the influence of hf cables and probes, which are used to connect the DUT with the VNA. After performing a calibration, the assessed S-parameters depend only on the microwave circuit of the DUT. The errors can be corrected in multiple ways, using various calibration processes, described in more detail in Appendix A.1. The most common technique for the VNA calibration (and also the method used within the framework of this diploma project) is the SOLT (*Short-Open-Load-Through*) calibration. Generally, it relies on the connection of well-defined standards to both ports of the VNA before connecting the DUT and measuring the frequency response.

1.4.2 Microwave excitation and detection

Excitation of SWs in the media of our investigation is ensured by a coplanar waveguide (CPW) [100].

The mechanism of the inductive SW excitation lies in generation of an alternating Oersted magnetic field around the waveguide placed in a proximity to the magnetic material. The whole volume of the magnetic material is initially saturated by a bias magnetic field so that all its spins are aligned parallel. By applying a hf signal to the waveguide, the alternating field in a direction perpendicular to the current is created and its components which are non-collinear with the bias magnetic field induce a torque acting on the magnetization, in accordance with Eq. (1.13). An amplitude of the magnetization precession is increased in the vicinity of the waveguide and is transmitted further through neighboring spins. Meeting the conditions imposed upon the bias field and oscillation frequency enables the SW propagation in the magnetic material.

The detection of SWs is ensured by the same mechanism as the excitation. Using an analogical waveguide as the antenna, the SW is detected by an inductive pickup.

Coplanar waveguide

A coplanar waveguide comprises a conductive strip, which is placed on the surface of a dielectric, and two ground electrodes placed symmetrically along the strip. This configuration benefits from the simplicity of the design, as all electrodes take place on one side of the dielectric substrate. Another benefit of a CPW is its inherent ability to produce a circularly polarized magnetic vector at the surface of the dielectric between the electrodes.

There is a whole range of wavevectors k that are excited by a single waveguide, however, they are not all excited to the same extent. In case of a CPW, the excitation spectrum is given by a Fourier transform of the $h_{\mathrm{ext}}\hat{\mathbf{e}}_y$. The excitation spectrum comprises dozens of peaks and gaps, and its shape is a function of the CPW geometry. There exists a maximum at the excitation spectrum, which is located at $k = k_{\mathrm{CPW}}$ and it identifies the most excited SW wavelength by that particular CPW. Another important value in the excitation spectrum is the first minimum located at $k = k_{\mathrm{cutoff}}$. As the second maximum is significantly attenuated compared to the first one, the k_{cutoff} can be looked at as the highest wavevector that is excited. To obtain the whole excitation spectrum of a CPW, the fast Fourier transform has to be performed. It is however possible to estimate the k_{cutoff} value alone. In the literature can be found different approaches resulting in similar values, using either a formula $k_{\mathrm{cutoff}} \approx \pi/w_{\mathrm{s}}$ [101] or $k_{\mathrm{cutoff}} \approx 2\pi/(w_{\mathrm{s}} + 2g)$ [102], where w_{s} is the width of the signal line and g is the gap between the signal line and each of the ground lines of the CPW.

Microwave transmission

In order to understand the measurement and the S-parameters, we introduce the basic theory of electromagnetic propagation in a microwave transmission line. There are four electric parameters describing a transmission line given by its geometry and material: resistance R and inductance L of the conductors, capacitance C between the conductors and conductance G of the underlying dielectric. All these parameters are related through voltage and current. In hf systems, however, two other parameters are mostly used for the characterization instead of the static parameters voltage and current. The first one is called the characteristic impedance Z_{c} of the line

$$Z_{\mathrm{c}} = \sqrt{\frac{R + i\omega L}{G + i\omega C}} \tag{1.36}$$

and it is the hf counterpart to the impedance which relates static voltage and current. The second one is the propagation constant γ_{c} defined by

$$\gamma_{\mathrm{c}} = \sqrt{(R + i\omega L)(G + i\omega C)}. \tag{1.37}$$

Both the Z_{c} and γ_{c} are generally complex quantities. The γ_{c} is often split in the real and the imaginary parts called the attenuation constant and the phase constant, respectively.

In the case of a low-loss transmission line, $R \ll \omega L$ and $G \ll \omega C$. The Z_{c} can be approximated by the expression

$$Z_{\mathrm{c}} = \sqrt{\frac{L}{C}}, \tag{1.38}$$

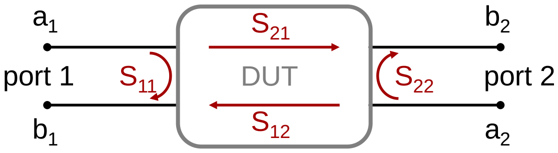

Fig. 1.2: A schematics of the S-parameter model of the two-port DUT. Complex and normalized incident waves a_i and outgoing waves b_i are indicated together with the corresponding S-parameters.

which is a function of the geometry only. Hence in the case of a CPW, the Z_c can be adjusted by the width of the conductors and spacing between them and it is commonly chosen to be $50\,\Omega$.

1.4.3 Scattering parameters

In order to describe a DUT in the hf measurements, the S-parameters are preferably used, instead of more complicated measurements of total voltage and current. To characterize a transmission element, a so-called two-port model can be used[3]. The two terminals of the element are called ports $i=1$ and 2. Then, a pair of waves a_i and b_i is defined

$$a_i = \frac{V_i + Z_{\mathrm{c}i} I_i}{2\sqrt{Z_{\mathrm{c}i}}} \quad \text{and} \quad b_i = \frac{V_i - Z_{\mathrm{c}i} I_i}{2\sqrt{Z_{\mathrm{c}i}}}, \tag{1.39}$$

which both are complex and normalized. Here, V_i, I_i, and Z_{ci}, are the voltage, the current and the characteristic impedance of the transmission line at the port i, respectively. The waves a_i and b_i can be interpreted as an incident wave and an outgoing wave. Using these waves, we can define the S-parameters as follows

$$\begin{pmatrix} b_1 \\ b_2 \end{pmatrix} = \begin{pmatrix} S_{11} & S_{12} \\ S_{21} & S_{22} \end{pmatrix} \cdot \begin{pmatrix} a_1 \\ a_2 \end{pmatrix}. \tag{1.40}$$

The S-parameters defined in this way denote the ratio of the outgoing wave at port i to the incident wave at the other port. And it also means that the wave b_i is a linear combination of the incident waves at both ports. It should be noted that any DUT can be fully characterized only by a set of S-parameters. The mutual relation between both waves and the S-parameters is shown in a schematics of the two-port model in Fig. 1.2.

Reciprocity and symmetry are other decisive properties of the DUT. When the former is fulfilled, the transfer function of the DUT is independent of the wave propagation direction and the S-parameters form a symmetric matrix with $S_{21}=S_{12}$. The latter implies $S_{11}=S_{22}$ for a symmetric DUT.

---

[3] The notation can be as well extended for n-port device using n^2 of the S-parameters. However, we work with two ports exclusively using our VNA.

1.4.4 Broadband ferromagnetic resonance technique

The broadband FMR is a standard technique for measurement of the magnetization dynamics in bulk magnets, thin magnetic films or micro-patterned magnetic media. It offers a possibility to measure the magnetodynamic properties in the frequency domain over a range of tens of GHz. In this way, the measured magnetic parameters can be obtained with high accuracy and their frequency dependence can be accessed.

The FMR technique allows the excitation of SWs with the wavevector close to zero. A CPW with a relatively wide signal line is used to ensure that $k_{\mathrm{CPW}} \approx 0$ and the other $k > 0$ contribute very little to the excitation spectrum.

An output of the technique are FMR parameters which are obtained from a standard measurement of the S-parameters against frequency and magnetic field. Magnetic excitation is a sinusoidal signal, provided to the sample via a CPW. A single CPW serves as a transmitter and a receiver of the SW and the dynamic response of the sample is inductively detected by the VNA. The measured quantity is either the reflected signal S_{11} (or S_{22}), or the transmitted signal S_{21} (or S_{12}). By analyzing the frequency sweep spectra, the frequency linewidth can be obtained and used for characterization of the dynamic magnetic properties.

It is mostly not possible to distinguish the frequency dependent signal from the background signal. Therefore, techniques involving subtraction of the measured signal from a reference signal, or its division by the reference signal are commonly used. The frequency spectra measured either in the zero bias field or in full magnetic saturation are most often used as references.

There are two different experimental arrangements commonly used. In the first case, the magnetic medium is covered by an electric insulation layer such as silicon dioxide (SiO_2) and a waveguide is lithographically prepared on the top, see Fig. 1.3a. Such configuration is with benefit used when magnetic micro- or nanostructures are investigated, as it allows to precisely align the waveguide with the structures. In the second case (Fig. 1.3b), the waveguide and the magnetic media are prepared on two separate sub-

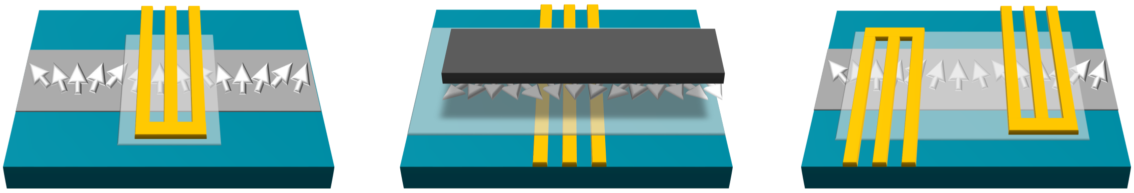
(a) (b) (c)

Fig. 1.3: A schematics of the measurement setup for the ferromagnetic resonance measurement using lithographically patterned CPW (a) or the flip-chip technique (b) and a schematics of setup suitable for the propagating spin-wave spectroscopy (c). According to the waveguide design, these methods allow three different qualities can be measured: A frequency response after the input signal reflection (a) or transmission (b) and a signal connected with propagation of the SWs (c).

strates. The substrate with magnetic film is placed on top of the isolated waveguide so that the film is turned towards the waveguide. The so-called *flip-chip* technique can be used only for the investigation of magnetic properties of continuous thin films or large arrays of structures, as the alignment is more complicated.

1.4.5 Propagating spin-wave spectroscopy

The propagating spin-wave spectroscopy (PSWS) technique is a tool for measurement of magnetostatic modes with non-zero wavevectors k. Similarly to the broadband FMR, the PSWS relies on the inductive excitation and detection of SWs via CPWs (or microwave antennas). In this case, the excitation and the detection are ensured by two waveguides spatially separated by short distance across which the excited SW can propagate (Fig. 1.3c). The reflected signal S_{ii} and also the transmitted signal S_{ij} from one waveguide to the other can be measured by the VNA. Then, the characteristics of the propagating SW such as attenuation length, phase delay, group velocity or magnetization relaxation rate can be calculated from the transmitted signal. In the PSWS configuration as well, both the lithographic preparation and the flip-chip techniques can be used.

To excite the SW modes with large k values in common ferromagnetic materials based on 3d transition metals, the dimensions of the waveguides need to lie in the order of tens of nanometers to units of micrometers. The waveguides of precise widths and spacings are necessary to provide the excitation spectrum with defined distributions of wavevectors. Therefore, they are commonly prepared by the electron beam lithography (EBL) technique.

There is, however, an exception in terms of the dimensions when the SW propagation media consists of a material with very low-attenuation properties, such as YIG. In this case, nearly macroscopic waveguides can be used. Conversely, very narrow waveguides cannot be used with YIG, as its low saturation magnetization limits the excitation frequencies to rather low values (and therefore limits also its potential for hf application).

It is worth mentioning that due to its low attenuation properties, YIG has become the first material extensively studied for SW propagation and it is still probably one of the most used materials in the PSWS. The attenuation lengths, i.e. the length scale at which the wave amplitude decreases by a factor of e, observed in YIG films lie in the micrometer to millimeter scale. Different propagating modes have been investigated in continuous and patterned films [51, 103, 104] and YIG is also employed as a reference material within the framework of this project.

2 Metastable FeNi thin film preparation in ultra-high vacuum

The purpose of this chapter is to introduce the first experimental part: preparation of samples. Techniques used in the preparation process are briefly introduced in Sec. 2.1. Then, it is summarized the state of knowledge of metastable FeNi thin films made at Institute of Applied Physics at TU Wien (TUW) and lately also at our laboratory in Brno. A model system of Fe/Cu(100) is described in Sec. 2.2 and its later replacement by FeNi/Cu(100)/H-Si(100) is discussed. Sec. 2.3 provides a concise description of the technological procedure of metastable FeNi film and the substrate preparation performed in our laboratory.

For the sake of clarity, the whole preparation process, in a nutshell, is illustrated in Fig. 2.1. A more detailed description is provided in the following text.

2.1 Introduction to ultra-high vacuum techniques

Ultra-high vacuum (UHV) stands for vacuum regime with the pressure of residual gas below 10^{-7} Pa or 10^{-9} mbar. In order to achieve high quality thin film samples with well defined interfaces and material composition, it is a must to perform the whole preparation

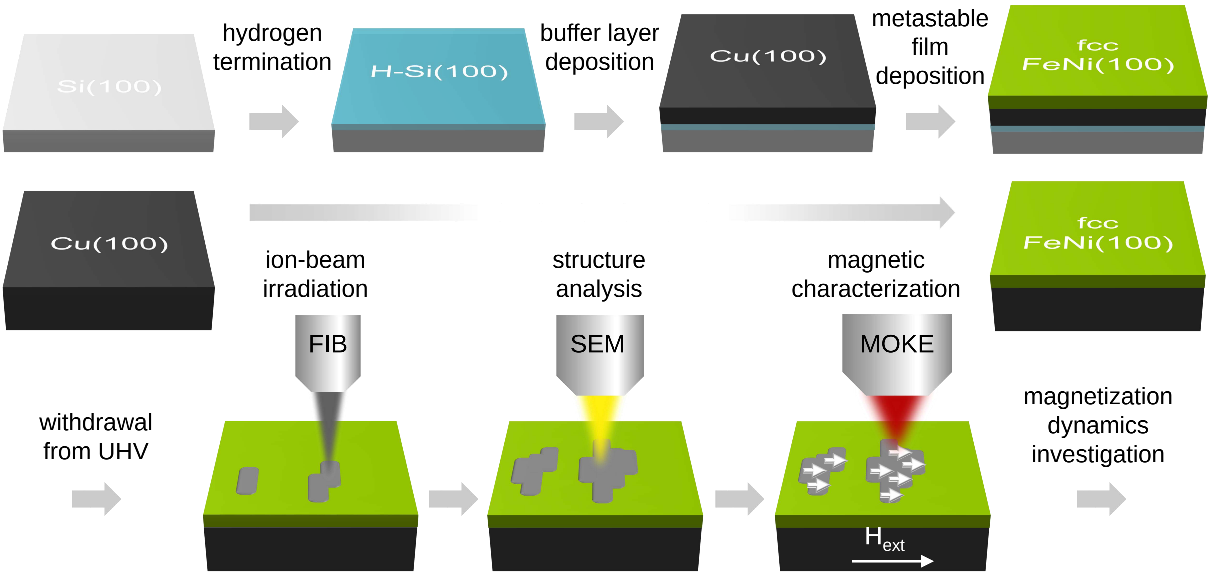

Fig. 2.1: A schematics of the metastable FeNi thin films preparation. The steps of the metastable thin film preparation on the Si substrate is summarized in the first row and the parallel process for the case of a Cu substrate is presented in the second row. Once the metastable thin film is prepared, the sample is taken out from the UHV apparatus and it is patterned by FIB direct-writing. The structural as well as the magnetic properties are characterized using the SEM and the magneto-optical Kerr magnetometry (MOKE), respectively. The sample is then prepared for magnetodynamics studies.

procedure in such conditions. However, the work with UHV is challenging and requires a special approach as some technological aspects must be taken into account.

The residual atmosphere is mainly caused by gases permeating through or diffusing out from walls of a UHV apparatus chamber and of surfaces of objects loaded inside the chamber. Therefore, anything transferred to the vacuum chamber from the outside (such as samples and sample holders) has to be properly cleaned prior the experiment itself. All objects loaded into the vacuum must consist of UHV compatible materials exclusively, and they have to be degreased before placing into the vacuum. Usual substrate *preparation* comprises outgassing both the sample holder and the sample followed by one or multiple cycles of sputtering and annealing. Then, the intended material can be deposited on the sample. To ensure flawless preparation, individual steps of the process can be monitored via different characterization methods.

As the preparation of the metastable FeNi thin films is rather complicated, we check the different steps of the procedure by several characterization techniques. X-ray photoelectron spectroscopy and low energy electron diffraction, the most important techniques for us, are briefly described in this section. The thin films preparation itself is carried out by epitaxial growth, which we also introduce to in the following text.

2.1.1 Epitaxial growth

The word *epitaxy* refers to a deposition of a single crystal layer on top of a crystalline substrate. The method of epitaxial growth is extensively used for the thin-film deposition on single crystals in the UHV conditions. The films prepared by the epitaxial growth are chemically pure and of well-defined crystal orientation with respect to the substrate, as the substrate creates a seed crystal for the film which is deposited. If this condition is not met, the thin-film growth is not epitaxial. Generally, it is distinguished between homoepitaxy and heteroepitaxy. In the first case, the deposited film and the substrate are of the same chemical composition; in the later, they consist of different materials.

The material to be deposited is located in the evaporator, either in a form of an evaporation rod or it is placed inside a crucible. First, the material is heated by electrons emitted from tungsten filament in close proximity. Then, the atoms of the heated material are emitted from the evaporator in a form of gas. Most of them remain inside, but some can pass through a collimator and reach the sample surface. Some of the atoms are ionized by collisions with accelerated electrons and a part of them hits the collimator. There they create the electric current which can be measured by a flux monitor. This current is used to control the deposition rate during the process. The evaporator has to be cooled in the course of the deposition, in order to avoid an increase of the pressure. A flow of water or nitrogen gas is typically used for the cooling.

2.1.2 Low energy electron diffraction

Low energy electron diffraction (LEED) is one of the most frequently used techniques for surface analysis. In order to obtain a back-scattered electron diffraction pattern, the investigated sample has to be a crystal with a well-ordered surface structure. LEED can be then used for investigation of the sample surface reconstruction, chemical bonds and also structural changes on the surface.

In the experiment, a beam of low-energy electrons emitted from an electron gun is directed upon a crystal surface at normal incidence. Electron energy is typically in range of $20 - 300\,\mathrm{eV}$. As these electrons collide with the investigated surface, they diffract in various directions depending on sample crystallography and they are accelerated towards a phosphor-covered screen. The diffracted electrons that reach the screen, cause fluorescence of the screen in the places they hit its surface. In this manner, a LEED pattern is created on the screen. The intensity of glow of each spot depends on the electron intensity and the obtained geometrical pattern reflects the atomic structure on the crystal surface in reciprocal space. A more detailed description can be found in Ref. [105].

From the analysis of the LEED pattern spot positions, one can obtain information on the degree of crystallite of the surface. The method also provides information on the size, symmetry and rotational alignment of the lattice unit cell. Moreover, from the intensities of individual spots, it is possible to quantitatively determine the atomic structure of the crystal with an accuracy of a few tenths of an angstrom.

2.1.3 X-ray photoelectron spectroscopy

X-ray photoelectron spectroscopy (XPS) is a widely used method for chemical characterization of surfaces. It is a common tool for a study of an electron structure and a chemical composition of solids or thin films. The XPS provides information about both quantitative elemental composition of materials and about electron bonds. An information depth of the technique is given by electron mean free path, which is usually several atomic layers from the sample surface. Hence, with the information depth of 3-10 nm, the XPS is considered as a surface sensitive technique and it can be as well used to estimate the thickness of thin films. Except for atoms of hydrogen, all elements can be distinguished together with their oxidation state.

Different experimental approaches allow angle-resolved or temperature-dependent measurement and even energy-resolved measurements of adsorbate distribution with lateral resolution down to several microns. Moreover, a depth profiling is also possible when the XPS measurement is combined with ion-milling.

The XPS technique is based on the photoelectric effect, i.e. on the emission of photoelectrons created by incident photons. In the experiment, a sample surface is excited with characteristic X-rays incoming from a monochromatic X-ray source causing the emission of photoelectrons from core levels of the sample. These photoelectrons are focused and collected by an electron energy analyzer. Only those of desired kinetic energy can pass and continue towards a detector, and hence contribute to the measured signal. From kinetic energy measured by the analyzer, electron binding energy is directly obtained. Then a photoelectron spectrum is recorded over a range of electron kinetic (or binding) energies. In the spectrum appear peaks that are relevant to the surface atoms emitting photoelectrons of distinct energy. Material composition can be identified from the peak positions, chemical bond from the peak shift and quantity of a detected element is determined from the peak intensity.

2.2 Epitaxial iron films on copper

The system of Fe thin-film epitaxially grown on copper single crystal – Cu(100) – has been extensively studied over past decades due to its potential for growth of metastable face-centered-cubic (fcc) Fe even at low temperatures [106–108]. When grown properly the film can be controllably transformed by ion irradiation to the body-centered-cubic (bcc) structure [109]. Such unusual behavior opens up many possibilities for utilization and further investigation.

2.2.1 Metastable thin iron films

As an allotropic material, Fe can be observed in more forms called phases. These differ in their crystal structure and they also exhibit distinct physical properties. In special cases, more than one phase of Fe thin films can coexist under the same conditions. These films are called *metastable*. With the change of pressure and temperature, the Fe films undergo phase transitions, which are affected also by the presence of admixtures and their concentration. At room temperature, pure bulk Fe is observed exclusively in the bcc structure, the α phase. In such case, it is ferromagnetic up to Curie temperature (approx. 770 °C). With the increase of temperature up to approx. 912 °C, it recrystallizes to γ phase characterized by fcc lattice and paramagnetic properties.

The reason for combining Fe with Cu substrate is following. In heteroepitaxial systems, there are always some disturbances at the interface of the layers due to different sizes of lattice constants of the two materials. Therefore, in order to achieve proper epitaxial growth, it is necessary to choose a system made of substances of similar lattice constants.

Restricted to the case of room temperature, the lattice parameter of bcc Fe is 2.68 Å [110] and it is incompatible with the lattice parameter 3.615 Å of fcc Cu, as the difference in their size is 26 % of the Cu lattice parameter value. However, the fcc Fe lattice parameter 3.588 Å [107] almost perfectly fits the one of Cu, as their variation is less than 0.7 %. Therefore, a Cu single crystal exhibiting the fcc structure can serve as a suitable substrate for the epitaxial growth of the fcc Fe films.

Moreover, the fcc Fe thin-film structure varies with thickness depending on the ratio of two major energy contributions. The first one, the energy of deformation, stabilizes the pseudomorphic structure of Fe i.e. the film structure is deformed to correspond with

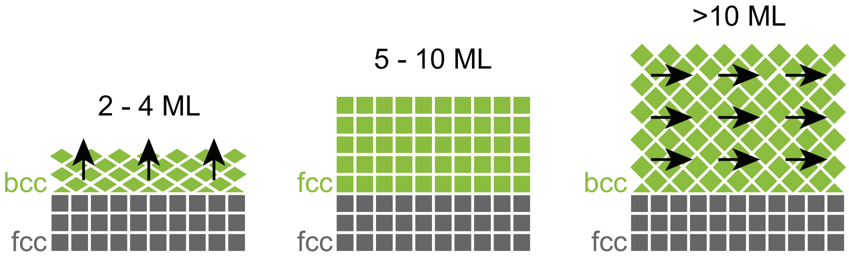

Fig. 2.2: Schematics of Fe/Cu(100) crystal structure, modified from [114]. The first schematics illustrates the earliest stage of growth – the ferromagnetic nanomartensitic structure, the second depicts the pseudomorphic growth of the paramagnetic fcc structure, and the third one depicts growth of the ferromagnetic bcc structure after releasing strain in the Fe layer. In both ferromagnetic growth regimes, preferred orientation of the magnetization vector is indicated by black arrows.

the substrate. The second contribution is the energy given by the crystal structure, which initiates the transition of Fe into the α phase because the bcc structure is more energy-efficient at low temperatures [111]. Depending on the ratio of both energies, three types of structures can be distinguished in different ranges of film thickness, schematically depicted in Fig. 2.2.

In the very beginning of the growth of Fe on Cu(100), a bcc(110) structure is observed up to a thickness of four monolayers (ML) of Fe. The bcc structure is distorted in such way that it minimizes discontinuity of the lattices at the interface and hence the energy of deformation. This structure, called nanomartensitic[1], exhibits ferromagnetism and magnetic anisotropy with an easy axis in the out-of-plane direction [112–114]. Then, a pseudomorphic growth of fcc(100) structure of paramagnetic Fe follows [112, 115]. It is sustainable up to the thickness of 10 ML when the energy gained by the fcc to bcc phase transition overcomes the interface-induced energy of deformation. Finally, the thickness region of paramagnetic Fe ends and the film relaxes back into the bcc(110) structure being ferromagnetic with magnetization lying in-plane of the film surface. The critical thickness at which the transition occurs can vary depending on temperature, on the presence of surfactants, and strain in the film. This structural phase transition ($\gamma \rightarrow \alpha$) is closely linked to magnetic phase transformation (paramagnet → ferromagnet). Similarly, the magnetic properties are connected with the film thickness.

2.2.2 Stabilization of paramagnetic phase

As thin films of pure γ-Fe are stable only below the thickness of approx. 10 ML, it was of major interest to find also possibilities for stabilization of thicker films. The thicker the Fe films are, the less they are prone to oxidation and to mechanical damage, both highly undesirable properties for the further application of the films. Furthermore, thicker films can reach higher magnetic moment after their transformation.

---

[1] A characteristic twin structure that combines local bcc order with a good lattice matching at the fcc substrate interface, a typical sign of bulk martensitic transition occurring on much smaller length scale [112].

Two methods of γ-Fe stabilization were introduced so far. The first alternative is deposition of Fe film in carbon-monoxide (CO) atmosphere [114, 116, 117]. During the deposition, gaseous CO molecules dissociate when they get in contact with the Fe surface. The C atoms incorporate into interstitial sites of the growing layer crystal lattice, where they act as stabilizing agents for the fcc structure growth. Contrarily, the O atoms remain on the surface acting as surfactants; they promote the further layer-by-layer growth of Fe. Unfortunately, the surface is gradually saturated by these O atoms that prevent additional atoms of C to penetrate into the Fe bulk. Therefore, the growth is no longer stabilized and the phase transformation takes place. This fact limits the maximum γ-Fe film thickness to approx. 22 ML [117].

The aforementioned limitation has been overcome by the later method presented by Gloss et al. [3] using Ni as a stabilizing agent. At room temperature, crystalline Ni displays ferromagnetic properties. It is stable in the fcc structure with the lattice parameter of 3.52 Å and its atomic radius is almost no different than the one of Fe. It can be easily bound to the Fe lattice and it can as well take the bcc structure of α-Fe. These properties make Ni an optimal element for alloying with Fe and also a convenient candidate the for fcc structure stabilization.

A phase diagram of an Fe_xNi_{1-x} alloy and stability of each of the two phases in dependence on the Ni concentration were thoroughly investigated. Based on the experimental study, see Fig. 2.3, the region of metastable fcc structure was determined [3]. The exact range of Ni concentrations was found to depend also on the pressure of residual CO gas in the UHV chamber where the growth takes place (Fig. 2.3a). Finally, an optimum was found for 22 % of Ni at 3×10^{-9} mbar of CO. This Ni concentration, which takes place just before the invar region, provides large magnetic moment (Fig. 2.3b). Most often, films of thickness 44 ML were studied [118] but it is possible to grow even thicker films using this method.

Due to the reasons given above, $Fe_{78}Ni_{22}$ (FeNi) has been exclusively used in successive studies.

2.2.3 Transformation by ion beam irradiation

The transformation from the metastable γ to the α phase was initially demonstrated on 8 ML Fe thin film with use of a broad beam Ar ion irradiation [109]. It was later demonstrated on thicker CO-stabilized films using lithographically prepared mask [117] and on Ni-stabilized films using a focused ion beam (FIB) irradiation [118]. The principle of transformation upon ion irradiation was thoroughly studied in last decade.

An atomic structure of thin FeNi (or Fe) film is subject to an interplay of two energy contributions as discussed in Sec. 2.2.1. Fig. 2.4 shows a dependence of total energy on the crystal structure. The fcc structure is, as can be seen from the figure, a local energy minimum of the studied system [120]. On the other hand, the bcc structure is energetically even more favorable and it is a global energy minimum of the system. The

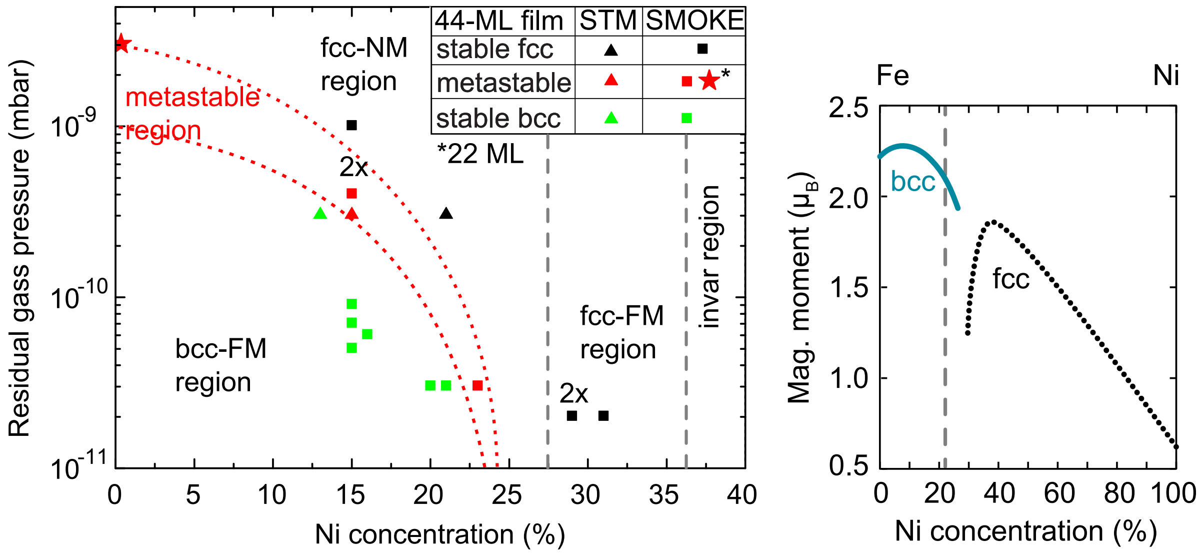

(a) (b)

Fig. 2.3: Diagrams of the structural and magnetic phases of Fe-Ni alloy: (a) Dependence of the structural phase on Ni concentration and on the residual gas pressure during the deposition, modified from [3] and (b) dependence of the magnetic moment on Ni concentration, modified from [119].

graph well illustrates the metastability of the fcc phase. Before the system can relax to the bcc phase, an energy barrier needs to be overcome.

The process of transformation can be explained by the *Thermal spike model*: The extra energy can be delivered to the system by an incident ion. The kinetic energy of the ion is transformed into the thermal energy and it is transferred to an atom it collided with. When a large amount of ions impact at one spot a small volume of material melts and lattice defects are created in its vicinity. In case that the energy obtained by another ion exceeds the energy barrier, a nucleus of bcc structure is created before the molten volume freezes; and with certain probability, it can freeze in a different structure (bcc) than the surrounding (fcc). Many bcc nuclei which grow and coalesce are gradually created in this way forming the new bcc phase embedded in the fcc matrix.

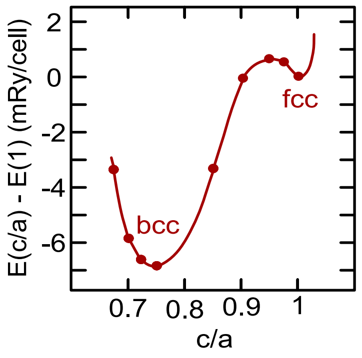

Fig. 2.4: Calculation of the Fe_3Ni alloy total-energy in dependence on the lattice parameters c/a ratio during the fcc-to-bcc structure transformation, in which $c = 2.67\,\mathrm{au}$ and $a = 2.6\,\mathrm{au}$. Modified from [120].

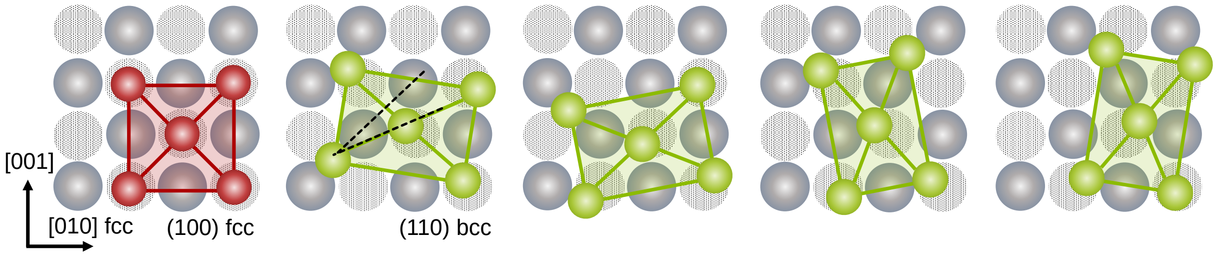

Fig. 2.5: Interface between crystal lattices of FeNi and Cu. The gray lattice represents the last atomic layer of fcc Cu(100) whereas the red and green lattices represent the first layer of metastable fcc (100) and bcc FeNi(110). Four equivalent alignments of the bcc (110) lattice on top of fcc Cu(100) exist. They are rotated by ±19.5° from the fcc $\langle 011 \rangle$ direction, as indicated by the dashed (black) lines.

After recrystallization into the bcc structure, crystal lattices of both adjacent materials no longer match. Instead, there are four equivalent orientations of FeNi(110) lattice on top of the Cu(100) lattice, as was demonstrated using LEED [112, 117]. One of the bcc $\langle 111 \rangle$ directions is parallel with $\langle 011 \rangle$ direction of the fcc lattice whereas the other one is rotated by ±19.5° from the corresponding direction, see Fig. 2.5. It is important to know, whether all four lattice orientations are created in the same proportion or one particular orientation dominates over the others, since the crystal structure is closely linked with magnetocrystalline anisotropy. A strong four-fold anisotropy is expected in crystalline Fe films. We have earlier confirmed the presence of the magnetocrystalline anisotropy in the transformed FeNi thin films [121], which is discussed in further detail in Chapter 3.

2.3 Preparation of FeNi films on different substrates

For the successful preparation of metastable fcc FeNi, flatness and purity of the single crystal substrate are essential. In the following section, experimental treatment of different substrates which allow the fcc FeNi growth is described. In addition to the Cu single crystal, we use also silicon and diamond substrates.

2.3.1 Copper single crystal

Deposition of FeNi directly on the Cu single crystal is the most straightforward approach. Cu crystals of various sizes, shapes, and quality are commercially available. The used substrates are Cu(100) hat-shape single crystals with 4 mm upper and 6 mm bottom diameters, with orientation inaccuracy <0.1° and purity 99.999 % made by MaTecK.

At the beginning of the experiment, the Cu(100) crystal is attached to a degreased molybdenum (Mo) sample plate using two strips of Mo sheet placed from the sides. The crystal cleaning is carried out by cycles of sputtering and annealing inside of a UHV chamber with a base pressure below 5×10^{-10} mbar. A broad beam of 1 keV Ar ions from an electron impact ion source is used for the sputtering at normal incidence. Consecutive annealing is performed using e-beam heater. The temperature is checked by a pyrometer, mounted on the view-port of the chamber, which is directed on Mo sample plate with the set emissivity of 0.8. At the temperature of 600 °C we estimate that the actual temperature of the sample is about 50 °C lower than the one measured by the pyrometer. The whole cleaning procedure is summarized in the following list:

- Mounting the Cu(100) crystal on a sample plate and its insertion into the UHV system.
- Outgassing the sample plate with the sample: It is important not to exceed the temperature of approx. 600 °C, to avoid the risk of melting of the Cu substrate. The emission current corresponding to the required temperature is approx. 15 mA at 1 kV.
- Sputtering the crystal: A typical procedure comprises sputtering for 20 min with 20 µA of 1 keV Ar^+ at 9×10^{-6} mbar.
- Annealing the crystal for 15 min: Heating of the sample is provided by 15 mA electron bombardment at 1 kV which corresponds to the temperature range of approx 550-580 °C.
- Two additional cycles of the sputtering followed by the annealing treatment: It is usual to apply more gentle parameters of sputtering procedure such as 5 min, 15 µA, 750 kV and to perform the annealing at a slightly higher temperature such as 580-600 °C, 17 mA, 1 kV for 15 min.

The final state after the preparation can be checked by LEED and XPS techniques. A typical LEED analysis is performed with the filament current of 1.5 µA, the screen at 6 kV and with primary beam energies in a range of 80-200 eV. For the XPS analysis, aluminum (Al) anode at power 400 W is typically used. Chemical purity of the crystal surface is verified by checking the energy spectra, especially for the presence of O, C, and Mo peaks. When there are no impurities present, we proceed with deposition of metastable fcc FeNi. The procedure is described further at the end of Sec. 2.3.2.

2.3.2 Hydrogen-terminated silicon

As mentioned in the previous section, the system of metastable fcc FeNi on a Cu single crystal has already been thoroughly studied. However, in order to bring it closer toward the application, substitution of the Cu single crystal with a less expensive material is necessary. The most appropriate substitute is of course silicon (Si). It has been the most used material in microelectronic industry for many years and great progress has already been made in the understanding of its material properties and its technological processing. Therefore, possibilities for substitution of the Cu by Si have been explored and it has been shown that metastable FeNi thin films can be prepared on a Cu(100) buffer layer on a hydrogen-terminated (H-Si) surface of Si(100).

The preparation of the epitaxial Cu(100) buffer layer on top of a Si single crystal is rather challenging. The use of regular Si(100) results in the growth of Cu(111) which is the preferred crystallographic orientation of Cu on Si(100). To make the Cu(100) growth possible, the Si substrate needs to be hydrogenated first [122]. The Cu(100) crystal lattice is rotated by 45° with respect to H-Si(100): the [010] direction of Cu being parallel with the [011] direction of Si, and their mutual lattice mismatch is 4-6 %. The H-Si substrate can be obtained by two methods: chemical and thermal. The former is achieved by *ex-situ* hydrofluoric acid (HF) etching and the latter is performed *in-situ* by flash annealing followed by the deposition of atomic hydrogen.

The stabilization of the Cu(100) structure on H-Si was already demonstrated by multiple studies [122–126]. Within these, H-Si was prepared solely by the chemical approach. Metastable fcc FeNi films were also successfully prepared on top of Cu buffer grown with the use of HF etching at TUW[2] [127]. Even though these FeNi films display low surface roughness at a microscopic scale, we have found difficulties with the subsequent investigation of their magnetic properties by the optical method (i.e. MOKE) due to their corrugation on a macroscopic scale. Therefore, it became desirable to use a method of preparation of cleaner H-Si to enable the growth of FeNi films of better surface quality. As a result, the thermal approach was implemented, and it exclusively is used for the preparation of H-Si within the scope of this thesis.

Flash annealing and hydrogenation

Prior the *in-situ* hydrogenation process, Si surface has to be cleansed of native oxide. To remove carbon-dioxide (CO_2) and other carbon contaminants from the Si surface, annealing at the temperature of 1200 °C is necessary. Cleaned surface is then hydrogenated using custom built hydrogen-cracker – a system that heats H_2 gas flowing through capillary to approx. 1700 °C and decomposes it to atomic H. To suppress heating of the sample by hydrogen-cracker, a liquid nitrogen (LN_2) cooled Cu cryo baffle is used.

Hydrogen adsorption sites on the Si(100) surface form a (2×1) reconstruction up to a full monolayer coverage. Additional exposure to atomic H leads to the final state characteristic by a (1×1) reconstruction with saturation point being around 2 ML of H [128]. In such case, the surface is very flat and can be used for epitaxial growth of Cu(100). It was observed that 150 L is sufficient for complete surface coverage by H [129]. However, even more H can be applied with no harm.

Substrates used in the experiment are boron-doped Si(100) with the resistivity of 6-12 Ωm and the thickness of 525 µm. Samples with dimensions of (3×12) mm^2 are cut by laser-dicing. This technique enables preparation of rectangular samples with very straight edges which is a highly important aspect for homogeneous distribution of temperature during the annealing process. The treatment is ensured by direct current (dc) heating

---

[2] One of advantages of using of the chemical approach is the parallel removal of the native oxide and hydrogenation of the surface within a single step of HF etching. Using the thermal approach, this has to be done separately.

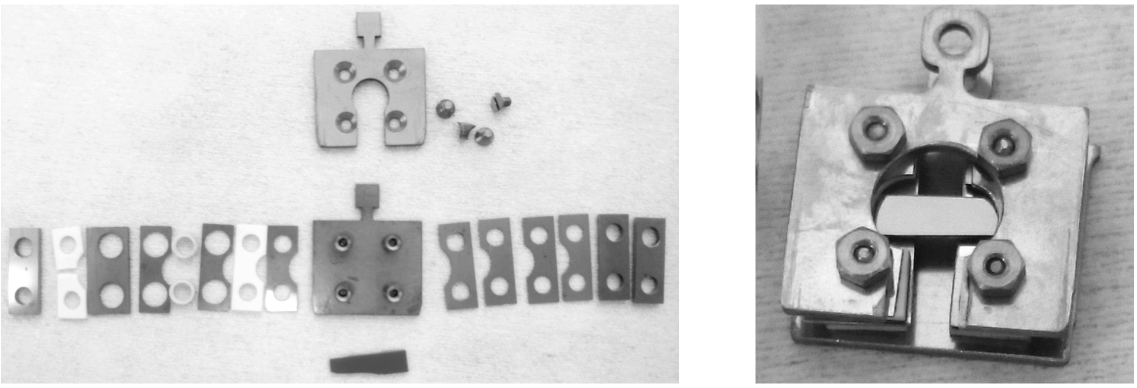

Fig. 2.6: Two similar custom built sample plates for dc heating. The sample plates comprise Mo parts such as sheets, threaded rods with nuts, or bolts with spacers. Ceramics are used to insulate the electrodes. Samples up to $5\times14\,\mathrm{mm}^2$ can be fasten within.

inside the UHV chamber with a base pressure below 5×10^{-10} mbar. Two similar custom built Mo sample plates and a commercial one are used for mounting of the samples (Fig. 2.6). Design of our sample plates is based on the design of the sample holders for dc heating made by SPECS. Temperature is checked by pyrometer directed on the Si surface. Initially, emissivity is set to 0.75 (SiO_2) for outgassing and it is changed to 0.35 (Si) only before the annealing.

The whole cleaning and hydrogenation procedure is summarized in following list:

- Mounting a Si sample on a dc sample plate and its insertion into the UHV system.
- Outgassing the sample plate by e-beam heater: The sample plate containing the sample is heated at the temperature of approx. 600 °Cuntil pressure in the UHV chamber reaches 5×10^{-9} mbar. The outgassing is mostly carried out overnight, as it last several hours.
- Outgassing the sample by dc: The sample is heated with use of a dc power supply at the temperature of approx. 600 °Cuntil the pressure reaches 5×10^{-10} mbar. Corresponding heating power is approx. 5 W, depending on dimensions and resistivity of the sample.
- Cooling a cryo baffle with LN_2: After the outgassing procedure, it is necessary to wait until the pressure decreases below 4×10^{-10} mbar before initiating the celasining of the sample.
- Flash annealing the sample by dc at 1200 °C: Typically, dc is in a range of 9.5-10.3 A depending on parameters of the sample. The annealing temperature is held for 10 s and it is preceded by a 5 s ramp up from the outgassing temperature and followed by a 5 s ramp down to room temperature. The timing is crucial in order to avoid melting the sample and to prevent the formation of silicides. The annealing process can be optionally repeated several times to ensure the sample surface cleanliness.
- Hydrogenation of the sample: The atomic hydrogen exposure takes approx. 420 s. It is achieved with 1 kV H atoms at the pressure of 1×10^{-7} mbar. The supplied

power is typically 18 W but the parameters can slightly vary. On the other hand, keeping the back pressure as low as possible is essential, therefore, the H-cracker has to be well degassed first.

- Surface reconstruction analysis by LEED followed by one shorter hydrogenation step.

After each step of the preparation procedure, inspection of the sample final state by the XPS analysis can be considered. However, it needs to be remembered that each additional treatment can increase contamination of the sample surface. Moreover, the XPS causes partial dehydrogenation and so does the LEED.

Results from analysis of Si sample during the preparation are shown in Fig. 2.7. XPS spectra of Si(100) obtained before and after annealing (Fig. 2.7a) prove the disappearance of O and C peaks – the major surface contaminants. The change of the surface reconstruction from (2×1) to (1×1) caused by hydrogen saturation is further visible in the LEED patterns (Fig. 2.7b). These are obtained before and after the hydrogenation the primary beam energy of 80 eV. Such H-Si(100) substrate is prepared for deposition of the buffer layer.

On the other hand, a remaining contamination, an incomplete hydrogenation, and other deviations result in the growth of a different than the (100) structure. It can be either polycrystalline Cu or the Cu(111) structure.

Several typical issues that can arise during the preparation are listed below together with their causes:

- A substrate of too high resistivity is used. ⇒ dc "breakthrough" cannot be reached.

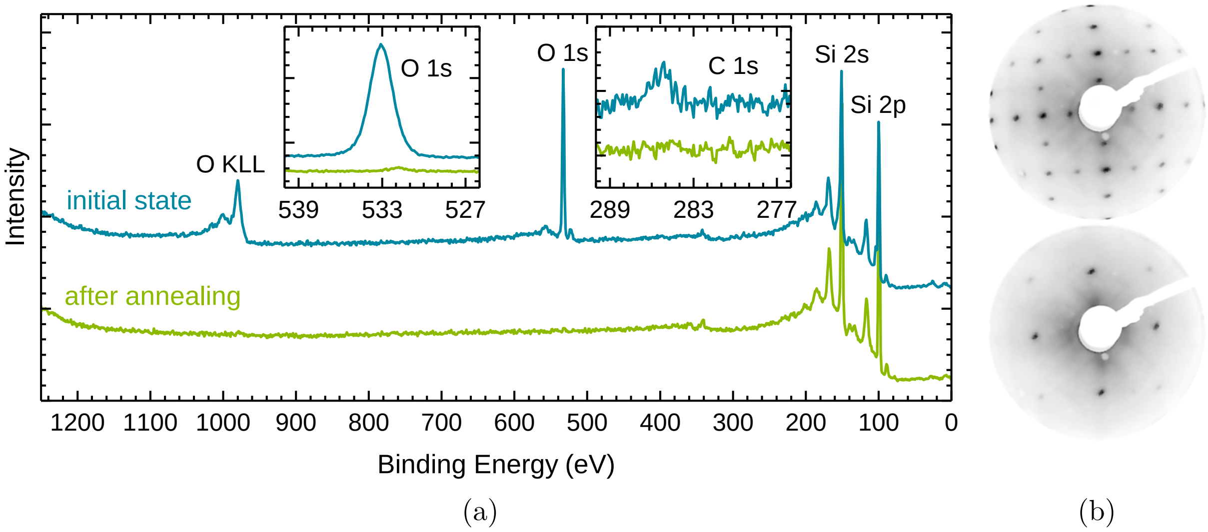

(a)

(b)

Fig. 2.7: Preparation of H-Si(100). (a) XPS spectra of Si(100) sample before treatment and after two cycles of flash annealing at 1200 °C. Insets: details of the O 1s and C 1s peaks. (b) LEED patterns of the (2×1) reconstruction on the Si(100) surface (top) and of the (1×1) reconstruction on the H-Si(100) surface (bottom).

- A sample is incorrectly mounted on the sample plate. ⇒ The measured resistance is infinite and either the dc "breakthrough" cannot be reached or the sample melts/breaks at one of its ends.
- A sample is cut too wide. ⇒ Supplied dc power is not sufficient for reaching 1200 °C.
- Sample edges are ragged. ⇒ Heat is not distributed equally causing melting of the sample on sides.
- The pressure inside the UHV chamber is higher than recommended in different steps of the procedure. ⇒ Defects appear on the Si surface to a greater extent.
- Spots associated with the (2×1) and (1×2) reconstructions are visible at LEED pattern after the hydrogenation. ⇒ The H saturation point was not reached yet.

Buffer layer and metastable thin film deposition

To obtain a homogeneous fcc (100) film of metastable FeNi, a quality of the substrate topmost interface is crucial. So far as it is known, Cu on H-Si(100) grows in an island mode [126] which is connected with grain formation at the Cu/H-Si interface. The grains cause an increased appearance of defects and they induce strain inside the film; then eventually grains of Cu are observed throughout the whole film thickness. Fortunately, the morphology of Cu ameliorates with thickness [130] as a coalescence of the islands and grains can take place. For this reason, relatively thick Cu(100) buffer layers are necessary.

On the basis of our most recent observations, there is another important factor responsible for a proper growth of the Cu(100) structure. During the process of a Cu deposition, a contamination by calcium originating from a crucible of one of the two used evaporators was observed in many experiments. On the contrary, no such contamination was observed when the other evaporator was used. It has turned out that, when the contaminated evaporator was used the growth of the fcc (100) structure was successful. However, with the use of the other evaporator, we were not able to prepare a monocrystalline Cu(100) layer. This result is rather counterintuitive; and moreover, many of earlier experiments relying on the HF etching technique were successful even though the uncontaminated evaporator was used. One of the possible explanations of this behavior is an assumption that the presence of any contamination on the H-Si surface acting as a surfactant is sufficient for initiation of the fcc (100) structure growth. In the case of HF etching, the resultant rough and not entirely pristine surfaces could also be sufficient for an initiation of the Cu(100) growth. However, an evidence for this hypothesis is currently missing, and therefore, the reason why the growth has not been always successful remains an open question.

We continue in the investigation of the problem, as it would help us to better understand the buffer layer growth. Here, we concentrate on the rest of the deposition process, in the way in which it was performed in our laboratory.

A typical thicknesses of the Cu and the FeNi films used within this project are 125 nm and 8 or 24 nm, respectively. Films are grown inside a custom deposition chamber with a base pressure of 5×10^{-11} mbar. The Cu buffer layer is deposited from a crucible and the metastable film is deposited from an $Fe_{78}Ni_{22}$ evaporation rod; Cu from electron beam evaporator EBE-1 by SPECS and FeNi from evaporator FEM 3 by Focus. The deposition rate is checked before the deposition itself by quartz crystal microbalance (QCM) – a resonator that estimates a mass variation by measuring changes in its resonance frequency. A QCM needs to be calibrated and kept at a constant temperature as its resonance frequency is temperature dependent. All depositions are performed at room temperature but the evaporators have to be cooled-down to preserve the pressure inside the UHV deposition chamber during the evaporation in a 10^{-10} mbar range. To make it possible, a LN_2-cooled cryo baffle is used and the evaporator in use is being continuously cooled by the flow of LN_2-cooled N_2 gas. As the FeNi layer is generally deposited immediately after the Cu layer, the procedure is summarized as a whole in the following list:

- Cooling-down a cryo baffle with LN_2 until the pressure inside the UHV deposition chamber reaches 4×10^{-10} mbar and subsequently cooling the Cu evaporator.
- Calibration of the deposition rate using the QCM.
- Deposition of Cu: The supplied power of 18.2 W corresponds with the deposition rate of approx. 0.04 Å s^{-1} which results in a deposition time of 8.7 h for 125 nm of Cu. The pressure has to be kept below 1×10^{-9} mbar in course of the deposition to minimize the number of contaminants.
- Examination of the crystallographic structure by LEED.
- Deposition of FeNi: The supplied power of 14.4 W corresponds with the deposition rate of approx 0.02 Ås^{-1}, which results in deposition time approx. 1 h for 8 nm film. The pressure must not exceed 5×10^{-10} mbar. In case the pressure of the residual atmosphere is lower, gaseous CO is injected as a supplement. The bias voltage 1.5 kV has to be applied to the sample to prevent hitting of the sample surface by the evaporated ions and its instant transformation.
- A final check of the structure by the LEED followed by the XPS analysis of the chemical composition.

Typical measurement results are shown in Fig. 2.8. An important part of the metastable film analysis is the inspection of its chemical composition. Besides contaminants detection, the XPS can be used to estimate the ratio between Fe and Ni in the compound. Surroundings of Fe 2p and Ni 2p peaks are measured with fine step and fitted[3]. From area below the modeled data (insets of Fig. 2.8a), an elemental ratio Fe : Ni can be calculated[4].

Apart from the FeNi film composition verification, the underlying substrates can be investigated before the deposition of the FeNi film. The XPS spectra in Fig. 2.8a elucidate chemical comparability of a Cu single crystal (blue) and a Cu buffer layer on H-Si

---

[3] The spectra are analyzed with use of Unifit XPS Analysis Software.

[4] Estimation of the ratio is 90.8 : 9.2 in the case presented in Fig. 2.8a. Such deviation from the expected composition 78 : 22 can be explained either by the data misinterpretation caused by insufficiently wide energy range around the Ni 2p peak, or by inappropriate evaporation conditions resulting in composition variation of deposited material.

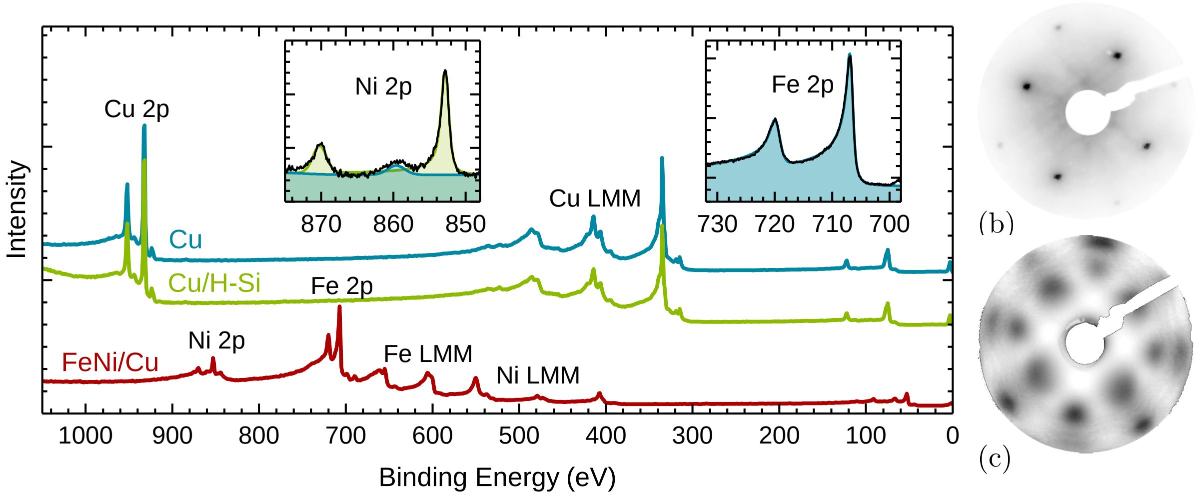

(a)

(b)

(c)

Fig. 2.8: Comparison of epitaxial Cu(100)/H-Si and Cu(100) single crystal substrates. (a) XPS spectra of both substrates prior deposition of metastable FeNi and of the deposited 8 nm-film on top of Cu(100) buffer layer. Magnesium (Mg) anode at 300 W is used. Insets: details of measured and fitted Ni 2p and Fe 2p peaks. (b) LEED pattern of Cu(100) single crystal at 150 eV primary beam energy. (c) LEED pattern of 125 nm Cu(100) buffer layer at 130 eV prepared and measured by J. Gloss at TUW.

(green); and oppositely, LEED patterns (Fig. 2.8b and 2.8c) reveal the difference in the surface quality of both substrates. Blurry diffraction spots in the Cu/H-Si case indicate significantly rougher surface than in the case of Cu single crystal. Despite their structural difference, magnetic properties of the FeNi films on both substrates are similar in many aspects. The relation of the structural and the magnetic properties is described in Chapter 3.

2.3.3 Perovskite oxides and diamond

There are several other materials that can be considered as candidates to substitute Cu(100) single crystal. The main selection restriction is their structural lattice match with fcc FeNi.

The first possibility is provided by perovskite oxides $SrTiO_3$ and $LaAlO_3$ that were already used for the Cu(100) growth [131]. It is possible to prepare them in form of thin films on Si single crystal substrate [132], thus they are compatible with current semiconductor microelectronics. In the past, $SrTiO_3$ was used as a substrate. However, the preparation of metastable FeNi thin film on this substrate has not been successful. As an oxide, $SrTiO_3$ is characterized by lower surface free energy compared to metallic Cu. Hence the Cu buffer layer grows in an island-growth mode on top of this oxide. It was observed, that these islands and grains are too large, and therefore, they prevent the creation of a Cu(100) single crystal layer.

Another substrate suitable for metastable thin film growth is diamond [133]. In contrast with Cu, diamond is extremely durable, it provides a band gap as large as 5.5 eV, high thermal conductivity, and transmissivity in both visible and X-ray spectra. Moreover, single crystalline C(100) can be prepared even as a free standing membrane which makes it a good candidate to be investigated by X-ray techniques. A very small lattice mismatch at the fcc Fe/C(100) interface ensures that it does not need to be used together with Cu(100) buffer layer, which also makes C a good alternative to Cu or Si.

The preparation of metastable FeNi on top of diamond was successful at TUW and one prepared FeNi/C(100) sample was investigated within the framework of the project. A diamond single crystal of dimensions $(4\times4)\,\mathrm{mm}^2$ and the thickness 1 mm was used as a substrate for the growth of the metastable thin film. The preparation process was performed with use of a following procedure.

The C(100) substrate was etched in 20% HNO_3 and then cleaned by sonication in deionized water. Next, it was mounted on a sample holder and loaded into a UHV system. After the outgassing procedure, the substrate was annealed at the temperature of 700 °C. The chemical purity of the cleaned substrate was checked by Auger electron spectroscopy. The 8 nm thick FeNi film was then evaporated by the same procedure as described in the Sec. 2.3.2.

3 Preparation of spin wave source and propagation media

The chapter is divided into two main blocks: patterning of metastable FeNi using the FIB and preparation of waveguides for spin wave excitation and detection. The patterning possibilities and the process of micropattern preparation are described in Sec. 3.1. Magnetic properties observed in the prepared films and their relation to the morphology is discussed in Sec. 3.2. Nanofabrication of coplanar waveguides using electron beam lithography is described in Sec. 3.3 and the design of the prepared waveguides is presented. In Sec. 3.4, the experimental setup and the experiment are outlined.

3.1 Ion beam direct writing

A second stage of the preparation process of the magnetic media for spin wave propagation starts by taking the sample with deposited metastable FeNi thin film out of the UHV complex. The preparation and the successive experiments are performed using following samples: 8 nm thick films of FeNi grown on Cu(100) and on C(100) and FeNi/Cu(100)/H-Si(100) samples with the thickness of the metastable thin film of 8 and 24 nm. All the used thin films on hydrogenated Si, a sample on C and some of the films on Cu single crystal were prepared by the colleagues at TUW. Nevertheless, their complete characterization and all the results presented in the following sections are carried out in our laboratory.

The transformation by FIB irradiation is performed with two FIB-SEM dual beam systems: TESCAN Lyra3 and FEI Helios 660. Both the instruments use Ga ions accelerated up to the energy of 30 keV and enable selection of the probe current in the range of approximately 1 pA to 50 nA. Other customizable parameters include: both a normal and an oblique ion beam incidence, a dwell time of the ion beam at one spot down to 0.03 µs, a lateral distance between the irradiated spots down to nanometers, number of passes of the beam and the beam trajectory.

The influence of the ion energy on the transformation of Fe and FeNi thin films was already investigated [114, 118]. In accordance with the earlier findings, we keep the same ion acceleration voltage 30 kV in all experiments. The high energy provides the best writing lateral resolution and the Ga ions of 30 keV can penetrate through the whole thickness of the metastable film or even deeper into the substrate. Therefore, the film can be transformed as a whole. We change all the other parameters according to a particular application.

The possibility to direct write magnetic patterns by the FIB is a unique property of our system and this method of magnetic nanopatterning is very advantageous is several aspects. First of all, it is fast and easy. As a single-step technique, it allows much easier patterning than conventional technique relying on the EBL, which usually require multiple patterning steps followed by a lift-off or an etching process. Second, it provides a vast range of patterning options. Due to all the mentioned parameters that may be changed, various magnetic structures can be written quickly and with reasonable resolution starting from millimeter-sized patterns and ending with sub-100 nm elements. In the previous study, we used an ion current of 3 pA to transform a lattice of magnetic nanodots with a diameter of approx. 80 nm [121]. Third, magnetic structures are written without any significant modulation of the film surface. Thus, the transformation process can produce discrete magnetic patterns embedded in a continuous paramagnetic matrix. Last, continuous transitions between the ferromagnetic and the paramagnetic material can be made as a result of partial transformation; in contrast with the EBL or the optical lithography processes which produce mainly patterns with sharp step-like edges. Also the possibility of a gradual change of the saturation magnetization at structure border can be used with benefit in magnonics, for instance, for preparation of graded-index magnonic elements [134].

3.2 Thin films pre-characterization

Before initiating the experiments with spin waves, the properties of the prepared films need to be well understood. Only then, we can appropriately use their rather unusual potential and we can also be aware of some limitations.

3.2.1 Transformation efficiency

First of all, we determine the range of ion doses upon which the transformation of FeNi/Cu(100) occurs. For this test, we irradiate a series of 12 µm patterns, each by different amounts of ions in the range of 1×10^{9} to 5×10^{17} ions/cm^2, beam current 145 pA (beam spot size of approx. 30 nm) and scanning step size 10 nm. Based on our previous results with FeNi/Cu(100), an optimal ion dose in the order of 10^{15} ions/cm^2 is expected and potential influence of the FIB scanning strategy is taken into account. Therefore, we carry out the same experiments for patterns irradiated along isotropic scanning trajectories either by a single scan or by multiple scans of shorter dwell times.

Immediately after the transformation, we image the irradiated patterns by SEM. We cannot detect changes in topography, but we can observe the contrast change between the irradiated and the unirradiated areas using an electron beam accelerated by 5 kV and detected by Everhart-Thornley secondary-electron detector. Upon slight tilt of the sample from the normal direction, the observed contrast reverts with the change of azimuthal angle. In transformed areas, the strongest contrast change is observed at 10° inclination and the reversal appears with a six-fold symmetry in a full rotation. This indicates its connection to the crystal lattice of the bcc structure. Indeed, the behavior can be

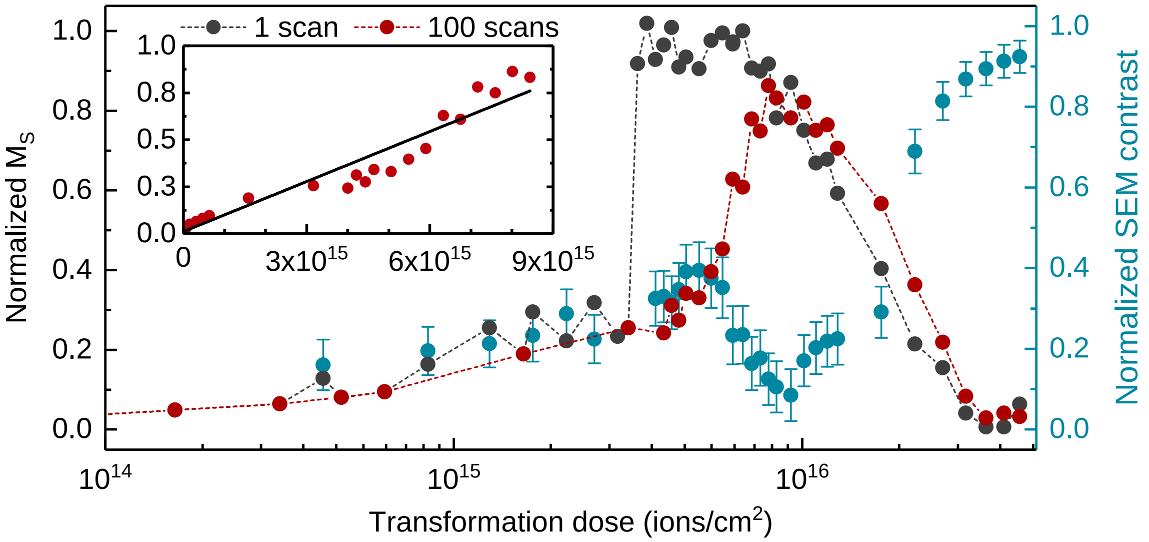

Fig. 3.1: Ion dose test for the 8 nm thick FeNi film on Cu(100). Dependence of the normalized saturation magnetization on ion dose used for transformation by two FIB scanning strategies: a single scan (gray) and 100 scans (red) with the same total irradiation times. Inset shows the initial part of the dependency in a linear scale and a linear fit indicating the constant transformation efficiency with the ion dose. Dependence of contrast changes of the 100-times scanned structures on the ion dose imaged by secondary electrons (blue) reflects the magnetization state. The irradiated areas turn lighter with ion dose up to the an abrupt (bright-to-dark) contrast reverse; at that point the full saturation is reached. Then the irradiated areas lightens up again, as FeNi is being sputtered away.

explained by the electron channeling through the transformed material [135]. Apart from distinguishing between irradiated and unirradiated areas, it can be used to distinguish between the four structural domains (presented in Fig. 2.5) upon tilting the sample. Hence, the SEM is a powerful tool for monitoring of the structural (and also magnetic) phase transformation already during the FIB transformation without removing the sample from the instrument.

To probe the magnetic properties, we use two instruments based on magneto-optical Kerr effect: a custom built micro-Kerr magnetometer [136] and a wide-field Kerr microscope by Evico magnetics. Neither of these techniques can provide the absolute value of saturation magnetization. Instead, they measure quantities, called Kerr rotation and Kerr ellipticity, which are proportional to the saturation magnetization.

In Fig. 3.1, the result of the experiment is presented. Using either of the scanning strategies single- or multiple-pass scanning, the magnetization initially increases linearly with the ion dose, as indicated by the inset plot with the linear x-axis scale. At 3×10^{15} ions/cm^2, however, a difference between the two approaches arises. When the film is irradiated by single scan strategy (gray dataset) an abrupt increase of the saturation magnetization toward its maximum occurs. On the contrary, upon irradiation by 100 fast scans over the area (red dataset), the magnetization smoothly increases with the dose up to 8×10^{15} ions/cm^2. Then it unites with the first dependency. Using each of the strategies, the magnetization decreases and it reaches zero at 4×10^{16} ions/cm^2. By that

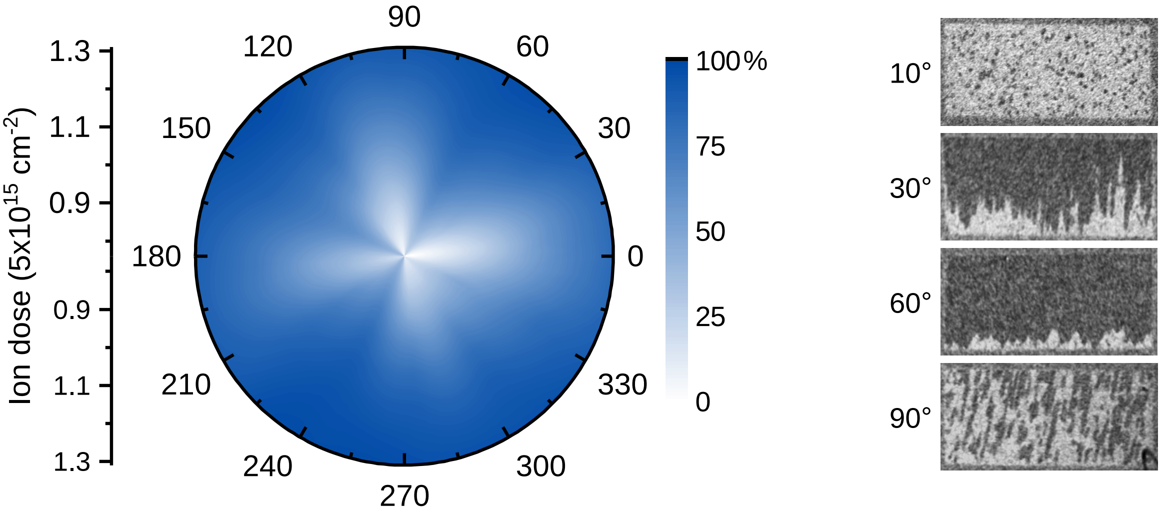

Fig. 3.2: Angular dependency of transformation efficiency. A fully transformed part of the area plotted in dependence on ion dose used for the transformation and the angle between the fcc [010] and the scanning directions. SEM micrographs of $6\times14\,\mu$m rectangles oriented in 10°, 30°, 60° and 90° from the fcc [010] direction, each irradiated by the same ion dose 5×10^{15} ion/cm^2 from the bottom side up. The transformation is uninitialized in the bright parts and oppositely, the dark part indicate the full transformation into the bcc phase.

point, the FeNi film is completely sputtered away. The change of contrast imaged by secondary electrons is plotted for the dataset of the 100-times scanned structures. The irradiated areas turn slowly brighter with low ion doses and they suddenly darken when the optimal ion dose is reached. The areas light up again as the Cu substrate is being gradually exposed.

We further studied the sudden change of transformation efficiency in the case of a single scan strategy. Due to the present magnetocrystalline anisotropy of a four-fold symmetry, we expected a variation of transformation efficiency with an angle defined by the FIB scanning direction and the easy (or hard) axis. We irradiated a series of $6\times14\,\mu\text{m}^2$ rectangles by linear scanning along their long side by different ion doses. The rectangles were oriented so that different angles were enclosed between the longer of their sides and the fcc [010] direction (easy axis). We confirmed the orientation dependence of the transformation efficiency and its four-fold symmetry. This is visible in Fig. 3.2 representing the percentage of the irradiated area which is fully transformed into the bcc phase. A selection of four rectangles irradiated by 5×10^{15} ion/cm^2 and labeled by their orientation with respect to the fcc [010] direction is also shown. Dark spots indicate fully transformed parts, bright parts are not yet transformed even though they are irradiated. These patterns were scanned from the bottom edge up, and therefore, the bcc structure nucleation starts from there. Once the transformation is initiated, the bcc structure grows in triangles beginning at each nucleation site. With further scanning of the FIB, the triangles coalesce and form continuous bcc structure, as is visible in micrographs labeled 30° and 60°.

The situation is quite similar in the case of FeNi/Cu/H-Si. We performed the experiment for samples of both thicknesses of FeNi films in order to find the optimal ion dose

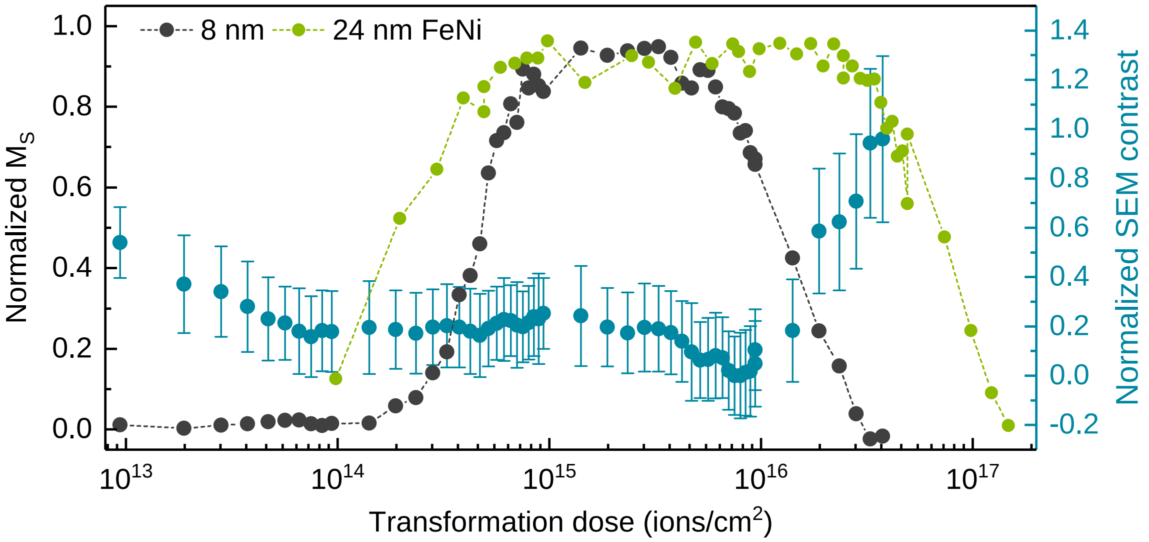

Fig. 3.3: Ion dose test for FeNi/Cu(100)/H-Si(100) samples with 8 and 24 nm of FeNi and a dependency of contrast changes in the 8 nm film imaged by the SEM. Patterns are irradiated by a single isotropic scan by the FIB over their area.

for each. Fig. 3.3 shows the dependency of the normalized magnetization on ion dose. A dataset of normalized contrast imaged by secondary electrons corresponds to the irradiated patterns in the 8 nm film. There are no apparent changes of contrast up to the point of FeNi film removal, nor there is visible a variation with the scanning strategy. Therefore, the degree of transformation can be only roughly estimated using SEM, as is apparent from the dependence in the plot. Besides, individual structural domains of the group of four are visually indistinguishable using SEM only which makes the characterization more complicated.

Instead, we observe faster onset of the full magnetic saturation and a plateau stretched up to higher ion doses than in the case of FeNi/Cu(100). The initial transformation efficiency is isotropic and the same for both films grown on the H-Si substrate. The optimal transformation is reached already by 1×10^{15} ions/cm^2 and the magnetic signal measured by Kerr microscopy is constant over a range of more than an order of magnitude higher dose. Therefore, the choice of irradiation dose is less strict than when using the Cu substrate.

Finally, it is worth to refer to the FeNi/C(100) system. This sample differs significantly from the others on Cu and H-Si substrates. Mere SEM micrographs of an unirradiated film uncover a difference in its morphology, see Fig. 3.4. As it is noticeable from the images, FeNi does not form a continuous film but instead the whole C(100) surface is covered by microscopic islands and clusters of FeNi.

Nonetheless, we performed the same experiment as with the other samples. We irradiated analogous series of structures to those on Cu and H-Si substrates and analyzed them using the micro-Kerr magnetometer. However, we observed Kerr ellipticity not higher than 0.03 mrad which is 13 times less than the highest value (0.4 mrad) measured in transformed FeNi/Cu(100). Furthermore, we experienced major difficulties with a scat-

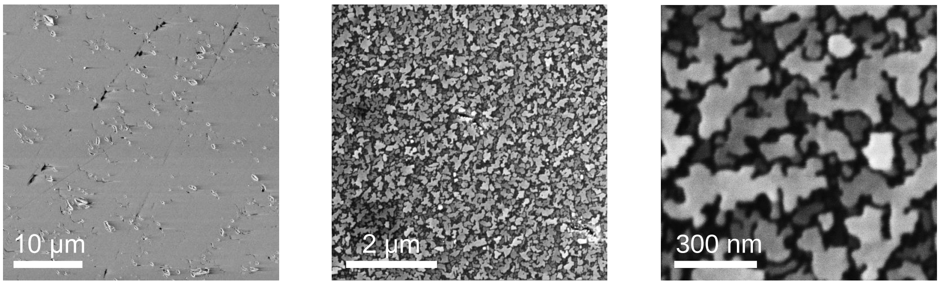

Fig. 3.4: SEM micrographs (from the left): overview micrograph of the clean C(100) surface and the FeNi/C(100) and a detail image showing clusters of FeNi on the C(100) substrate.

tering of the probe on the film surface. These can be addressed to the morphology. Based on these observations, we decided not to carry on with the FeNi/C(100) research.

3.2.2 Morphology of the thin films

Morphology of the substrate is an important factor influencing the final quality of the FeNi films. Based on our previous results from LEED, quality of the Cu(100) surface is very different between the Cu single crystal and the Cu buffer layer grown on H-Si, see Fig. 2.8b and 2.8c. Moreover from the SEM observations of the FeNi films, the difference in their structural quality depending on the underlying substrate is distinguishable. And finally, the magnetic properties of the films prepared on Cu and on H-Si partially differ.

We investigate surface qualify of our samples using atomic force microscopy (AFM). Even more important than an initial state of the films is the final quality of the surface they obtain during the transformation process. Therefore, we compare the surfaces in the two cases side by side in Fig. 3.5. All micrographs are measured under the same conditions on two adjacent $(1{\times}1)\,\mu\mathrm{m}^2$ areas of each sample, but one of each pair is irradiated by approx. $10^{15}\,\mathrm{ions/cm}^2$. There is an indisputable difference between the film on Cu and on H-Si. The first film is perfectly flat except for a few step bunches and contaminants (Fig. 3.5a). The latter reveals a nano-grain structure (Fig. 3.5b and 3.5c).

Deterioration of the film on Cu single crystal upon ion irradiation is apparent, less can be concluded from the other two pairs of micrographs. Hence, to estimate the roughness from the micrographs, we perform a quantitative analysis of the height distribution over each one. The obtained height distributions are presented in graphs 3.5d and the results summarized in Tab. 3.1. The surface of FeNi film on the Cu substrate is 15× less rough than the same film on H-Si substrate and its roughness is significantly increased by the transformation. On the contrary, the roughness of FeNi on H-Si is slightly decreased by the ion irradiation. The reason for this behavior may be related to the grain intermixing caused by the incident ions. On top of that, a better quality surface is observed in the case of 24 nm thick FeNi film when compared to the 8 nm film. This indicates a coalescence of the grains during the FeNi film growth. Such behavior can be expected and it suggests that the morphology improves with the thickness of both the buffer layer and the metastable film.

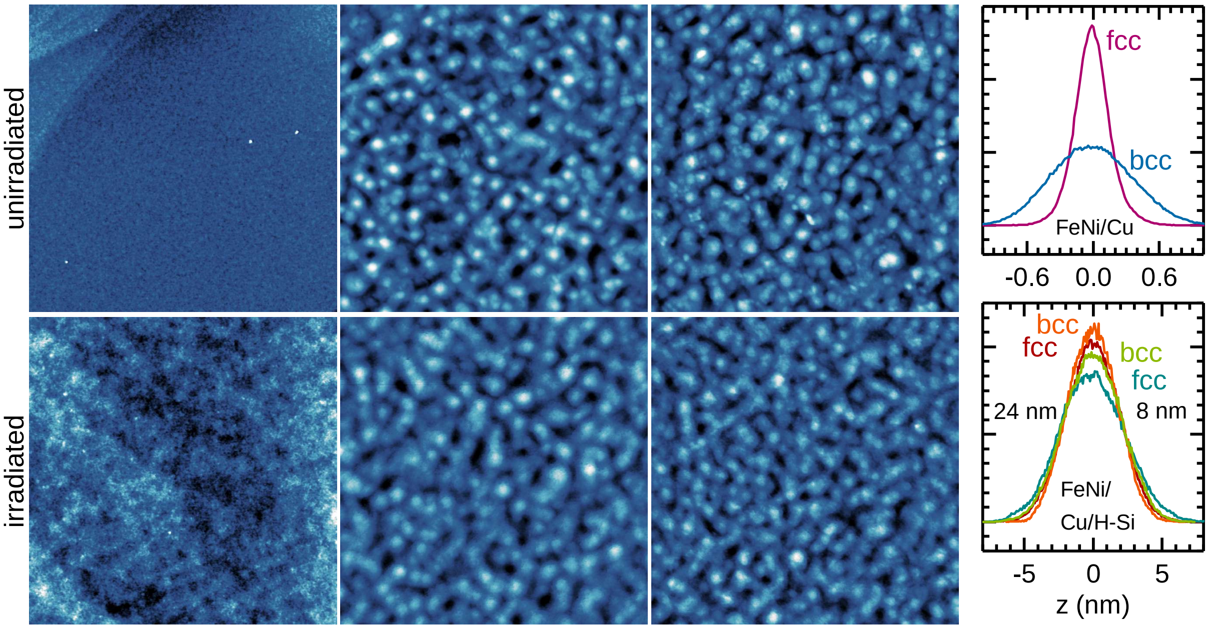

(a) 8 nm FeNi/Cu (b) 8 nm FeNi/Cu/H-Si (c) 24 nm FeNi/Cu/H-Si (d)

Fig. 3.5: (a)-(c) Topography of as deposited metastable fcc FeNi (top row) and bcc FeNi (bottom row) after the FIB irradiation. All AFM micrographs have the same lateral scale 1 µm and different z-scales: (a) 2.2 nm (b) 13 nm and (c) 11 nm. (d) Height distribution calculated over images (a)-(c): Surface of FeNi on Cu (top) and FeNi of two different thicknesses on hydrogenated Si (bottom).

Tab. 3.1: Height distribution calculated over area 1 µm^2 obtained before and after irradiation of FeNi thin films by Ga ions.

sample designation	as deposited: FWHM (Å)	after irradiation: FWHM (Å)
8 nm FeNi on Cu(100)	3.4±0.015	8.7±0.029
8 nm FeNi on H-Si(100)	55.9±0.29	49.8±0.16
24 nm FeNi on H-Si(100)	46.4±0.14	43.6±0.18

3.2.3 The effect of anisotropy

As mentioned in the previous chapter, the four-fold magnetocrystalline anisotropy is an intrinsic property of crystalline Fe films and we have observed it also in FeNi thin-films on Cu during our previous studies [121, 137]. We have found a magnetic anisotropy of four-fold symmetry apparently connected with the crystallographic directions of the substrate, which is weaker than the anisotropy expected in a pure Fe single crystal. We have also observed that there is a dependence of the anisotropy symmetry on the FIB scanning direction through the irradiated area.

Different results are obtained, if a pattern is irradiated by isotropic (such as circular) scanning of the FIB or if an anisotropic scanning strategy (such as linear scanning) is used. In the former case, the magnetic anisotropy of the four-fold symmetry is observed. In the latter case, a uniaxial magnetic anisotropy is observed.

It has been found out that directions of the easy axes lie in $\langle 010 \rangle$ directions of fcc lattice. The reason for this behavior was found in the transformation process itself. By the FIB scanning strategy, we are able to select which of the four structural bcc domains are created to what extent. Therefore, when all four domains are equally represented in the transformed area (by the isotropic scanning), different anisotropy contributions add up forming a four-fold anisotropy with the easy axes in the fcc $\langle 010 \rangle$ directions. On the contrary, when only two out of four structural domains are created, the resultant anisotropy is uniaxial.

This behavior can be demonstrated by transformation of two areas on the sample by the same ion dose $2{\times}10^{15}$ ions/cm^2 by a single linear scan, however, each one by different angle of the FIB scanning. The anisotropy is then investigated with the use of the Kerr microscopy: Magnetic field was applied in different angles with respect to the [010] crystallographic direction of the sample and a hysteresis loop was taken for each of the orientations with a step of 10°. The remanent magnetization of all hysteresis loops were then plotted against the direction of the applied field. The easy and hard axes can be easily distinguished from the polar plots, see Fig. 3.6.

This experiment was repeated for different FIB scanning directions and the easy axis orientations were analyzed in each case. It was observed that even though the direction of the easy axis is to a great extent controlled by the fcc $\langle 010 \rangle$ directions, its precise orientation varies as a function of the angle between the FIB scanning and the crystallography. A variation was found to belong into a range of ±10° around the $\langle 010 \rangle$. As can be seen from Fig. 3.7a, the angle smoothly rotates with rotation of the FIB scanning and then it suddenly jumps to the proximity of the other preferred orientation. This highly interesting finding has opened numerous possibilities for application of the metastable FeNi in magnonic element design.

The same anisotropic behavior has been tested on the 24 nm thick FeNi film prepared on H-Si. The presence of the anisotropy connected with the crystallography have been

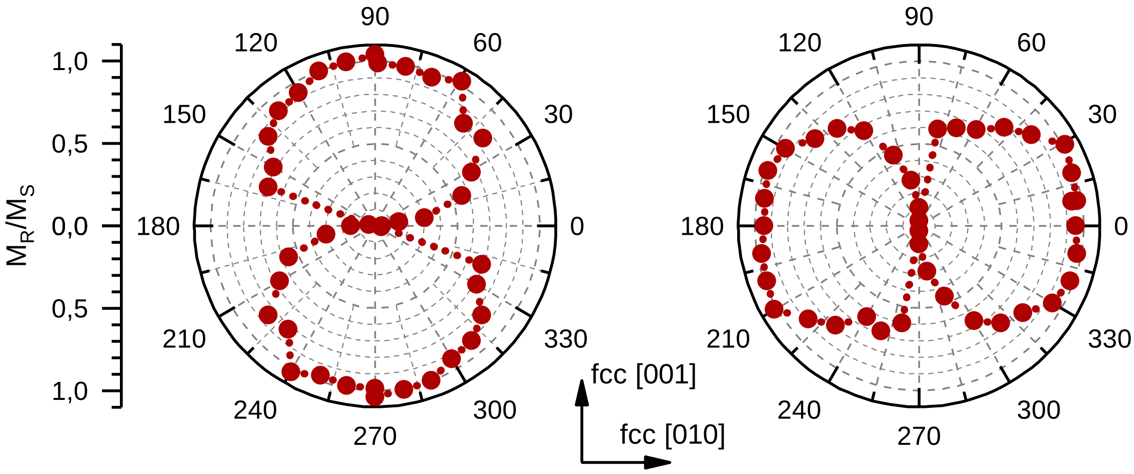

Fig. 3.6: Polar plots of remanent magnetization normalized to the saturation for two areas transformed by the FIB scanning in two directions perpendicular to each other, measured by L. Flajšman.

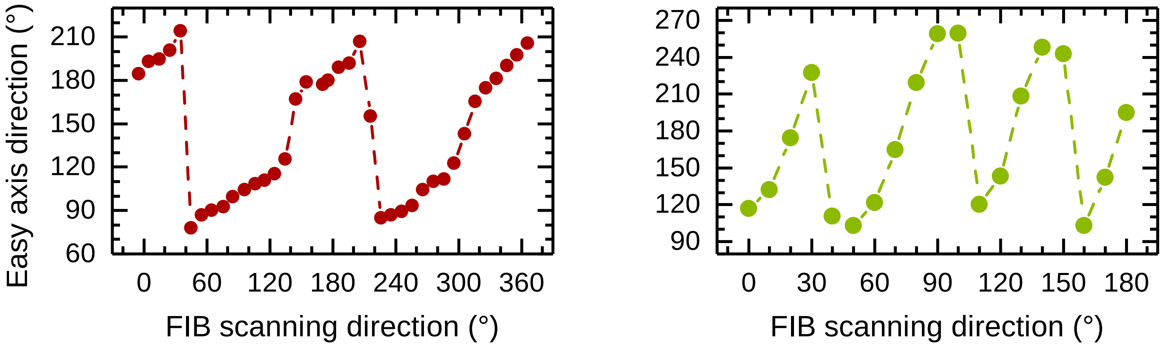

(a) (b)

Fig. 3.7: The direction of the magnetic easy axis as a function of the angle of the FIB scanning direction with respect to the fcc [010] (a) for the FeNi/Cu and (b) the FeNi/Cu/H-Si. The data were measured and analyzed by L. Flajšman.

confirmed, although not to the same extent as in case of the Cu substrate. From the preliminary results, it seems highly probable that the anisotropy can be tailored by the FIB scanning even in this type of sample (Fig. 3.7b). Unfortunately, it is not possible to distinguish between the bcc structural domains by the crystallographic contrast directly by the SEM. Anyhow, there is still plenty of space for further investigation until the true potential of the metastable thin films on H-Si is fully explored.

3.3 Sources and detectors nanofabrication

Excitation and detection of SWs is carried out with a series of CPWs prepared by standard EBL technique and followed by a deposition of the conductive material via an electron-beam evaporation. The waveguides are made of a titanium (Ti) adhesion layer and a gold (Au) conductive layer. The prepared CPWs (with the exception of the area of contact pads) are covered with an insulation layer of SiO_2. Then, they are wire-bonded to an adapter made of a double sided Cu clad board. A schematics summarizing the whole preparation procedure, described in detail in the text, is presented in Fig 3.8. We should remark, that when the CPWs are lithographically prepared directly on top of the magnetic (conductive) material, the order of the preparation process is reversed. Naturally, the SiO_2 insulation layer has to be deposited below the CPWs and there is no further necessity to cover the Au layer.

The substrate, which we use in most of the cases for the CPW fabrication is gallium arsenide (GaAs), the most widely used substrate for hf applications nowadays. GaAs is preferably utilized when low noise signal, high electron mobility and low dielectric loss are needed. Therefore, we use GaAs as a dielectric substrate for all the PSWS experiments, as the detected signal is highly attenuated by the propagation in such case. However, for FMR measurements where wider waveguides are utilized and the signal detection is easier, we use less expensive Si wafers covered by 285 nm thick SiO_2 layer as the substrate. The fabrication process is summarized in several steps as follows:

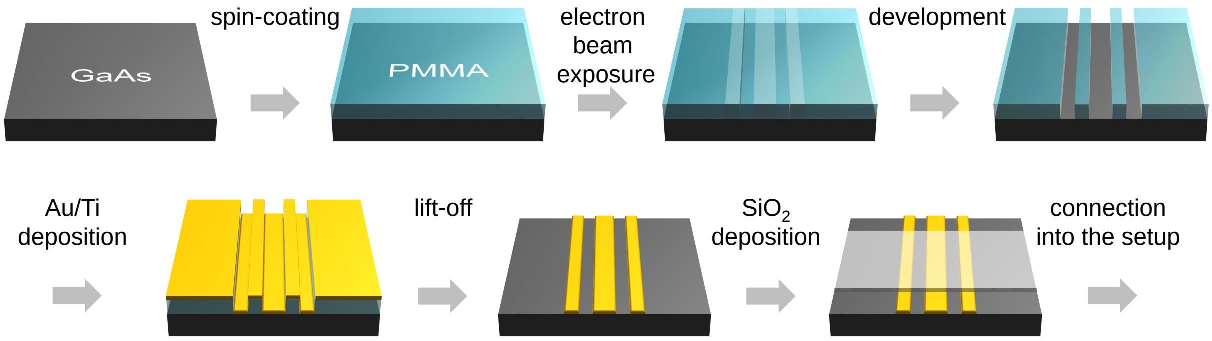

Fig. 3.8: A schematics of the CPW preparation process: A GaAs substrate is cleaned, coated with PMMA-based resist and exposed to an electron beam irradiation. After the resist is developed, the adhesive Ti layer and the Au layer are deposited from an electron-beam evaporator. The lift-off is performed with the use of an acetone bath. The prepared waveguide is partially covered by an insulation and it can be used in magnetization dynamics experiments.

- The GaAs (or SiO_2/Si) wafer is cut into (5×5) mm^2 rectangles by laser-dicing and it is thoroughly cleaned by the sonication in acetone and isopropyl alcohol (IPA) bath.
- The well-cleaned substrate is pre-beaked at the temperature of 150 °C and coated by resist based on Poly(methyl methacrylate) (PMMA), commercially available as AR-P 679.04 from ALLRESIST. After the spin-coating at 2500 rpm for 60 s, the substrate is post-baked at 150 °C for 180 s.
- The substrate is irradiated by electrons accelerated by the voltage of 20 kV with the use of an electron-beam writer TESCAN Mira3. A dose of 270 µC/cm^2 was found to be optimal for the exposure of the whole thickness of the resist. To limit the emergence of optical aberrations during the exposure, the area of the waveguide is stitched up from numerous (100×100) µm^2 write-fields.
- The exposed pattern is developed for 100 s by bathing in commercial developer AR-P 600-56, followed by bathing for another 60 s in IPA, which is used as a stopper.
- Plasma etching for 60 s in 80:20 Ar:O_2 plasma is carried out to assure removal of all residues of the resist from the exposed area.
- Deposition of Ti and Au is performed in an electron-beam evaporator with the base pressure of 1×10^{-8} mbar. The thickness of the deposited adhesive Ti layer is typically 5 nm and it is succeeded by deposition of 140 nm of the functional Au layer.
- The lift-off procedure consists of an acetone bathing for several hours and following sonication and cleaning by IPA. The long-lasting lift-off process is necessary to enable acetone to penetrate in between the long and narrow conductive lines of CPWs.
- Prepared waveguides are checked by an optical microscope and the widths of their lines are measured. The contact pads of the waveguides are then covered, for in-

stance, by a Kapton tape and a 40 nm thick insulating layer of SiO_2 is deposited over the unprotected part of the sample surface.

In order to investigate the magnetic material attenuation properties, PSWS experiments need to be performed using pairs of CPWs with different distances between the transmitter and the receiver. Therefore, we pattern four pairs of the CPWs with different mutual distances side by side on a single substrate, to ensure that all conditions are as similar as possible in all the four waveguides.

There is also a minor disadvantage of using of a single substrate to host multiple CPWs when a wire-bonding technique is used for contacting. The bonds need to be removed from the first CPW before a new one can be connected. On the contrary, the scheme of more CPWs on a single substrate provides an additional benefit when a probe station for microwave probing – more common tool for hf measurements – is employed. To contact the CPWs, the probes can be easily moved between the CPW pairs without a necessity to exchange the substrates.

3.3.1 Prepared waveguides

The layout of the used CPWs was designed to be compatible with the microwave probes and so that they can be wire-bonded. Moreover, the CPWs are designed to provide enough space for placing of our samples within the flip-chip technique.

In order to enable the excitation of different wavevectors, CPWs with various dimensions have been prepared. The characteristic dimensions by which the CPWs are described involve: width of the signal line w_s, width of the ground lines w_g, and the gap between them g, the signal-to-signal line distance d, the length of the lines L and the Au layer thickness t. These parameters are varied and the other dimensions are kept constant. For the sake of clarity, the characteristic parameters are graphically illustrated in optical micrographs of the prepared CPWs in Fig. 3.9.

The waveguides prepared on the SiO_2/Si substrate, intended to be used in the FMR experiments, have the overall length of 8.4 mm including the contact pads. The distance between the narrow part of the CPW and the contact pads is bridged by 50 µm wide lines

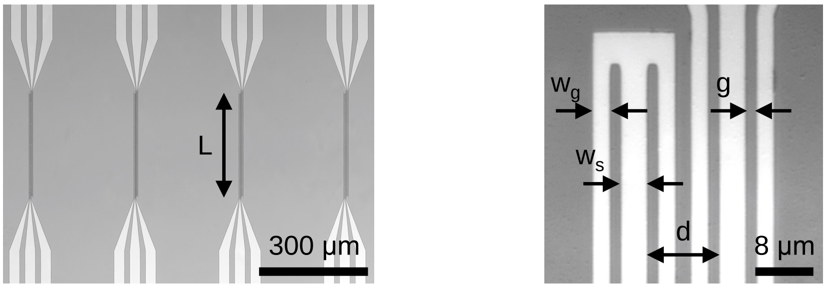

Fig. 3.9: An optical micrograph of four CPW pairs, which wary in the signal-to-signal distance and a detail of a CPW pair snapped with higher magnification. The characteristic dimensions of the waveguides are indicated together with their designation.

tapered on both ends. The width and the length of the contact pads are $(100\times300)\,\mu\text{m}^2$ and the edge-to-edge pitch between the signal and the ground pads is $50\,\mu\text{m}$.

In the case of the PSWS, the waveguides prepared on the GaAs substrate have the overall length of 3.7 mm including the contact pads. The dimensions of the contact pads are $(100\times100)\,\mu\text{m}^2$ and the edge-to-edge pitch between the signal and ground pads is again $50\,\mu\text{m}$.

The waveguide which is used for a majority of the FMR experiments is a CPW in the transmission geometry. It can be characterized by the following dimensions: $g = 5\,\mu\text{m}$, $w_\text{s} = w_\text{g} = 10\,\mu\text{m}$, $L = 1000\,\mu\text{m}$ and $t = 100\,\text{nm}$. The estimated k_CPW excited by such a CPW is approx. $0.23\,\text{rad}/\mu\text{m}$.

As different CPWs are used for the PSWS experiments, the characteristic parameters of the used series are concisely presented in Tab. 3.2. The k_CPW and k_cutoff values of each CPW are included in the table. These values are numerically calculated using FEMM software[1].

Tab. 3.2: Characteristic dimensions of the CPWs used for the excitation and the detection of propagating spin-wave modes. All the presented CPWs have the same thickness of the Au layer $t = 140\,\text{nm}$ and the length $L = 400\,\mu\text{m}$. Only the shortest signal-to-signal distance of each series of four CPW pairs, labeled as min. d, is explicitly stated. The other d values can be obtained by adding $1, 2$ or $3\,\mu\text{m}$.

label	w_s (µm)	w_g (µm)	g (µm)	min. d (µm)	k_CPW (rad/µm)	k_cutoff (rad/µm)
a	3.27	2.54	1.20	9.13	0.7031	1.342
b	2.36	1.20	0.81	5.96	1.087	1.981
c	3.66	2.75	1.86	10.68	0.5752	1.087
d	2.16	1.80	1.68	6.29	0.8309	1.534
e	3.27	2.18	1.35	9.14	0.7031	1.278
f	2.75	1.93	1.20	8.00	0.8309	1.534

3.4 Experimental setup

The experimental setup used for the all-electrical spin-wave spectroscopy investigation is illustrated by a diagram in Fig. 3.10. The main parts of the setup are as follows: the VNA instrument, a source of the bias magnetic field equipped by a Hall probe gaussmeter and a power supply, a computer used for automation of the experiment control, the source and the detector of SWs and finally the sample upon investigation.

The VNA instrument (model Rohde & Schwarz ZVA50 10 MHz−50 GHz Vector Network Analyzer) is used both as a generator of a sine-wave stimulus and as a detector of the dynamic response of the system, in accordance with the description provided in Sec. 1.4. Transmission of the hf signal towards the CPW and back to the VNA is ensured via microwave cable assembly by Huber-Suhner (model SF104). Their connection

---

[1] Finite Element Method Magnetics: www.femm.info/wiki/HomePage

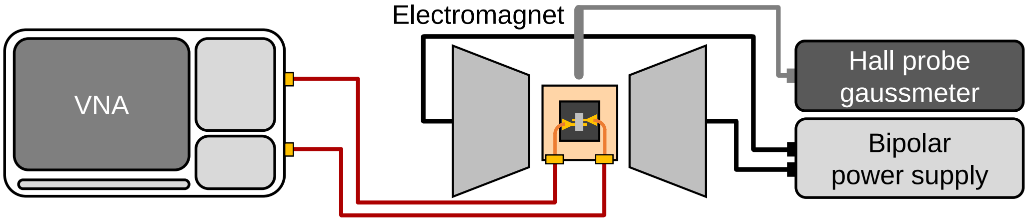

Fig. 3.10: Schematic diagram of the experimental setup for the all-electrical SW spectroscopy measurements. The sample and the CPW(s) are placed between the pole pieces of the electromagnet. The magnet is powered by bipolar power supply and the produced field is measured by digital gaussmeter. Connection of the CPWs with the ports of the VNA is established via hf cables and SMA connectors.

is established by SMA (SubMiniature version A) connectors placed at both ends of the cables.

The bias field is generated by an electromagnet powered by a bipolar power supply (model BOP 20-10M) made by Kepco. Positions of iron pole pieces of the electromagnet can be adjusted. Depending on the width of a cavity between the pole pieces, the electromagnet is able to produce the magnetic field of the intensity $\mu_0 H$ up to approx. $2\,\mathrm{T}$. The bias fields applied during an investigation of our samples, however, do not in most cases exceed $100\,\mathrm{mT}$. A digital Hall effect gaussmeter (model FW Bell 6010) with the probe placed in the vicinity of the sample is used to dynamically measure the intensity of the magnetic field between the pole pieces.

The power supply, the gaussmeter, and the VNA are connected to a computer through a USB (universal serial bus) and a GPIB (general purpose interface bus) interface. In this way, the devices can be controlled from the computer via dedicated LabVIEW software which allows for semi-automated measurements of the S-parameters in dependence on frequency and magnetic field.

Connection of the waveguides

Since our CPWs are contacted exclusively via the wire-bonding technique, an adapter which would connect the CPWs with the rest of the experimental setup has to be used. The adapter made of a double sided Cu clad board is prepared separately from the CPWs and it can be repeatedly used for different CPW series. Examples of the prepared adapters suitable for the FMR and for the PSWS studies are shown in Fig. 3.11a.

First, electrodes to direct the hf signal between the waveguide and the SMA connectors are engraved into the Cu clad board. The board is equipped with a pair of device sockets (model Right Angle SMA 50 Ω made by Rosenberger) and then the GaAs substrate with the CPWs is fixed to an engraved position on the top of the board. In order to allow eventual removal (and exchange) of the CPWs series, a glue soluble in acetone is used for the fixation. Finally, contact pads of one CPW are wire-bonded to the engraved signal lines.

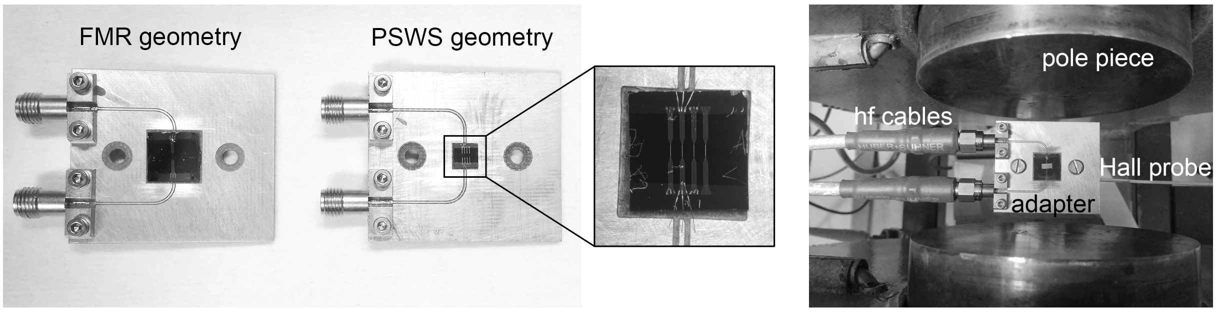

(a) Adapters with wire-bonded CPWs (b) Mounted adapter

Fig. 3.11: Photographs of the CPWs wire-bonded to the Cu board adapters. (a) Examples of the prepared adapters for each of the experimental geometries. Substrates with a single CPW in transmission geometry are used for the FMR measurements and substrates with a series of four CPWs are used for PSWS experiments. (b) A top view of the adapter mounted between the pole pieces of the electromagnet. The measured sample is placed film-side down on the CPW.

It requires a special care to properly wire-bond the CPW, as the bonds act as sources of noise during the hf measurements. Hence, the quality of the prepared bonds is to some extent related to the quality of the acquired frequency spectra.

The Cu board adapter including the CPWs, prepared according to the described procedure, can be mounted between the pole pieces of the electromagnet and connected with both the ports of the VNA. The investigated sample is put by the magnetic-film-side down on the middle part of the SiO_2-covered waveguide(s). The whole interconnection is captured in Fig. 3.11b.

4 Experimental results and discussion

In this chapter, the achieved results are presented and discussed. Quantitative analysis of static and magnetodynamic properties obtained through the broadband FMR is presented in Sec. 4.1. We present the FMR measurements of FeNi thin films grown on Cu and on Cu/H-Si substrates and compare them with thin films of standard ferromagnetic materials, which include Fe, Ni, and Permalloy. In Sec. 4.2, we present results from PSWS experiments with FeNi thin films and we study a possibility to employ the metastable FeNi thin films in magnonics. The spectroscopy is carried out as well for materials commonly used in magnonic structures, Permalloy and YIG. Then in Sec. 4.3, we compare propagating SW modes in a continuous layer of FeNi and in a micro-structured layer.

4.1 Broadband ferromagnetic resonance

All measurements discussed in the following section are performed using the setup which is described in Sec. 3.4 combined with the flip-chip technique. Therefore, we used the SOLT calibration, which is referred to in Appendix A.1, using the calibration kit provided by the VNA manufacturer.

The directly measured quantities are the S-parameters in their polar notation. Hence, we obtain magnitude (power) and phase of the S-parameters in dependence on frequency. An example of a raw frequency spectrum acquired by the VNA is provided in Fig. 4.1. The chart shows measured FMR quantities of transformed 24 nm thick film of FeNi measured in a bias magnetic field of 58 mT. The FMR peak which lies at 9 GHz, is almost entirely hidden in the signal background. Therefore, it is necessary to process the detected signal first and normalize the spectra to a reference signal[1].

A common technique of the normalization is a subtraction of the signal from a reference signal and its subsequent division by the reference. Essentially any frequency spectrum taken under different bias field can serve as the reference. However, typically the signal

---

[1] The detected power, initially provided in dBm, is converted to mW and with a known load impedance, its further conversion to corresponding voltage signal is also possible. The conversion between the power in dBm and in mW can be achieved as follows

$$P(\mathrm{dBm}) = 10\log_{10}\left(\frac{P(\mathrm{mW})}{1(\mathrm{mW})}\right) = 10\log_{10}\left(\frac{V_{\mathrm{pk}}^2(\mathrm{V})}{2R}\right). \tag{4.1}$$

Here, the V_{pk} is a peak voltage value of a sine-wave. As well as the power is recalculated, the phase can be converted from degrees to radians. Then, the recalculated values can be expressed in Cartesian form. To reveal the field-dependent signal, they are most often used in logarithmic form. Finally, the whole spectra is normalized to the reference.

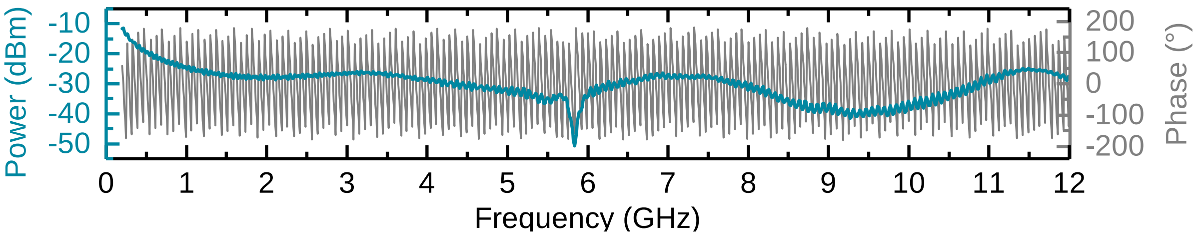

Fig. 4.1: Raw frequency sweep spectrum of S_{21} obtained from 24 nm FeNi film measured at 58 mT. The FMR peak at 9 GHz is barely visible.

obtained at the highest applied bias field, sufficient for saturation of the magnetic material or the signal obtained at zero bias field is chosen.

To avoid introduction of asymmetry into the normalized spectra, we used as the reference either the spectrum obtained at zero-field or a median of all the measured spectra through the sweep of magnetic field. We observed the best results using the latter approach because this choice of the reference reduces the signal variations with the bias field. In most cases, however, the zero-field reference provided very similar results.

After such treatment, the FMR is usually fairly distinguishable from the background even in the case of very low measured signal strengths. Examples of two processed signals illustrating the enhanced visibility of the observed peaks are shown in Fig. 4.2. We denote the modified quantities ΔS_{ii} and ΔS_{ij}. Strengths of the excitation and detection signals are represented by $|\Delta S_{ii}|$ and an amplitude of the transmitted signal is represented by $|\Delta S_{ij}|$. Further information can be assessed also from their real and imaginary parts $\mathbb{R}(\Delta S_{ij})$ and $\mathbb{I}(\Delta S_{ij})$, respectively. Moreover in the SW propagation experiments, information about the phase is carried in the transmitted signal.

All the presented SW spectra are processed with the use of the reference signal technique, to enhance the visibility of the FMR signal. Always, the $\mathbb{I}(\Delta S_{ij})$ values are plotted on a logarithmic scale. In Fig. 4.3, the measured SW spectra of metastable FeNi thin films can be seen. The FMR peak is well visible in each map. This is caused by excitation of the SW at the resonance combinations of bias field and frequency. The probed frequency range is 0.1-10 GHz and the bias field is swept from 100 mT to -100 mT. The input power is 10 dBm.

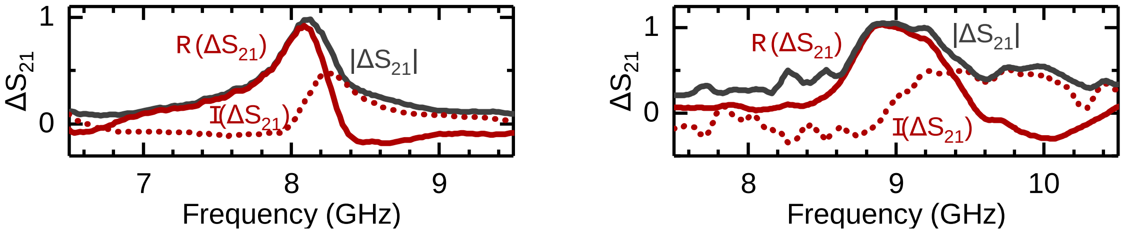

(a) 100 nm Permalloy

(b) 24 nm FeNi

Fig. 4.2: Measured and processed quantities ΔS_{21} obtained from the spectra of Permalloy and FeNi films. Both examples are measured at 50 mT in the frequency range around the FMR peak. Spectrum measured at zero bias field was taken as the reference signal.

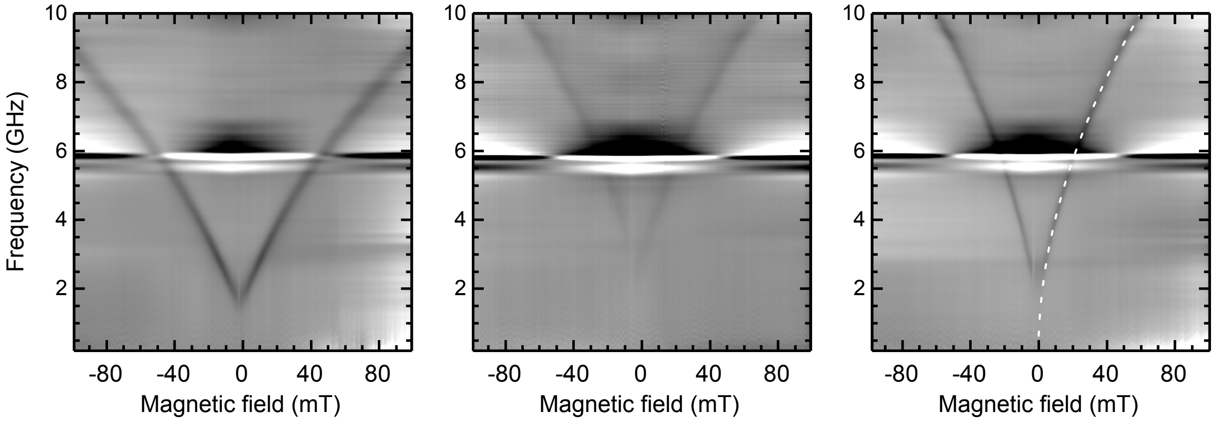

(a) 8 nm FeNi/Cu (b) 8 nm FeNi/Cu/Si-H (c) 24 nm FeNi/Cu/Si-H

Fig. 4.3: SW spectra of the three studied FeNi films. The normalized ΔS_{21} parameter is plotted in a logarithmic scale. Dashed (white) line indicates the FMR fitted by Eq. (1.23)

The apparent frequency-independent peak lying at $f = 5.9\,\text{GHz}$ (in Fig. 4.3) is not related to the ferromagnetic material of investigation. Instead, this noise is caused by a standing electromagnetic wave created in the cavity between the pole pieces of the electromagnet. The signal lines of the Cu adapter behave as a microwave antenna exciting a wave which is reflected on the poles pieces. It was found that the observed signal corresponds to the 29^{th} Harmonic of the standing wave.

4.1.1 Magnetodynamic properties measurements

The obtained SW spectra are further investigated in order to extract the magnetodynamic characteristics of the studied materials. We achieved to extract the parameters including: saturation magnetization M_S, gyromagnetic ratio γ, damping parameter α and inhomogeneous broadening ΔH_0, which are all described in Sec. 1.2.2. Different steps of data processing, which we describe in detail, are depicted in Fig. 4.4.

The most straightforward is the extraction of the M_S and the γ from the SW spectra, which can be done by fitting the FMR frequency in accordance with Eq. (1.23). As the presence of weak magnetocrystalline anisotropy is expected, we included the anisotropy constant K_1 to the model. Based on Kerr measurements we carried out earlier, no tilt of the magnetization from the film surface is expected, and therefore, the term containing $K_\perp$ is not considered. In this way, we obtained the values of M_S and γ for all the three FeNi samples. In all of them, the best fit was found for the $K_1 = 0$. The most probable explanation concerning the samples prepared on H-Si is their weak anisotropy. In the case of FeNi/Cu(100), it would be necessary to analyze several other areas transformed by FIB scanning along different directions, to extract a reliable value of K_1. Therefore, the K_1 is not listed in Tab. 4.1 among the other obtained parameters.

To extract α, there exist two possible approaches, which were discussed in the Sec. 1.2.2. The first relies on the linewidth ΔH and the latter uses the linewidth Δf according to Eq. (1.25) and (1.26), respectively. We implemented both methods into the analysis pro-

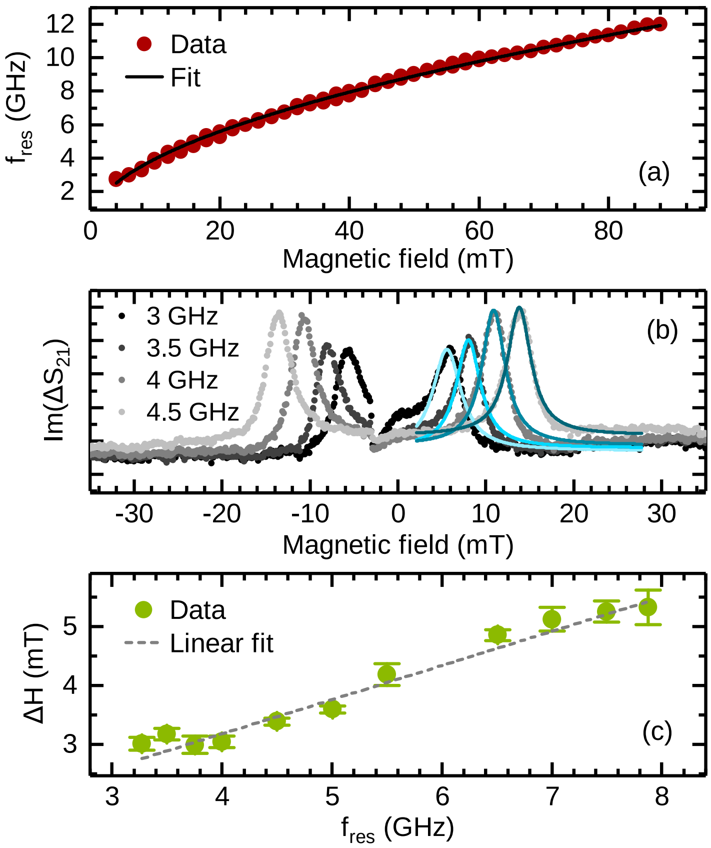

Fig. 4.4: Different steps of the data analysis process shown on a 24 nm FeNi film: The resonance frequency f_{res} is first fitted using Kittel formula (Eq. (1.23)), from which we obtained parameters M_{S}, γ and eventually K_1 (a). Next, the $\mathbb{I}(\Delta S_{21})$ parameter as a function of the bias field at constant frequency is fitted by the Lorentzian function (b). Finally, the Lorentzian shape linewidth is plotted against the f_{res}, giving a linear dependency, from which the α and ΔH_0 is assessed (c).

cess but the approach relying on Δf was found less accurate in the measured region due to the linewidth broadening at low frequencies[2]. Therefore, we present the results obtained using the linewidth ΔH. At selected frequencies, we fitted the field-sweep spectra of $\mathbb{I}(\Delta S_{21})$ by the Lorentzian function. Its full width at half maximum ΔH is a linear function of the resonance frequency f_{res} (Fig. 4.4). The slope is proportional to the α and the intercept can be interpreted as the ΔH_0.

In order to classify our samples and to compare them with different materials, we analyzed also several other ferromagnetic materials which we have available (Fe, Ni, Permalloy). Each of them was deposited by an electron beam evaporation as a continuous film on a Si substrate. We prepared samples with the film thickness of 100 nm which would be easy to measure and should display bulk-like properties and also 8 nm films to better approximate our FeNi samples. The measurement and the analysis process was the same

---

[2] The phenomena of the line-width broadening is indirectly connected to the flip-chip technique. Especially to the fact, that the transformed area of the sample is larger than is the width of the CPW conductor. The magnetic field excited off-center of the CPW has an out-of-plane component. This inhomogeneity creates magnetostatic modes, which cause the linewidth broadening at low frequencies [72].

Tab. 4.1: Summary of the parameters extracted from FMR measurements. The mean values are provided together with respective standard deviations. Reference values taken from the literature are listed together with the measured values.

sample	t (nm)	$\mu_0 M_\mathrm{S}$ (T)	$\gamma/(2\pi)$ (GHz/T)	α $\times 10^{-3}$	ΔH_0 (mT)
FeNi/Cu/H-Si	24	1.77±0.6	29.5±0.5	8.39±3.1	0.7±0.28
FeNi/Cu/H-Si	8	1.75±1.5	28.5±1.6	8.79±0.27	1.7±1.1
FeNi/Cu	8	1.17±0.9	26.0±1.0	8.84±1.1	0.4±0.4
Permalloy [64]	–	1.04	29.9	8 [36, 89, 138]	–
Permalloy/Si	100	1.03±0.05	29.8±0.6	8.0±0.4	0.3±0.18
Permalloy/Si	8	0.86±0.31	29.5±5	14.0±1.3	0.8±0.6
Fe [64]	–	2.15	28.9	–	–
Fe/Si	100	2.2±0.7	28.9±4	47±13	4±5
Fe/Si	8	1.6±0.6	28.9±5	12.4±1.0	5.3±0.4
Ni [64]	–	0.61	29.5	–	–
Ni/Si	100	0.61±0.37	26.5±7.3	20.8±6.7	24.3±2.4

as the already described characterization of FeNi. A selection of the measured maps for the reference materials can be found in Appendix B.1.

All obtained results and corresponding reference values are summarized in Tab. 4.1. The measured parameters of the thicker reference materials are in good agreement with the values which can be found in the literature. Not surprisingly, the M_S is reduced in the thinner films. This can be attributed to degradation of the magnetic material by its oxidation, which is more significant in the case of the thin films. We can assume similar behavior in the FeNi films. The assumption of oxidation can be supported by the fact that both the samples on H-Si were measured much sooner after their preparation than the sample on Cu, in which we observed a lower value of the M_S. Also from our other experiments with the metastable FeNi films, we have been able to conclude that the effective M_S decreases by approx. 20 % of the initial value within first few weeks after their removal from the UHV.

Concerning the SW attenuation properties, metastable FeNi exhibits relatively low effective damping. The extracted values of $\alpha \approx 0.0087$ are consistent over the three FeNi samples and they are comparable with the literature value of Permalloy (0.008). On the contrary, the α is relatively high in the Fe and Ni samples. This can be expected in imperfect films prepared by the evaporation.

The observed finite zero-frequency field linewidth ΔH_0 is very small in the FeNi when compared with Fe and Ni. This inhomogeneous broadening is connected with structural imperfections of the investigated material. Therefore, this behavior also is expected, as the quality of the epitaxially grown FeNi films is certainly better than of the films prepared by the evaporation. The less expected are the low values in case of Permalloy. On top of that, we can observe the lowest value of ΔH_0 between the FeNi samples in the film grown on Cu and the highest value in the thinner film on H-Si, which is in accord with our observations of their morphology, discussed in Sec. 3.2.2.

4.2 Propagating spin wave spectroscopy in plain films

The spin wave propagation study was carried out by PSWS experiments using the same setup as described in Sec. 3.4. In contrast with the FMR studies, we used a pair of CPW prepared on GaAs substrate for each measurement of FeNi samples. We have studied SW propagation in FeNi exclusively in the geometry of magnetostatic surface spin waves. However, in YIG, we were able to observe propagating modes in two different geometries: magnetostatic surface spin waves and magnetostatic backward volume waves.

4.2.1 Propagation in YIG film

The study of YIG on a gallium gadolinium garnet (GGG) substrate was performed predominantly to verify the capabilities of our measurement setup. This material was chosen as it has been studied by PSWS by other groups and the signal of propagating SW is easy to acquire.

A sample used for the study is a 6 µm thick YIG film epitaxially grown on GGG(111). Lateral dimensions of the sample approx. $(3{\times}24)\,\mathrm{mm}^2$ allowed us to study the SWs propagating between 2 mm and 20 mm distant antennas. These propagating modes were excited and detected solely by antennas engraved into the Cu board. The signal line width was chosen to be approx. 500 µm. This way, the highest excited wavevector (approx. 60 rad/cm) is still in the non-saturated part of the dispersion curve even though the M_S of YIG is very small.

The measurement and the subsequent signal processing was performed using the same procedure as in the previous experiments. The frequency was swept in a range of 0.1-4 GHz and the bias field was swept between ±100 mT. The best signal-to-noise ratio was obtained for the input power of -10 dBm. The measured SW spectra in both geometries were verified by numerical calculations. A side by side comparison of the measured and the modeled SW spectra is shown in Fig. 4.5.

We acquired the modeled SW spectra from numerical calculation of the density of states in dependency on the bias magnetic field. The material parameters used in the calculation were taken from the literature: $\gamma/(2\pi) = 28\,\mathrm{GHz/T}$ and $M_\mathrm{S} = 0.14\,\mathrm{MA/m}$ [49, 97]. The calculation of dispersion relations for MSSW and MSBVW modes was performed using MATLAB software. The obtained normalized density of states was plotted for the same bias field and frequency range as in the experiment. It can be seen that the measured and modeled data are in a good agreement.

In a low-field region of the measured spectra (Fig. 4.5), the SW signal apparently disappears. This is caused by a demagnetization of the YIG film, which is characterized by out-of-plane magnetization direction in absence of a bias field. With increase of the bias field intensity, the signal is soon restored after exceeding the anisotropy field. The SW spectra of all four signals obtained from the S-parameters measurement in MSSW geometry are further presented in Appendix B.2.

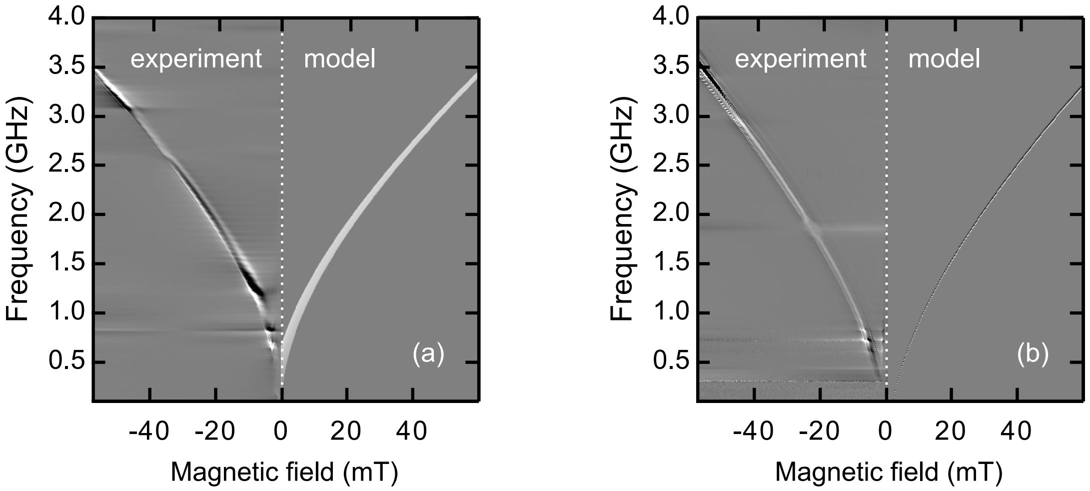

Fig. 4.5: Comparison of the measured and calculated SW spectra of (a) MSSW and (b) MSBVW propagating in YIG/GGG(111). The thickness of the YIG film is 6 µm and the SW are excited by 500 µm wide Cu antennas. The model is calculated using the dispersion relations Eq. (1.32) and (1.33) with wavevectors in the range from $k = 0$ up to $k_{\text{cutoff}} = 63\,\text{rad/cm}$.

4.2.2 Propagation in metastable thin films

One of the main goals of the SW propagation studies was to describe the investigated material from the perspective of magnonics. So far, we were successful in detection of propagating modes in the 24 nm thick FeNi film and extraction of the SW propagation characteristics.

The observed propagating modes in the transformed continuous layer of 24 nm FeNi are presented in Fig. 4.6. As a SW source and detector, we used a CPW series b, the parameters of which are summarized in Tab. 3.2. This design combines a relatively short separation and moderately low static impedance, which was measured as 115 Ω between the signal and the ground electrodes. We observe signal at significantly lower frequencies than it is predicted from the analytical model of the MSSW mode, Eq. (1.32), for $k = k_{\text{CPW}} = 1.087\,\text{rad/µm}$. In the figure, the modeled MSSW mode is indicated by slid (blue) line. Even though, we expect that the measured spectra belong to the propagating mode, as we observe a frequency increase compared to the FMR, which is indicated by dashed (blue) line corresponding with the curve in Fig. 4.3c.

A range of the measured bias fields was narrowed to ±50 mT, after initial PSWS experiments which revealed that at higher frequencies (and thus fields) the signal is almost hidden by the noise and it is unsuitable for the analysis. The signal amplitudes overall are much lower in the PSWS compared with the FMR studies. The high level of background signal is connected also with the use of the flip-chip technique. Despite the limitation of the technique, we were able to extract the SW characteristics from the measured spectra.

To evaluate the SW characteristics, the amplitude of the transmitted signal is first normalized to the excitation strength. However, in order to do so, another aspect needs to be taken into account. In general, the sample upon investigation is not placed precisely in the geometrical center of the CPWs, which leads to an inequality of the excitation and

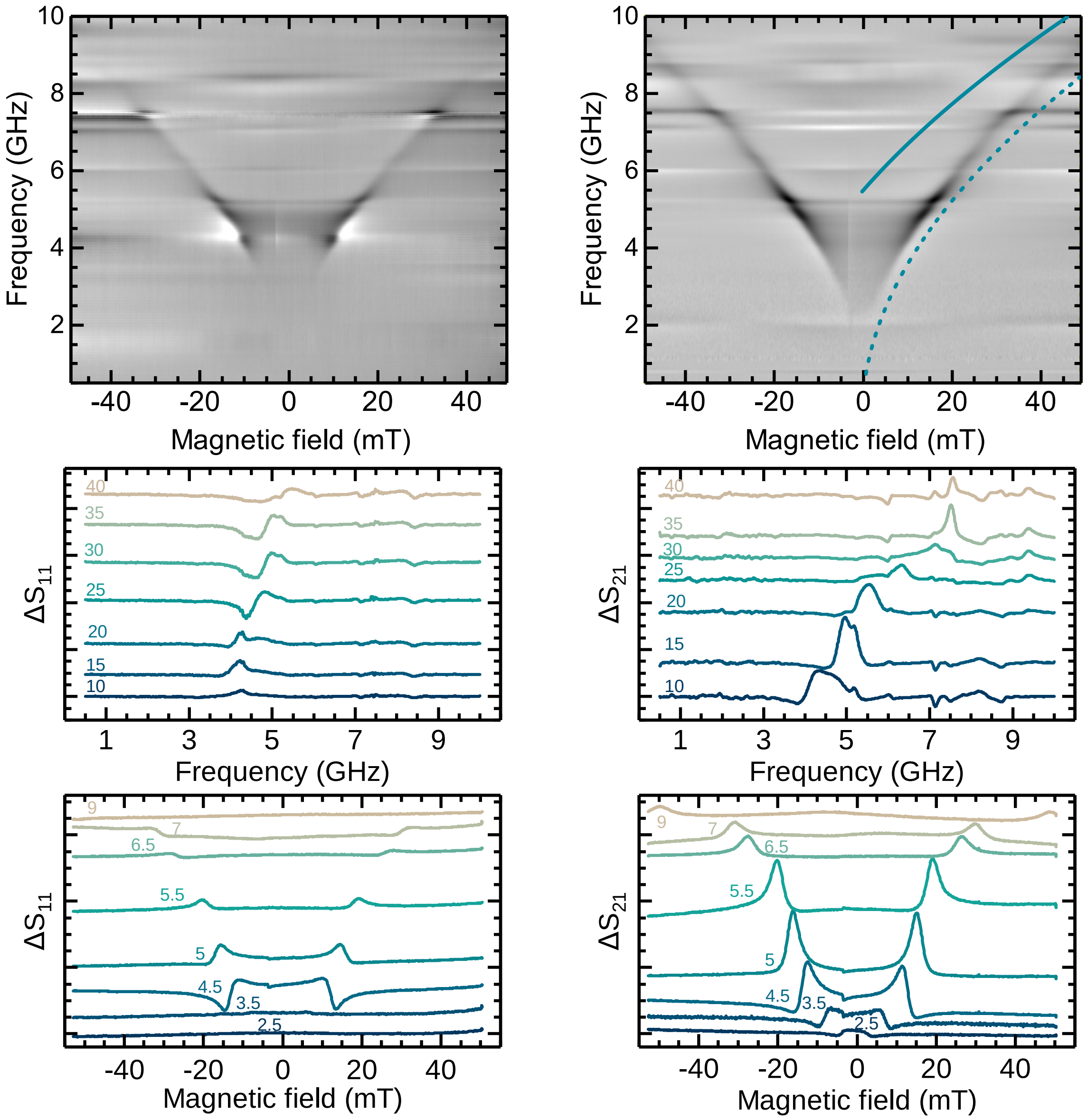

(a) $\mathbb{I}(\Delta S_{11})$

(b) $\mathbb{I}(\Delta S_{21})$

Fig. 4.6: Imaginary parts of the normalized amplitudes of the reflected signal at port 1 (a) and the transmitted signal between two CPWs with $d = 5.96\,\mu\text{m}$ (b). Cross sections of the SW spectra at selected frequencies and bias fields (labeled in the graphs) are presented below. They show the excited SW (corresponding to S_{11} parameter) and the SW incoming (corresponding to S_{21}) to the other CPW. The spectra are obtained for 24 nm thick film of FeNi prepared on H-Si. Analytical model of the MSSW excited by $k_{\text{CPW}} = 1.087\,\text{rad}/\mu\text{m}$, based on the measured parameters of the sample (given in Tab. 4.1) is indicated in the SW spectra by blue line. For clarity, as well the model of FMR is indicated in the SW spectra by the dashed (blue) line.

detection strengths. Thus, $|S_{11}| \neq |S_{22}|$. Such non-reciprocity can be even though mathematically corrected. Instead of using only the $\Delta S_{21}/\Delta S_{11}$ (or $\Delta S_{12}/\Delta S_{22}$) parameter, the geometrical mean of both reflected signals $\sqrt{\Delta S_{11}\Delta S_{22}}$ is employed as a normalization factor.

Then, the normalized parameters can be used to evaluate the SW characteristics such us the group velocity, the decay length δ and the magnetization relaxation rate Γ. These quantities are connected through the formula $\delta = v_\mathrm{g}/\Gamma$.

To obtain the SW characteristics, we followed an experimental procedure as reported by Gladii et al. [138], who studied single crystal iron films grown on MgO(001). The amplitude of $|\Delta S_{21}|$ as well as the real $\mathbb{R}(\Delta S_{21})$ or the imaginary part $\mathbb{I}(\Delta S_{21})$ is needed. The amplitude $|\Delta S_{21}|$ of the signal measured in PSWS experiment is normalized to the amplitudes $|\Delta S_{11}|$ and $|\Delta S_{22}|$ representing the excitation and detection strengths, yielding a normalized amplitude A_{21}. This quantity is expected to decay with the distance between the CPWs as

$$A_{21} = \frac{|\Delta S_{21}|}{\sqrt{|\Delta S_{11}||\Delta S_{22}|}} = \mathrm{e}^{-(d+d_0)/\delta}. \tag{4.2}$$

Here, d_0 stands for an offset caused by the non-zero width of the CPW signal lines. Since the decay is exponential, -ln(A_{21}) is a linear function of the signal-to-signal distance d. A slope of the dependency provides an inverse of δ. Therefore, the PSWS has to be carried out for several pairs of CPWs with various d (Fig. 4.7a).

Furthermore, we use the fact that the imaginary (and the real) part of the transmitted signal contains information about the phase of the propagating SW. This leads to the formation of an oscillation of the signal imaginary component, within the peak formed by the signal magnitude. The period of this oscillation is connected with the v_g through the propagation time $\tau = (d + d_0)/v_\mathrm{g}$. The oscillation period which indicates the change of phase about 2π is the inverse of the τ. Hence, by plotting the τ against the d, we can obtain the group velocity as an inverse slope of the linear dependency (Fig. 4.7b).

The relaxation rate of the propagating SW can be obtained from Eq. (4.2) by substituting for δ and subsequently for τ. Then, the Γ simply represents the slope of -ln(A_{21}) as a function of d (Fig. 4.7c).

We measured the S-parameters using a series of four CPWs, to have enough points to allow us to fit the data. From the measured SW transmission map (Fig. 4.6b), we chose the frequency spectra at the bias field of 20 mT. Around this field, the SW signal was

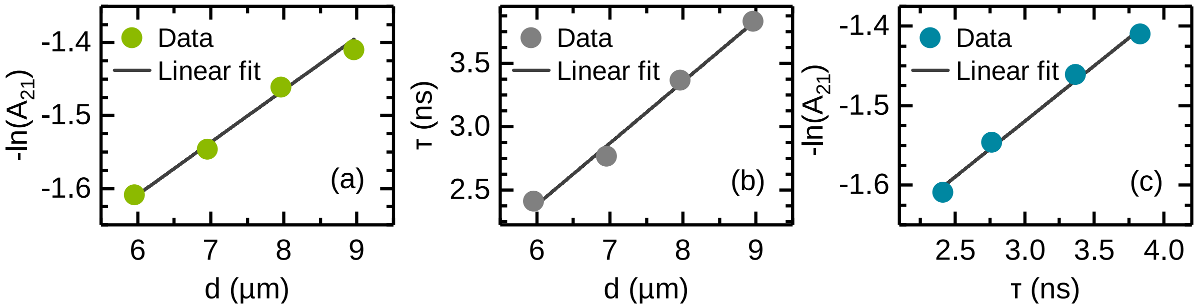

Fig. 4.7: SW characteristics extracted from PSWS measurements of 24 nm thick transformed continuous layer of FeNi. A dependence (a) of the logarithm of the normalized signal amplitude A_{21} on the signal-to-signal distance d providing δ^{-1}, a dependence (b) of the propagation time τ on the d providing a v_g^{-1} and a dependence (c) of the logarithm of A_{21} on the τ providing the value of Γ.

Tab. 4.2: Summary of the propagating SW characteristics extracted from the PSWS measurements. The mean values are provided together with respective standard deviations. The bias field, at which the analysis was carried out is indicated as H.

sample	t (nm)	H (mT)	δ (µm)	v_g (km/s)	$\Gamma \times 10^8$ (rad/s)
FeNi	24	20	13.9±0.6	2.05±0.15	1.47±0.09
Permalloy	100	38	3.3±0.6	3.2±0.4	11.3±1.6

the least difficult to distinguish from the background noise. We processed the frequency spectra for each measured d as described above and acquired the parameters which are listed in Tab. 4.2.

In order to support our results, we repeated the same measurement and analysis for material commonly used for SW propagation – Permalloy. Propagating modes were excited in 100 nm thick Permalloy film using a CPW series d. These CPWs have very similar dimensions and thus excite similar wavevectors as the previously employed CPWs (type b). To assure the conditions as similar as possible with the initial experiment using FeNi, we investigated the frequency spectra having the peak at the same resonance frequency as FeNi does. An intensity of the corresponding bias field is 38 mT. Results of the analysis are presented in Tab. 4.2 and selected steps of the analysis are presented in Appendix B.3.

The table provides a comparison of the calculated characteristics together with the sample properties and the field H at which the analysis was performed. The value of decay length extracted for Permalloy is consistent with our expectations 3 µm [139]. On the contrary, we found unusually long decay length of SWs propagating in FeNi. The results obtained from SW propagation in epitaxially grown Fe, as reported by Gladii et al. [138], are significantly different than ours. The study presents the decay length in a range of 5-7 µm, which is approximately half of our value. In the study, the SW characteristics are calculated for the bias fields within a range of 20-180 mT. The value of $\delta = 6.8$ µm extracted at 58 mT (corresponding with the resonant frequency of 18.9 GHz) is stated explicitly in the study. On the contrary, our result is measured at 20 mT and the resonant frequency is 5.7 GHz. Therefore, the values cannot be correctly compared. Nevertheless these findings are not necessarily in a dispute, since a decreasing character of δ with the resonant frequency is expected. Moreover, our result approaches the theoretical values of δ, which are quite higher at low-frequency region than those measured in Ref. [138].

Using our current experimental setup, we were able to analyze the propagating SW only in a range of low frequencies. However, it is of high interest to repeat the experiment for SWs excited by higher frequencies, in order to compare the values precisely. The result we have obtained so far is still very promising, even though a further investigation should to be carried out in order to confirm this first observation.

In addition to the propagating SW modes in the 24 nm thick FeNi film, we were also able to detect SWs propagating across a distance of approx. 6 µm in the FeNi film with the thickness of 8 nm. The SWs were excited and detected by a pair of CPWs from a series *b*. The obtained SW spectra is presented in Appendix B.4. Despite the fact that strength of the detected signal is not sufficient to perform quantitative analysis of the SW characteristics, these data open up new possibilities for investigation. As the measured SW spectra prove that the combination of the detection limits given by our experimental setup and attenuation properties of FeNi enables to carry out further PSWS experiments with the 8 nm films.

4.3 Spin waves in modulated magnetic media

An experimental study of SW propagation in magnonic crystals was initiated based on assumptions derived from results obtained through micromagnetic modeling.

Theoretical model

The theoretical studies carried out by O. Wojewoda [140], investigate SW propagation in magnonic crystals comprising ferromagnetic thin films that display the same magnetic properties as those experimentally observed in the FeNi thin films.

The modeled dispersion relations in MSSW geometry at 50 mT for three MCs and corresponding SW spectra are shown in Fig. 4.8. The MCs comprise 10 nm thick ferro-

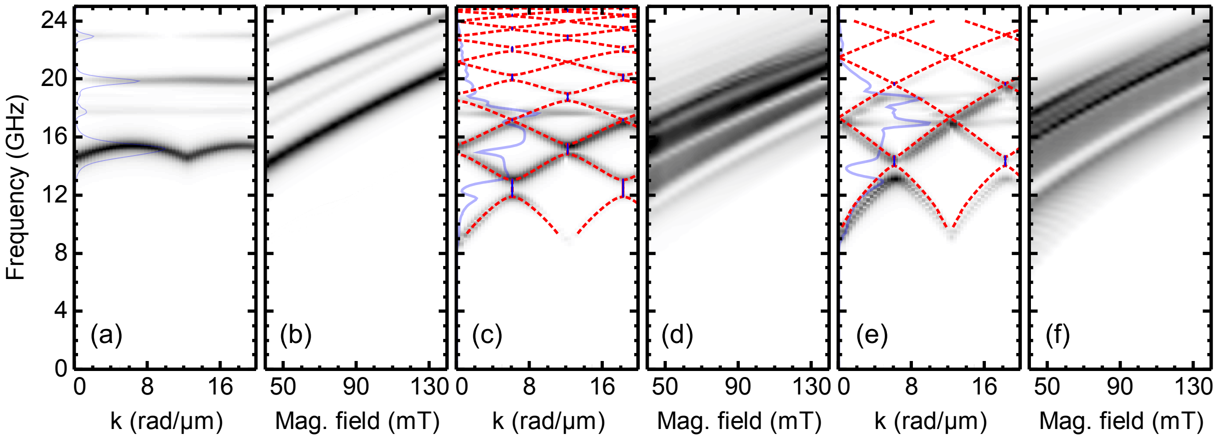

Fig. 4.8: Dispersion relations (a), (c) and (e) and SW spectra (b), (d) and (f) of one-dimensional MCs created by spatial modulation of various magnetic parameters in alternating strips. The strips are characterized by the width of 256 nm, the thickness of 10 nm and nominal value of saturation magnetization $\mu_0 M_S = 2.14\,\mathrm{T}$. Damping parameter is $\alpha = 0.008$ and exchange stiffness $A = 1.3\,\mathrm{pJ/m}$. (a)-(b) A magnonic crystal created by reduction of M_S about 100 % in every second strip, which results in spatial alternations of magnetization between 2.14 T and 0 T. (c)-(d) Similar MC with reduction of M_S by 20 % resulting in alternations of 2.14 T and 1.7 T. (e)-(f) A crystal created by variation of direction of the easy axis in an anisotropic material with $K_u = 14\,\mathrm{kJ/m^3}$. The orientation of the easy axis is alternated between 0° and 90° with respect to the strips. All dispersion relations are calculated at the bias magnetic field of 50 mT. Blue profiles indicate the modeled density of states. Dashed (red) lines indicate analytically calculated dispersion relations obtained on the basis of the Bloch theorem and the transfer-matrix method. Band gaps are labeled by vertical (blue) lines. All spectra are plotted in logarithmic scale. Modified from [140].

magnetic film, in which either saturation magnetization or magnetic anisotropy is alternated in 256 nm wide strips. The created band gaps, which can be seen in the frequency spectra, are apparently reflected into the modeled SW spectra. Therefore, multiple peaks are visible in the SW spectra, in the contrary with the non-modulated material.

For the sake of clarity, we provide a brief description of the used model and processing technique:

The excitation magnetic field provided by a CPW with geometrical parameters of $w_\mathrm{s} = w_\mathrm{g} = g = 100\,\mathrm{nm}$ is modeled in FEMM. The excitation spectrum and magnetic field induced by the CPW is used as an input to micromagnetic solver mumax^3 [141], which models the SW propagation in the MC. The calculated volume of $(16\times0.2\times0.01)\,\mu\mathrm{m}^3$ is divided into rectangular prisms of size $(4\times4\times5)\,\mathrm{nm}^2$ and periodic boundary conditions with sufficient repetitions are used. The calculation time is 10 ns and the time step $\leq 1\,\mathrm{ps}$. The two-dimensional maps of M_x are captured with time-step of 6 ps and they are exported to MATLAB for further processing. Then, the data are converted by a fast Fourier transform (FFT) into the frequency domain. From the FFT of the M_x, dispersion relations of the propagating SWs are calculated. The dispersion relations are summed over k, providing the density of states in dependence on frequency. An effect of the CPW acting as the detector is included. Finally, by repeating the whole calculation of the density of states for different bias magnetic field strengths, the resultant SW spectra in dependence on frequency and bias field are obtained.

Experimental results

The experimental studies of PSWS in patterned films are somewhat complicated when relying on the flip-chip technique alone. The prepared microstructures need to cover a large area of the sample surface, as the perfect alignment of the conductors on top of the structures is not possible. Therefore, we performed the experiments on $(600\times500)\,\mu\mathrm{m}^2$ areas patterned by the FIB.

Whereas our experiments are the very first studies of SW propagation in FeNi, we decided to begin with the least complicated type of MCs: a one-dimensional modulation of the saturation magnetization, see Fig. 4.8a-4.8d. Using the knowledge of the precise proportion between the ion dose used for the film transformation and the resultant saturation magnetization in case of the 24 nm thick FeNi film on H-Si (Fig. 3.3), we were able to modulate its M_S in a controlled way.

The first prepared sample comprises 900 nm wide strips with the highest possible M_S, alternating with 900 nm wide strips from which the FeNi layer was completely etched away. In the resulting structure, the M_S is confined in the ferromagnetic strips separated by the etched grooves (Fig. 4.9a). The width of the strips was designed based on the knowledge of dispersion relations of different MCs obtained from micromagnetic modeling as well as on the FIB patterning possibilities.

The second sample was prepared without a topographical modulation of the FeNi film. We irradiated the chosen area by two different ion doses (Fig. 4.9b) both of them lower than would be necessary to sputter the FeNi away. The resultant structure consists of 1000 nm wide strips with the highest possible saturation magnetization (which is approx. 1.77 T) and 800 nm wide strips with the M_S being a half of the maximum value (approx. 0.88 T).

Both of the samples were checked via SEM and Kerr microscopy in order to confirm the structure and the magnetic properties of the transformed patterns. The micrographs of the structures are shown in Fig. 4.9. The coercive field of both samples is approx. 15 mT, when the strips are aligned parallel with the external magnetic field.

For the PSWS measurements, we employed the same experimental technique as in the case of continuous magnetic films, with the only exception of the measurement frequency range. We measured the PSWS in the range of 0.5-20 GHz, in order to capture also the band gaps and the modes arising from the confinement, which are expected to lie within this frequency range.

The measurements were carried out for both transformed structures, using the CPWs from series *b*, *c*, and *d*. One of the measured SW spectra is presented in Fig. 4.10. It corresponds to SW propagation through the ferromagnetic strips which are separated by the etched grooves. The employed CPWs are separated by the distance $d = 5.96$µm.

For comparison purposes, the modeled SW spectra of MCs based on the experimentally prepared structures are also incorporated into the figure. The data shown in the two-dimensional plots of the modeled MCs correspond with the normalized density of states in dependence on the microwave frequency and on the bias magnetic field strength.

As can be seen from the measured spectra, we were not successful so far in a detection of different modes than those, which we have already measured in the continuous layer. The main difference that we were able to observe is a significant decrease of the transmitted

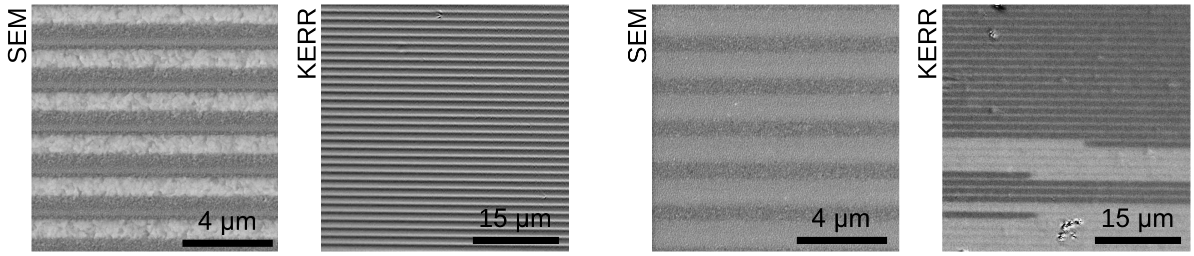

(a) (b)

Fig. 4.9: SEM and Kerr micrographs of one-dimensional magnonic crystals prepared from metastable FeNi films with the thickness of 24 nm. (a) FIB-etched grooves of width 900 nm alternating with transformed FeNi areas and (b) alternating transformed and non-irradiated FeNi stripes with the width of 1000 nm and 800 nm, respectively. To enhance a magnetic contrast of the Kerr micrographs, a corresponding image taken at full magnetic saturation is subtracted fromthe image taken at 0 mT. Therefore, the magnetic signal is made more visible on the expense of the topography.

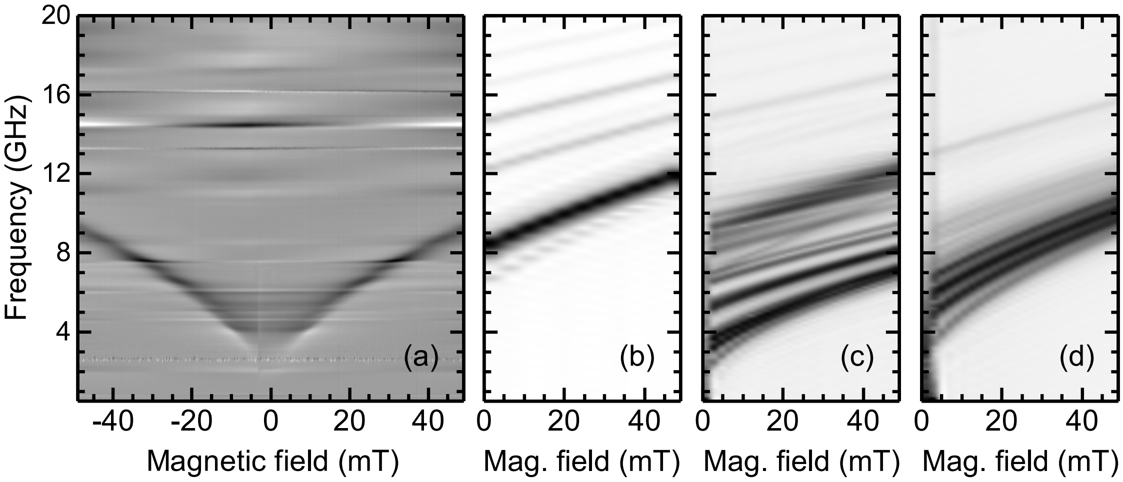

Fig. 4.10: SW spectra of the microstructured 24 nm thick FeNi film and modeled spectra one-dimensional MCs of the same thickness with alternating saturation magnetization. Experimentally determined material parameters are used in the modeled systems. (a) Measured SW propagating in 900 nm wide fully-transformed strips ($\mu_0 M_S \approx 1.77\,\mathrm{T}$) alternating with FIB-etched grooves of the same width. The SW excitation and detection is ensured by CPWs from a series b distant by $d = 5.96\,\mu\mathrm{m}$. (b) Modeled one-dimensional magnonic crystal with 900 nm alternating magnetic strips ($\mu_0 M_S = 1.76\,\mathrm{T}$) and non-magnetic strips. (c) Similar MC with alternating strips of two different saturation magnetization values $\mu_0 M_S = 1.76\,\mathrm{T}$ and $0.88\,\mathrm{T}$ (corresponding with M_S modulation by 50 %). (d) Modeled spectra of continuous thin film with $\mu_0 M_S = 1.76\,\mathrm{T}$. The calculated spectra (b)-(d) were obtained on the basis of numerical model prepared by O. Wojewoda. The model employs FEMM and MATLAB softwares for SW excitation and detection and solves the SW propagation using micromagnetic solver mumax^3.

signal when compared with SW propagation in the continuous layer. The decrease of the signal amplitude can be expected in this corrugated layer.

The reason why the other modes and the band gaps could not be measured in the patterned samples remains an open question. The most probable explanation seems to be our experimental setup relying on the flip-chip technique. We plan to implement a microwave probe station, which would allow us to lithographically prepare the CPWs directly on top of the patterned FeNi film.

Conclusion

In this thesis, we have been dealing with preparation and study of materials for magnonic applications based on metastable FeNi thin films. We investigated two systems FeNi/Cu(100) and FeNi/Cu(100)/H-Si(100) and successfully measured the magnetization dynamics in continuous and modulated layers prepared by FIB direct writing.

We have prepared several metastable FeNi thin films epitaxially grown on Cu(100) single crystal substrates. These films were initially used for magneto-structural analysis including testing of transformation ion dose efficiency, magnetocrystalline anisotropy studies, testing of various FIB patterning strategies and *in-situ* studies of topography and morphology of both unirradiated and transformed films. A sample comprising 8 nm thick FeNi film was then used for all-electrical characterization of spin wave dynamics.

We carried out multiple experiments in order to prepare hydrogenated Si(100) substrate of the best chemical purity and structural quality of the surface. Despite the efforts, we were not successful in preparation of monocrystalline Cu(100) buffer layer on the top. As was revealed by experiments performed later at TU Wien, the most probable reason for this behavior was missing Ca during the deposition of Cu. It was observed that Ca contamination in a crucible of the evaporator can have a significant influence on the growth of the first atomic layers of the Cu(100), affecting especially the initiation of the (100) structure growth. Another possibility is insufficiently low pressure in the deposition chamber during the growth. In any case, it is of high interest to proceed with the study and accomplish the growth of Cu(100) single crystal on H-Si in our laboratory. Meanwhile, the samples prepared in at TUW were used for the study of spin wave propagation.

Ferromagnetic properties were locally induced in the metastable thin films by a FIB irradiation. We achieved the best results upon single-scan irradiation by the dose of approx. 6×10^{15} ions/cm^2 in case of 8 nm thick FeNi film on Cu, and approx. 2×10^{15} ions/cm^2 and 6×10^{15} ions/cm^2 for 8 nm and 24 nm thick films on H-Si, respectively. Moreover, we found a direct relation between the crystallography and the transformation efficiency, while studying the films grown on a Cu(100) substrate. When scanned by the FIB along the low-index crystallographic directions $\langle 011 \rangle$, we could observe the full transformation upon irradiation by approx. 25% lower ion dose when compared with the scanning along one of $\langle 010 \rangle$ directions. We did not yet verify whether the same behavior concerns the films grown on H-Si, nevertheless, it may become useful in future if these films shall be utilized as magnonic elements. It can be, however, expected that the direction dependency of the transformation efficiency would be weaker in films prepared on H-Si due to the morphology of the Cu buffer layer. We observed that the irradiated surface of FeNi film grown on H-Si is approx. 5.7× more rough than the surface of the same film grown on the Cu substrate. The well-characterized samples were then employed as spin wave propagation media.

Spin waves with various wavevectors were excited and studied in three different samples with use of the VNA. The excitation was ensured via microscale CPWs with various geometrical parameters, separately prepared on GaAs and SiO_2/Si substrates. Contact pads of the waveguides were wire-bonded to the experimental setup, since the probe station for microwave probing has not been available during the project. Due to poor adhesion of the Cu buffer layer on top of the Si substrate, it is not possible to wire-bond the waveguides without damaging the underlying film. Hence, the waveguides could not be lithographically prepared on top of the FeNi films, but we had to rely solely on the flip-chip technique. The situation would be different if the probe station could have been used to avoid the wire-bonding.

In the initial experiments, we studied large transformed areas of the FeNi films by the broadband ferromagnetic resonance to obtain their magnetodynamic characteristics. Using Kittel formula which relates the resonant frequency to the external magnetic field, we extracted saturation magnetization, damping parameter, gyromagnetic ratio and inhomogeneous broadening of the resonant peak. In order to verify our results and classify the material of investigation, we performed the same experiment with several other samples including films of Fe, Ni and Permalloy. The observed value of M_S of the FeNi is approx. 1.76 T, which corresponds well with the value 1.8 T that can be obtained by interpolation of the saturation magnetizations of pure Fe and Ni. Almost the same observed effective damping (0.0087) as in Permalloy (0.008) is the confirmation justifying FeNi as a potential candidate for application in magnonics.

The measurements of non-zero k modes were carried out by propagating spin-wave spectroscopy. We excited modes propagating in Damon-Eshbach geometry and detected them inductively, by CPWs separated by the distance up to 11 µm (measured by the signal-to-signal distance). Even though we did not try to detect the propagating SWs with use of more distant CPWs, we can assume that the SW could be detected ever farther. This assumption is based on the experimentally determined SW decay length. Measured at the bias field 20 mT (and resonant frequency approx. 5.7 GHz), we obtained the decay length of 13.9 µm for a SW propagating with the group velocity approx. 2.1 km/s. For comparison, the values 3.3 µm and 3.2 km/s were observed at the same resonant frequency in Permalloy.

Encouraged by these observations, we believe that the thin metastable FeNi films hold a true potential for magnonic application as spin wave propagation media and we shall continue with their employment in further innovative investigations.

References

[1] Kruglyak, V. V., Demokritov, S. O. and Grundler, D. Magnonics. *Journal of Physics D: Applied Physics*, 43(26):264001, 2010. doi: 10.1088/0022-3727/43/26/264001.

[2] Chumak, A. V., Serga, A. A. and Hillebrands, B. Magnonic crystals for data processing. *Journal of Physics D: Applied Physics*, 50:244001, 2017. doi: 10.1088/1361-6463/aa6a65.

[3] Gloss, J., Shah Zaman, S., Jonner, J. et al. Ion-beam-induced magnetic and structural phase transformation of Ni-stabilized face-centered-cubic Fe films on Cu (100). *Applied Physics Letters*, 103(26):262405, 2013. doi: 10.1063/1.4856775.

[4] National Instruments. Introduction to Network Analyzer Measurements: Fundamentals and Background, 2018. URL `http://download.ni.com/evaluation/rf/Introduction_to_Network_Analyzer_Measurements.pdf`. Accessed: 2018-04-25.

[5] Chumak, A. V., Vasyuchka, V. I., Serga, A. A. et al. Magnon spintronics. *Nature Physics*, 11:453–461, 2015. doi: 10.1038/nphys3347.

[6] Akhiezer, A. I., Bar'yakhtar, V. G. and Peletminskii, S. V. *Spin waves*. New York: North-Holland Series in Low Temperature Physics, 1968. doi: 10.1126/science.163.3870.923-a.

[7] Holstein, T. and Primakoff, H. Field dependence of the intrinsic domain magnetization of a ferromagnet. *Physical Review*, 58(12):1098, 1940. doi: 10.1103/PhysRev.58.1098.

[8] Dyson, F. J. General Theory of Spin-Wave Interactions. *Physical Review*, 102: 1217–1230, 1956. doi: 10.1103/PhysRev.102.1217.

[9] Bloch, F. Zur Theorie des Ferromagnetismus. *Zeitschrift für Physik*, 61:206–219, 1930. doi: 10.1007/BF01339661.

[10] Griffiths, J. H. E. Anomalous High-frequency Resistance of Ferromagnetic Metals. *Nature*, 158:670–671, 1946. doi: 10.1038/158670a0.

[11] Fleury, P. A., Porto, S. P. S., Cheesman, L. E. et al. Light Scattering by Spin Waves in FeF_2. *Physical Review Letters*, 17:84–87, 1966. doi: 10.1103/PhysRevLett.17.84.

[12] Gorobets, Y. I. and Reshetnyak, S. A. Reflection and refraction of spin waves in uniaxial magnets in the geometrical-optics approximation. *Technical Physics*, 43 (2):188–191, 1998. doi: 10.1134/1.1258965.

[13] Demokritov, S. O., Serga, A. A., Andre, A. et al. Tunneling of dipolar spin waves through a region of inhomogeneous magnetic field. *Physical Review Letters*, 93(4): 047201, 2004. doi: 10.1103/PhysRevLett.93.047201.

[14] Lan, J., Yu, W. and Xiao, J. Antiferromagnetic domain wall as spin wave polarizer and retarder. *Nature Communications*, 8(1):178, 2017. doi: 10.1038/s41467-017-00265-5.

[15] Bauer, M., Mathieu, C., Demokritov, S. O. et al. Direct observation of two-dimensional self-focusing of spin waves in magnetic films. *Physical Review B*, 56 (14):R8483, 1997. doi: 10.1103/PhysRevB.56.R8483.

[16] Choi, S., Lee, K.-S. and Kim, S.-K. Spin-wave interference. *Applied Physics Letters*, 89(6):062501, 2006. doi: 10.1063/1.2259813.

[17] Khitun, A., Bao, M. and Wang, K. L. Magnonic logic circuits. *Journal of Physics D: Applied Physics*, 43(26):264005, 2010. doi: 10.1088/0022-3727/43/26/264005.

[18] Slonczewski, J. C. Current-driven excitation of magnetic multilayers. *Journal of Magnetism and Magnetic Materials*, 159(1-2):L1–L7, 1996. doi: 10.1016/0304-8853(96)00062-5.

[19] Neusser, S., Duerr, G., Bauer, H. et al. Anisotropic propagation and damping of spin waves in a nanopatterned antidot lattice. *Physical Review Letters*, 105(6): 067208, 2010. doi: 10.1103/PhysRevLett.105.067208.

[20] Yu, H., Huber, R., Schwarze, T. et al. High propagating velocity of spin waves and temperature dependent damping in a CoFeB thin film. *Applied Physics Letters*, 100 (26):262412, 2012. doi: 10.1063/1.4731273.

[21] Schultheiss, H., Pearson, J. E., Bader, S. D. et al. Thermoelectric detection of spin waves. *Physical Review Letters*, 109(23):1–5, 2012. doi: 10.1103/PhysRevLett.109.237204.

[22] Bauer, H. G., Chauleau, J.-Y., Woltersdorf, G. et al. Coupling of spinwave modes in wire structures. *Applied Physics Letters*, 104(10):102404, 2014. doi: 10.1063/1.4868250.

[23] Demidov, V. E. and Demokritov, S. O. Magnonic waveguides studied by microfocus Brillouin light scattering. *IEEE Transactions on Magnetics*, 51(4):1–15, 2015. doi: 10.1109/TMAG.2014.2388196.

[24] Lee, K.-j., Deac, A., Redon, O. et al. Excitations of incoherent spin-waves due to spin-transfer torque. *Nature Materials*, 3:877–881, 2004. doi: 10.1038/nmat1237.

[25] Choi, S., Lee, K.-s., Guslienko, K. Y. et al. Strong Radiation of Spin Waves by Core Reversal of a Magnetic Vortex and Their Wave Behaviors in Magnetic Nanowire Waveguides. *Physical Review Letters*, 98:087205, 2007. doi: 10.1063/1.2259813.

[26] Verba, R., Hierro-Rodriguez, A., Navas, D. et al. Spin-wave excitation modes in thick vortex-state circular ferromagnetic nanodots. *Physical Review B*, 93:214437, 2016. doi: 10.1103/PhysRevB.93.214437.

[27] Wintz, S., Tiberkevich, V., Weigand, M. et al. Magnetic vortex cores as tunable spin-wave emitters. *Nature Nanotechnology*, 11:948, 2016. doi: 10.1038/nnano.2016.117.

[28] Hämäläinen, S. J., Brandl, F., Franke, K. J. et al. Tunable Short-Wavelength Spin-Wave Emission and Confinement in Anisotropy-Modulated Multiferroic Heterostructures. *Physical Review Applied*, 8(1):1–9, 2017. doi: 10.1103/PhysRevApplied.8.014020.

[29] Van de Wiele, B., Hämäläinen, S. J., Baláž, P. et al. Tunable short-wavelength spin wave excitation from pinned magnetic domain walls. *Scientific Reports*, 6(21330), 2016. doi: 10.1038/srep21330.

[30] Berger, L. Emission of spin waves by a magnetic multilayer traversed by a current. *Physical Review B*, 54(13):9353, 1996. doi: 10.1103/PhysRevB.54.9353.

[31] Tsoi, M., Jansen, A., Bass, J. et al. Generation and detection of phase-coherent current-driven magnons in magnetic multilayers. *Nature*, 406(6791):46, 2000. doi: 10.1038/35017512.

[32] Tsoi, M. Phase-coherent current-driven magnons in magnetic multilayers. *Journal of Magnetism and Magnetic Materials*, 240:103–107, 2002. doi: 10.1016/S0304-8853(01)00716-8.

[33] Demidov, V. E., Urazhdin, S. and Demokritov, S. O. Direct observation and mapping of spin waves emitted by spin-torque nano-oscillators. *Nature Materials*, 9(12): 984, 2010. doi: 10.1038/nmat2882.

[34] Madami, M., Bonetti, S., Consolo, G. et al. Direct observation of a propagating spin wave induced by spin-transfer torque. *Nature Nanotechnology*, 6(10):635, 2011. doi: 10.1038/nnano.2011.140.

[35] Urazhdin, S., Demidov, V., Ulrichs, H. et al. Nanomagnonic devices based on the spin-transfer torque. *Nature Nanotechnology*, 9(7):509, 2014. doi: 10.1038/nnano.2014.88.

[36] Demidov, V., Urazhdin, S., De Loubens, G. et al. Magnetization oscillations and waves driven by pure spin currents. *Physics Reports*, 673:1–31, 2017. doi: 10.1016/j.physrep.2017.01.001.

[37] Demidov, V. E., Kostylev, M. P., Rott, K. et al. Excitation of short-wavelength spin waves in magnonic waveguides. *Applied Physics Letters*, 99(8):082507, 2011. doi: 10.1063/1.3631756.

[38] Sklenar, J., Bhat, V. S., Tsai, C. C. et al. Generating wave vector specific Damon-Eshbach spin waves in Py using a diffraction grating. *Applied Physics Letters*, 101 (5):052404, 2012. doi: 10.1063/1.4737438.

[39] Davies, C. S. and Kruglyak, V. V. Generation of propagating spin waves from edges of magnetic nanostructures pumped by uniform microwave magnetic field. *IEEE Transactions on Magnetics*, 52(7):1–4, 2016. doi: 10.1109/TMAG.2016.2517000.

[40] Sankey, J. C., Braganca, P. M., Garcia, A. G. F. et al. Spin-transfer-driven ferromagnetic resonance of individual nanomagnets. *Physical Review Letters*, 96(22): 227601, 2006. doi: 10.1103/PhysRevLett.96.227601.

[41] Petit, S., Baraduc, C., Thirion, C. et al. Spin-torque influence on the high-frequency magnetization fluctuations in magnetic tunnel junctions. *Physical Review Letters*, 98(7):077203, 2007. doi: 10.1103/PhysRevLett.98.077203.

[42] Ando, K., Ieda, J., Sasage, K. et al. Electric detection of spin wave resonance using inverse spin-Hall effect. *Applied Physics Letters*, 94(26):262505, 2009. doi: 10.1063/1.3167826.

[43] Borovik-Romanov, A. S. and Kreines, N. M. Brillouin-Mandelstam scattering from thermal and excited magnons. *Physics Reports*, 81(5):351–408, 1982. doi: 10.1016/0370-1573(82)90118-1.

[44] Vogt, K., Schultheiss, H., Hermsdoerfer, S. J. et al. All-optical detection of phase fronts of propagating spin waves in a Ni81Fe19 microstripe. *Applied Physics Letters*, 95(18):2012–2015, 2009. doi: 10.1063/1.3262348.

[45] Sebastian, T., Schultheiss, K., Obry, B. et al. Micro-focused Brillouin light scattering: imaging spin waves at the nanoscale. *Frontiers in Physics*, 3:35, 2015. doi: 10.3389/fphy.2015.00035.

[46] Au, Y., Ahmad, E., Dmytriiev, O. et al. Resonant microwave-to-spin-wave transducer. *Applied Physics Letters*, 100(18):182404, 2012. doi: 10.1063/1.4711039.

[47] Au, Y., Dvornik, M., Davison, T. et al. Direct excitation of propagating spin waves by focused ultrashort optical pulses. *Physical Review Letters*, 110(9):097201, 2013. doi: 10.1103/PhysRevLett.110.097201.

[48] Stenning, G., Shelford, L., Cavill, S. et al. Magnetization dynamics in an exchange-coupled NiFe/CoFe bilayer studied by x-ray detected ferromagnetic resonance. *New Journal of Physics*, 17(1):013019, 2015. doi: 10.1088/1367-2630/17/1/013019.

[49] Serga, A. A., Chumak, A. V. and Hillebrands, B. YIG magnonics. *Journal of Physics D: Applied Physics*, 43(26):264002, 2010. doi: 10.1088/0022-3727/43/26/264002.

[50] Vitko, V. V., Nikitin, A. A., Ustinov, A. B. et al. Investigation of spin waves in magnonic crystal based on periodically metallized YIG film. In *Journal of Physics: Conference Series*, volume 929, page 012027. IOP Publishing, 2017. doi: 10.1088/1742-6596/929/1/012027.

[51] Krysztofik, A., Głowiński, H., Kuświk, P. et al. Characterization of spin wave propagation in (111) YIG thin films with large anisotropy. *Journal of Physics D: Applied Physics*, 50(23):235004, 2017. doi: 10.1088/1361-6463/aa6df0.

[52] Woltersdorf, G., Kiessling, M., Meyer, G. et al. Damping by slow relaxing rare earth impurities in Ni80Fe20. *Physical Review Letters*, 102(25):257602, 2009. doi: 10.1103/PhysRevLett.102.257602.

[53] Chumak, A. V., Pirro, P., Serga, A. A. et al. Spin-wave propagation in a microstructured magnonic crystal. *Applied Physics Letters*, 95(26):262508, 2009. doi: 10.1063/1.3279138.

[54] Sebastian, T., Ohdaira, Y., Kubota, T. et al. Low-damping spin-wave propagation in a micro-structured Co2Mn0.6Fe0.4Si Heusler waveguide. *Applied Physics Letters*, 100(11):112402, 2012. doi: 10.1063/1.3693391.

[55] Stückler, T., Liu, C., Yu, H. et al. Spin wave propagation detected over 100μm in half-metallic Heusler alloy Co2MnSi. *Journal of Magnetism and Magnetic Materials*, 450:13–17, 2018. doi: 10.1016/j.jmmm.2017.09.074.

[56] Kostylev, M. á., Serga, A., Schneider, T. et al. Spin-wave logical gates. *Applied Physics Letters*, 87(15):153501, 2005. doi: 10.1063/1.2089147.

[57] Lee, K.-S. and Kim, S.-K. Conceptual design of spin wave logic gates based on a Mach–Zehnder-type spin wave interferometer for universal logic functions. *Journal of Applied Physics*, 104(5):053909, 2008. doi: doi.org/10.1063/1.2975235.

[58] Khitun, A., Bao, M., Wu, Y. et al. Logic devices with spin wave buses-an approach to scalable magneto-electric circuitry. *MRS Online Proceedings Library Archive*, 1067, 2008. doi: 10.1557/PROC-1067-B01-04.

[59] Cramer, J., Fuhrmann, F., Ritzmann, U. et al. Magnon detection using a ferroic collinear multilayer spin valve. *Nature Communications*, 9(1):1089, 2018. doi: 10.1038/s41467-018-03485-5.

[60] Wu, H., Huang, L., Fang, C. et al. Magnon Valve Effect between Two Magnetic Insulators. *Physical Review Letters*, 120(9):097205, 2018. doi: 10.1103/PhysRevLett.120.097205.

[61] Cornelissen, L. J., Liu, J., van Wees, B. J. et al. Spin-current-controlled modulation of the magnon spin conductance in a three-terminal magnon transistor. *Physical Review Letters*, 120(9):097702, 2018. doi: 10.1103/PhysRevLett.120.097702.

[62] Hubert, A. and Schäfer, R. *Magnetic Domains: The Analysis of Magnetic Microstructures*. New York: Springer, 2009. ISBN 978-3-540-64108-7. doi: 10.1007/978-3-540-85054-0.

[63] Skomski, R. *Simple Models of Magnetism*. Oxford: Oxford University Press, 2008. doi: 10.1093/acprof:oso/9780198570752.001.0001.

[64] Coey, J. M. D. *Magnetism and Magnetic Materials*. New York: Cambridge University Press, 2010. ISBN 978-0-521-81614-4.

[65] Chikazumi, S. and Graham, C. D. *Physics of Ferromagnetism*. Oxford: Oxford University Press, 1997. ISBN 0-19-851776-9.

[66] Landau, L. and Lifshitz, E. On the theory of the dispersion of magnetic permeability in ferromagnetic bodies. *Physikalische Zeitschrift der Sowjetunion*, 8:155–161, 1935.

[67] Mallinson, J. C. On damped gyromagnetic precession. *IEEE Transactions on Magnetics*, 23, 1987. doi: 10.1109/TMAG.1987.1065181.

[68] Barnett, S. and Kenny, G. Gyromagnetic Ratios of Iron, Cobalt, and Many Binary Alloys of Iron, Cobalt, and Nickel. *Physical Review*, 87(5):723, 1952. doi: 10.1103/PhysRev.87.723.

[69] Schwarze, T. *Spin waves in 2D and 3D magnonic crystals: From nanostructured ferromagnetic materials to chiral helimagnets*. Dissertation thesis, Technischen Universität München, 2013.

[70] Giesen, F. *Magnetization dynamics of nanostructured ferromagnetic rings and rectangular elements*. Dissertation thesis, Universität Hamburg, 2005.

[71] Kittel, C. On the theory of ferromagnetic resonance absorption. *Physical Review*, 73(2):155–161, 1948. doi: 10.1103/PhysRev.73.155.

[72] Bilzer, C. *Microwave susceptibility of thin ferromagnetic films: metrology and insight into magnetization dynamics*. Dissertation thesis, Université Paris Sud 11, 2007.

[73] Kalarickal, S. S., Krivosik, P., Wu, M. et al. Ferromagnetic resonance linewidth in metallic thin films: Comparison of measurement methods. *Journal of Applied Physics*, 99(9):093909, 2006. doi: 10.1063/1.2197087.

[74] Neusser, S. *Spin Waves in Antidot Lattices: From Quantization to Magnonic Crystals*. Dissertation thesis, Technischen Universität München, 2011.

[75] Stancil, D. D. and Prabhakar, A. *Spin waves: Theory and Applications*. New York: Springer, 2009. ISBN 978-0-387-77864-8. doi: 10.1007/978-0- 387-77865-5.

[76] Haghshenasfard, Z. *Linear and Nonlinear Dynamics of Spin Waves in Ferromagnetic Nanowires*. Dissertation thesis, The University of Western Ontario, 2017.

[77] Damon, R. W. and Eshbach, J. R. Magnetostatic modes of a ferromagnetic slab. *Journal of Applied Physics*, 31(5):104–105, 1960. doi: 10.1063/1.1984622.

[78] Demokritov, S. O. Dynamic eigen-modes in magnetic stripes and dots. *Journal of Physics: Condensed Matter*, 15(34):S2575, 2003. doi: 10.1088/0953-8984/15/34/307.

[79] Kraczyk, M. and Grundler, D. Review and prospects of magnonic crystals and devices with reprogrammable band structure. *Journal of Physics: Condensed Matter*, 26:123202, 2014. doi: 10.1088/0953-8984/26/12/123202.

[80] Gubbiotti, G., Tacchi, S., Carlotti, G. et al. Collective spin modes in monodimensional magnonic crystals consisting of dipolarly coupled nanowires. *Applied Physics Letters*, 90(9):092503, 2007. doi: 10.1063/1.2709909.

[81] Ulrichs, H., Lenk, B. and Münzenberg, M. Magnonic spin-wave modes in CoFeB antidot lattices. *Applied Physics Letters*, 97(9):092506, 2010. doi: 10.1063/1.3483136.

[82] Krawczyk, M. and Puszkarski, H. Plane-wave theory of three-dimensional magnonic crystals. *Physical Review B*, 77(5):054437, 2008. doi: 10.1103/PhysRevB.77.054437.

[83] Langer, M., Röder, F., Gallardo, R. et al. Role of internal demagnetizing field for the dynamics of a surface-modulated magnonic crystal. *Physical Review B*, 95(18): 184405, 2017. doi: 10.1103/PhysRevB.95.184405.

[84] Gubbiotti, G., Silvani, R., Tacchi, S. et al. Tailoring the spin waves band structure of 1D magnonic crystals consisting of L-shaped iron/permalloy nanowires. *Journal of Physics D: Applied Physics*, 50(10):105002, 2017. doi: 10.1088/1361-6463/aa59a4.

[85] Gulyaev, Y. V., Nikitov, S. A., Zhivotovskii, L. et al. Ferromagnetic films with magnon bandgap periodic structures: Magnon crystals. *Journal of Experimental and Theoretical Physics Letters*, 77(10):567–570, 2003. doi: 10.1134/1.1595698.

[86] Chumak, A., Serga, A., Hillebrands, B. et al. Scattering of backward spin waves in a one-dimensional magnonic crystal. *Applied Physics Letters*, 93(2):022508, 2008. doi: 10.1063/1.2963027.

[87] Chumak, A., Serga, A., Wolff, S. et al. Design and optimization of one-dimensional ferrite-film based magnonic crystals. *Journal of Applied Physics*, 105(8):083906, 2009. doi: 10.1063/1.3098258.

[88] Lee, K.-S., Han, D.-S. and Kim, S.-K. Physical origin and generic control of magnonic band gaps of dipole-exchange spin waves in width-modulated nanostrip waveguides. *Physical Review Letters*, 102(12):127202, 2009. doi: 10.1103/PhysRevLett.102.127202.

[89] Xiong, L., Kostylev, M. and Adeyeye, A. Magnetization dynamics of Ni80Fe20 nanowires with continuous width modulation. *Physical Review B*, 95(22):224426, 2017. doi: 10.1103/PhysRevB.95.224426.

[90] Nikitov, S., Tailhades, P. and Tsai, C. Spin waves in periodic magnetic structures—magnonic crystals. *Journal of Magnetism and Magnetic Materials*, 236(3): 320–330, 2001. doi: 10.1016/S0304-8853(01)00470-X.

[91] Wang, Z. K., Zhang, V. L., Lim, H. S. et al. Nanostructured magnonic crystals with size-tunable bandgaps. *ACS Nano*, 4(2):643–648, 2010. doi: 10.1021/nn901171u.

[92] Ciubotaru, F., Chumak, A. V., Obry, B. et al. Magnonic band gaps in waveguides with a periodic variation of the saturation magnetization. *Physical Review B*, 88: 134406, 2013. doi: 10.1103/PhysRevB.88.134406.

[93] Obry, B., Pirro, P., Brächer, T. et al. A micro-structured ion-implanted magnonic crystal. *Applied Physics Letters*, 102(20):202403, 2013. doi: 10.1063/1.4807721.

[94] Vogel, M., Chumak, A. V., Waller, E. H. et al. Optically reconfigurable magnetic materials. *Nature Physics*, 11(6):487, 2015. doi: 10.1038/nphys3325.

[95] Wang, Q., Chumak, A. V., Jin, L. et al. Voltage-controlled nanoscale reconfigurable magnonic crystal. *Physical Review B*, 95(13):134433, 2017. doi: 10.1103/PhysRevB.95.134433.

[96] Kumar, N. and Prabhakar, A. Resonant spin wave excitations in a magnonic crystal cavity. *Journal of Magnetism and Magnetic Materials*, 450:46–50, 2018. doi: 10.1016/j.jmmm.2017.06.009.

[97] Kryshtal, R. and Medved, A. Influence of magnetic anisotropy on dynamic magnonic crystals created by surface acoustic waves in yttrium iron garnet films. *Journal of Magnetism and Magnetic Materials*, 426:666–669, 2017. doi: 10.1016/j.jmmm.2016.10.148.

[98] Wang, D., Zhou, Y., Li, Z.-x. et al. Magnonic band structure of domain wall magnonic crystals. *IEEE Transactions on Magnetics*, 53(3):1–10, 2017. doi: 10.1109/TMAG.2016.2633238.

[99] Vasseur, J., Dobrzynski, L., Djafari-Rouhani, B. et al. Magnon band structure of periodic composites. *Physical Review B*, 54(2):1043, 1996. doi: 10.1103/PhysRevB.54.1043.

[100] Wen, C. P. Coplanar waveguide: A surface strip transmission line suitable for nonreciprocal gyromagnetic device applications. *IEEE Transactions on Microwave Theory and Techniques*, 17(12):1087–1090, 1969. doi: 10.1109/TMTT.1969.1127105.

[101] Counil, G., Kim, J.-V., Devolder, T. et al. Spin wave contributions to the high-frequency magnetic response of thin films obtained with inductive methods. *Journal of Applied Physics*, 95(10):5646–5652, 2004. doi: 10.1063/1.1697641.

[102] Kennewell, K., Kostylev, M. and Stamps, R. Calculation of spin wave mode response induced by a coplanar microwave line. *Journal of Applied Physics*, 101(9):09D107, 2007. doi: 10.1063/1.2710068.

[103] Yu, H., Kelly, O. d., Cros, V. et al. Magnetic thin-film insulator with ultra-low spin wave damping for coherent nanomagnonics. *Scientific Reports*, 4:6848, 2014. doi: 10.1038/srep06848.

[104] Qin, H., Hämäläinen, S. J. and van Dijken, S. Exchange-torque-induced excitation of perpendicular standing spin waves in nanometer-thick YIG films. *Scientific Reports*, 8(1):5755, 2018. doi: 10.1038/s41598-018-23933-y.

[105] Kittel, C. *Introduction to Solid State Physics*. New York: John Wiley, 1996. ISBN 0-471-11181-3.

[106] Jesser, W. A. and Matthews, J. W. Evidence for pseudomorphic growth of iron on copper. *Philosophical Magazine*, 15(138):1097–1106, 1967. doi: 10.1080/14786436708222752.

[107] Macedo, W. A. A. and Keune, W. Magnetism of epitaxial fcc-Fe (100) films on Cu (100) investigated in situ by conversion-electron Mössbauer spectroscopy in ultrahigh vacuum. *Physical Review Letters*, 61(4):475, 1988. doi: 10.1103/PhysRevLett.61.475.

[108] Kalki, K., Chambliss, D. D., Johnson, K. E. et al. Evidence for martensitic fcc-bcc transition of thin Fe films on Cu (100). *Physical Review B*, 48(24):18344, 1993. doi: 10.1103/PhysRevB.48.18344.

[109] Rupp, W., Biedermann, A., Kamenik, B. et al. Ion-beam induced fcc-bcc transition in ultrathin Fe films for ferromagnetic patterning. *Applied Physics Letters*, 93(6): 063102, 2008. doi: 10.1063/1.2969795.

[110] Tournerie, N., Schieffer, P., Lépine, B. et al. In-plane magnetic anisotropies in epitaxial Fe (001) thin films. *Physical Review B*, 78(13):134401, 2008. doi: 10.1103/PhysRevB.78.134401.

[111] Biedermann, A., Schmid, M. and Varga, P. Nucleation of bcc Iron in Ultrathin fcc Films. *Physical Review Letters*, 86(3):464, 2001. doi: 10.1103/PhysRevLett.86.464.

[112] Biedermann, A., Tscheließnig, R., Schmid, M. et al. Crystallographic structure of ultrathin Fe films on Cu(100). *Physical Review Letters*, 87(8):086103, 2001. doi: 10.1103/PhysRevLett.87.086103.

[113] Biedermann, A., Tscheliessnig, R., Schmid, M. et al. Local atomic structure of ultra-thin Fe films grown on Cu (100). *Applied Physics A*, 78(6):807–816, 2004. doi: 10.1007/s00339-003-2435-7.

[114] Zaman, S. S. *Ion-beam induced magnetic nano-structures of Fe grown on Cu(100)*. Dissertation thesis, Technische Universität Wien, 2011.

[115] Biedermann, A., Tscheliessnig, R., Klein, C. et al. Reconstruction of the clean and H covered "magnetic live surface layer" of Fe films grown on Cu(100). *Surface Science*, 563(1-3):110–126, 2004. doi: 10.1016/j.susc.2004.06.150.

[116] Kirilyuk, A., Giergiel, J., Shen, J. et al. Growth of stabilized γ-Fe films and their magnetic properties. *Physical Review B*, 54(2):1050, 1996. doi: 10.1103/PhysRevB.54.1050.

[117] Zaman, S. S., Oßmer, H., Jonner, J. et al. Ion-beam-induced magnetic transformation of CO-stabilized fcc Fe films on Cu(100). *Physical Review B*, 82(23):235401, 2010. doi: 10.1103/PhysRevB.82.235401.

[118] Gloss, J. *Magnetic transformation of metastable fcc Fe/Cu(100) films by focused ion beam*. Diploma thesis, Brno University of Technology, 2014.

[119] Crangle, J. and Hallam, G. The magnetization of face-centred cubic and body-centred cubic iron + nickel alloys. *Proceedings of the Royal Society of London A*, 272(1348):119–132, 1963. doi: 10.1098/rspa.1963.0045.

[120] Entel, P., Hoffmann, E., Mohn, P. et al. First-principles calculations of the instability leading to the Invar effect. *Physical Review B*, 47(14):8706, 1993. doi: 10.1103/PhysRevB.47.8706.

[121] Křižáková, V. *Magnetic properties of materials based on metastable FeNi thin films*. Bachelor thesis, Brno University of Technology, 2016. (In Czech).

[122] Chang, C.-A. Outdiffusion of Cu through Au: Comparison of (100) and (111) Cu films epitaxially deposited on Si, and effects of annealing ambients. *Applied Physics Letters*, 55(26):2754–2756, 1989. doi: 10.1063/1.101944.

[123] Chang, C.-A., Liu, J. C. and Angilello, J. Epitaxy of (100) Cu on (100) Si by evaporation near room temperatures: In-plane epitaxial relation and channeling analysis. *Applied Physics Letters*, 57(21):2239–2240, 1990. doi: 10.1063/1.103902.

[124] Liu, C. and Chen, L. Effects of substrate cleaning and film thickness on the epitaxial growth of ultrahigh vacuum deposited Cu thin films on (001) Si. *Applied Surface Science*, 92:84–88, 1996. doi: 10.1016/0169-4332(95)00208-1.

[125] Hashim, I., Park, B. and Atwater, H. Epitaxial growth of Cu (001) on Si (001): Mechanisms of orientation development and defect morphology. *Applied Physics Letters*, 63(20):2833–2835, 1993. doi: 10.1063/1.110302.

[126] Demczyk, B., Naik, R., Auner, G. et al. Growth of Cu films on hydrogen terminated Si (100) and Si (111) surfaces. *Journal of Applied Physics*, 75(4):1956–1961, 1994. doi: 10.1063/1.356344.

[127] Horký, M. *Growth of metastable fcc Fe thin films on Cu(100)/Si(100) substrates.* Diploma thesis, Brno University of Technology, 2016. (In Czech).

[128] Shi, M., Wang, Y. and Rabalais, J. Structure of hydrogen on the Si {100} surface in the (2× 1)-H monohydride,(1× 1)-H dihydride, and c (4× 4)-H phases. *Physical Review B*, 48(3):1689, 1993. doi: 10.1103/PhysRevB.48.1689.

[129] Cooil, S. P., Mazzola, F., Klemm, H. W. et al. In Situ Patterning of Ultrasharp Dopant Profiles in Silicon. *ACS Nano*, 11(2):1683–1688, 2017. doi: 10.1021/acsnano.6b07359.

[130] Meunier, A., Gilles, B. and Verdier, M. Cu/Si(001) epitaxial growth: role of the epitaxial silicide formation in the structure and the morphology. *Journal of Crystal Growth*, 275(1-2):e1059–e1065, 2005. doi: 10.1016/j.jcrysgro.2004.11.132.

[131] Francis, A. J., Cao, Y. and Salvador, P. A. Epitaxial growth of Cu (100) and Pt (100) thin films on perovskite substrates. *Thin Solid Films*, 496(2):317–325, 2006. doi: 10.1016/j.tsf.2005.08.367.

[132] Warusawithana, M. P., Cen, C., Sleasman, C. R. et al. A ferroelectric oxide made directly on silicon. *Science*, 324(5925):367–370, 2009. doi: 10.1126/science.1169678.

[133] Hoff, H., Waytena, G., Glesener, J. et al. Critical thickness of single crystal fcc iron on diamond. *Surface science*, 326(3):252–266, 1995. doi: 10.1016/0039-6028(94)00787-X.

[134] Davies, C. S. and Kruglyak, V. Graded-index magnonics. *Low Temperature Physics*, 41(10):760–766, 2015. doi: 10.1063/1.4932349.

[135] Ashida, K., Kutsuma, Y. and Kaneko, T. Quantitative observation of low energy electron channeling contrast from sub-nanometer thick surface layers using hexagonal Silicon Carbide single crystal. In *European Microscopy Congress 2016: Proceedings*. Wiley Online Library, 2016. doi: 10.1002/9783527808465.EMC2016.5371.

[136] Flajšman, L., Urbánek, M., Křižáková, V. et al. High-resolution fully vectorial scanning Kerr magnetometer. *Review of Scientific Instruments*, 87(5):053704, 2016. doi: 10.1063/1.4948595.

[137] Urbánek, M., Flajšman, L., Křižáková, V. et al. Focused ion beam direct writing of magnetic patterns with controlled structural and magnetic properties. *ArXiv e-prints*, 2018. URL `https://arxiv.org/abs/1803.04348`.

[138] Gladii, O., Halley, D., Henry, Y. et al. Spin-wave propagation and spin-polarized electron transport in single-crystal iron films. *Physical Review B*, 96(17):174420, 2017. doi: 10.1103/PhysRevB.96.174420.

[139] Demidov, V. E., Urazhdin, S., Liu, R. et al. Excitation of coherent propagating spin waves by pure spin currents. *Nature Communications*, 7:10446, 2016. doi: 10.1038/ncomms10446.

[140] Wojewoda, O. *Disperzní relace magnonických krystalů s netriviální prostorovou distribucí magnetické anizotropie*. Bachelor thesis, Brno University of Technology, 2018. (In Czech).

[141] Vansteenkiste, A., Leliaert, J., Dvornik, M. et al. The design and verification of MuMax3. *AIP Advances*, 4(10):107133, 2014. doi: 10.1063/1.4899186.

List of abbreviations

AFM	atomic force microscopy
bcc	body-centered-cubic
dc	direct current
CPW	coplanar waveguide
DE	Damon-Eshbach
DUT	device under test
EBL	electron beam lithography
FFT	fast Fourier transform
fcc	face-centered-cubic
FIB	focused ion beam
FMR	ferromagntic resonance
FWHM	full width at half maximum
GGG	gallium gadolinium garnet
hf	high-frequency
IPA	isopropyl alcohol
LEED	low-energy electron diffraction
MC	magnonic crystal
ML	monolayer
MOKE	magneto-optical Kerr effect
MSBVW	magnetostatic backward volume wave
MSFVW	magnetostatic forward volume wave
MSSW	magnetostatic surface wave
PMMA	Poly methyl methacrylate
PSSW	perpendicular standing spin wave
PSWS	propagating spin-wave spectroscopy
QCM	quartz crystal microbalance
SEM	scanning electron microscopy
SMA	SubMiniature version A
SOLT	Short-Open-Load-Match
SOLR	Short-Open-Load-Reciprocal
SW	spin-wave
UHV	ultra-high vacuum
TOSM	Through-Open-Short-Match
TRL	Through-Reflect-Line
TUW	Technische Universität Wien
VNA	vector network analyzer
XPS	X-ray photoelectron spectroscopy
YIG	yttrium iron garnet

A Vector network analyzer calibration

A.1 Calibration techniques

For the characterization of a device under test, the magnitude and the phase of incident and outgoing waves are inspected by a VNA. By the measurement of the wave properties, the VNA resolves many electric characteristics of the DUT including the impedance, group delay or losses. Nevertheless, the accuracy of the output parameters is a subject to the accuracy with which the VNA measures the magnitude and the phase relation of the incident and outgoing waves. As the measurement depends on the measurement setup itself, calibration information is necessary for the proper performance, especially when a highly precise characterization is demanded.

The main contribution to the uncertainties is a variation of the laboratory conditions and the measurement configuration such as temperature, frequency, DUT interconnection, length of the cables between the VNA and the DUT and so on. Another major source of imperfections is related with inherent instrument impairments. They are caused by four main contributions: port match, frequency response, directivity and isolation. All of them are in detail described in Ref. [4]. The vast majority of these systematic errors can be eliminated by the calibration process.

As there is a vast range of impairments, there also are many ways how to realize the VNA calibration. In accordance with the measurement settings, types of ports of the DUT or available calibration standards, different calibration methods varying in time requirements and accuracy can be used. Common types of a two-port VNA calibration include the frequency response calibration, the one-path two-port calibration and the full S-parameter calibration. The first one is the easiest, fastest and a reasonably accurate method, the second one provides better accuracy and allows wider measurement range. The last type is the most used and the most precise of them all. It provides the correction of all the S-parameters and employs various calibration techniques, of which we describe two in detail.

The SOLT (*Short-Open-Load-Through*) calibration, which is sometimes referred to as the TOSM (*Through-Open-Short-Match*) calibration, is the most common technique for the VNA calibration. It relies on the measurement of well-known calibration standards connected to both ports. The calibration procedure is simple when dealing with a DUT with mating connectors. Then, both ports can be directly connected, which results in a zero-length Through. However, when a DUT with connectors of the same gender or with different type of connectors is used (i.e. a non-insertable device), the calibration is bit more complex. Either a phase-equal adapters have to be used for the calibration, or another method based on the use of a Reciprocal through is employed. This is the SOLR (*Short-Open-Load-Reciprocal*) calibration, known also as a calibration by *Unknown Thru*. Nevertheless, there is an additional requirement of reciprocity ($S_{21} = S_{12}$) placed upon the Through standard. During the SOLR process, first a one-port calibration is carried out at each port using the Short, Open, and Load standards. Then, the S-parameters are estimated from forward and reverse measurements using the Through. The SOLR

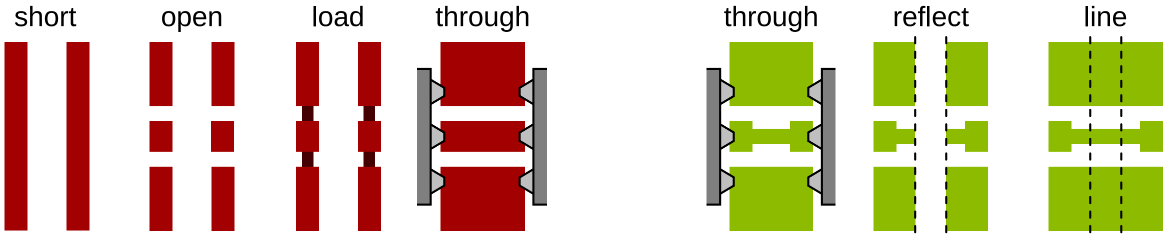

Fig. A.1: A schematics of the calibration standards for two-port methods: SOLT and TRL calibration. Emplacement of contact probes of both ports is illustrated in the through lines. Reference planes in case of the TRL calibration are indicated by dashed line.

technique is also useful for an *on-wafer* calibration, if the prepared Through line is anyhow bended.

Another popular technique is the TRL (*Through-Reflect-Line*) calibration. It is widely used for the on-wafer measurements, where instead of highly precise calibration standards, rather a lithographically prepared calibration set is used. The Through is formed by a zero-length strip directly connecting both ports, the Reflect is a common open circuit between the ports and the Line is non-zero-length strip. A disadvantage of the TRL technique is a narrow frequency range in which it can be used. The range is given by the length of the Line. In order to extend the range, more Lines need to be utilized for successive calibrations. Such calibration technique is referred to as the multi-line TRL.

Schematics of the calibration standards used for both of the described techniques is presented in Fig. A.1. Thorough description of other calibration types and associated processes can be found in Ref. [4].

When the calibration of the VNA is completed, it is important to avoid any changes of the hardware and to keep the software setting the same for the measurement of the DUT. To preserve the calibration valid, all the measurement settings also need to be kept constant. They include the start and stop frequency, number of measured frequency points, frequency bandwidth, averaging, source power and settings of the receiver step attenuators. Therefore, it is often recommended to perform a test measurement to adjust all the parameters prior the calibration process.

A.2 On-wafer calibration

In case the probe station is incorporated into the experimental setup, it is advantageous to use the on-wafer calibration standards rather than the calibration kit, which requires dismounting of the probes and connecting of the standards to connectors of the cables.

Therefore, we provide the on-wafer SLOT calibration standards with each series of our CPWs. The calibration is prepared within the same lithographic process (described in Sec. 3.3) as are the waveguides. The only difference with the described procedure is omitting the deposition of the insulation layer, which has to be from obvious reasons absent. The optical micrographs of the calibration standard representatives can be seen in Fig. A.2. The line of the Load is designed to have 50 Ω between the signal and the ground pads.

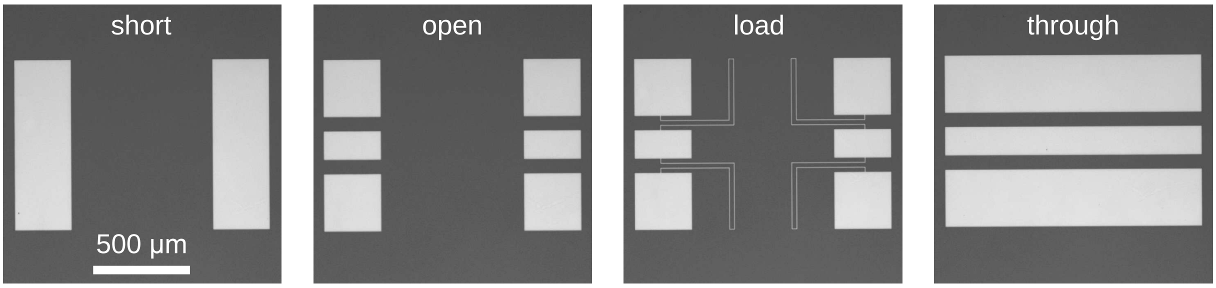

Fig. A.2: Optical micrographs of a series of the on-wafer SLOT calibration standards prepared using the EBL technique. The probe signal-to-ground pitch is 150 µ.

B Measured spin wave spectra

B.1 Broadband ferromagnetic resonance in ferromagnetic films

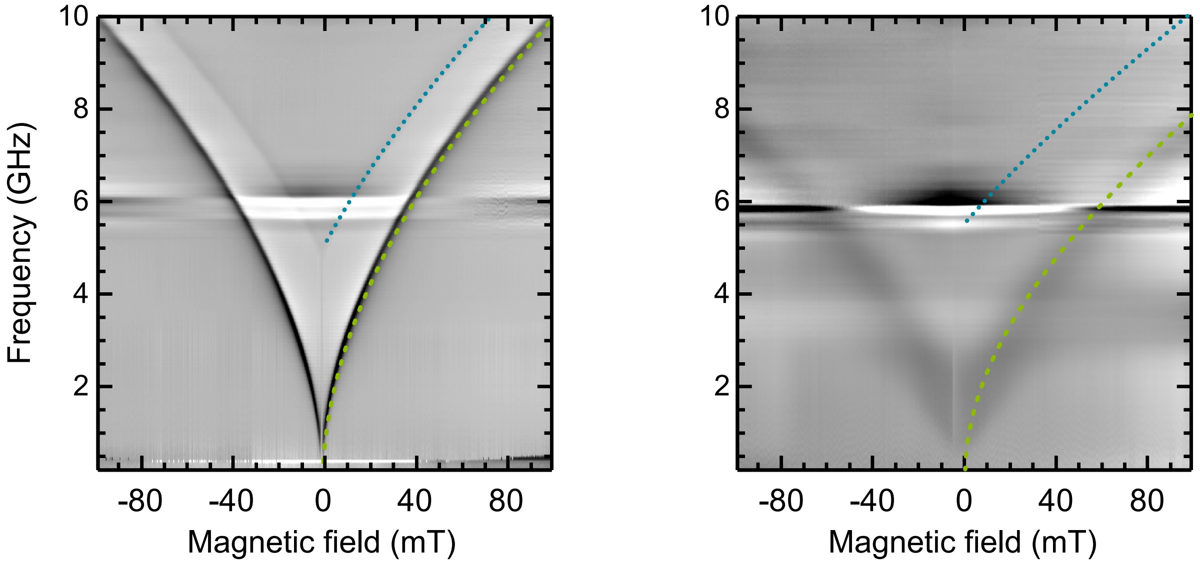

(a) 100 nm Permalloy/Si (b) 100 nm Ni/Si

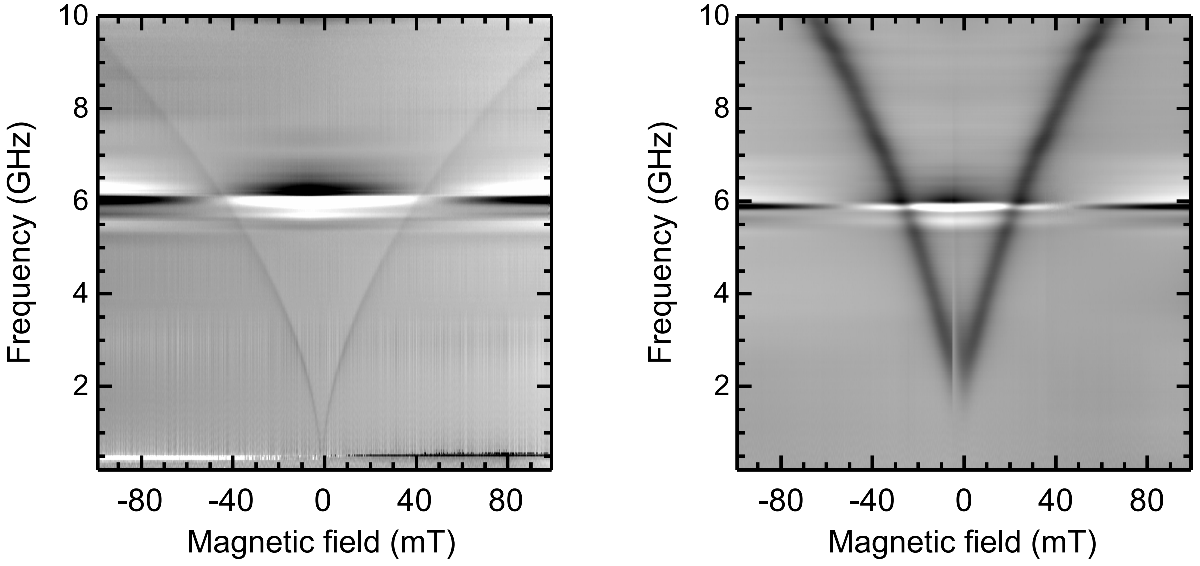

(c) 8 nm Permalloy/Si (d) 8 nm Fe/Si

Fig. B.1: Comparison of broadband FMR spectra of selected ferromagnetic materials. The dashed (green) line in the plots (a) and (b) indicates an analytical model of the FMR according to Eq. 1.23 with the literature values of M_S and γ. The dotted (blue) line indicates the modeled PSSW (Eq. 1.35) of the order $p = 1$. This mode with the zero-field frequency of 4.9 GHz is visible in the plot (a) and it cannot be observed in (b).

B.2 Propagating spin waves in YIG

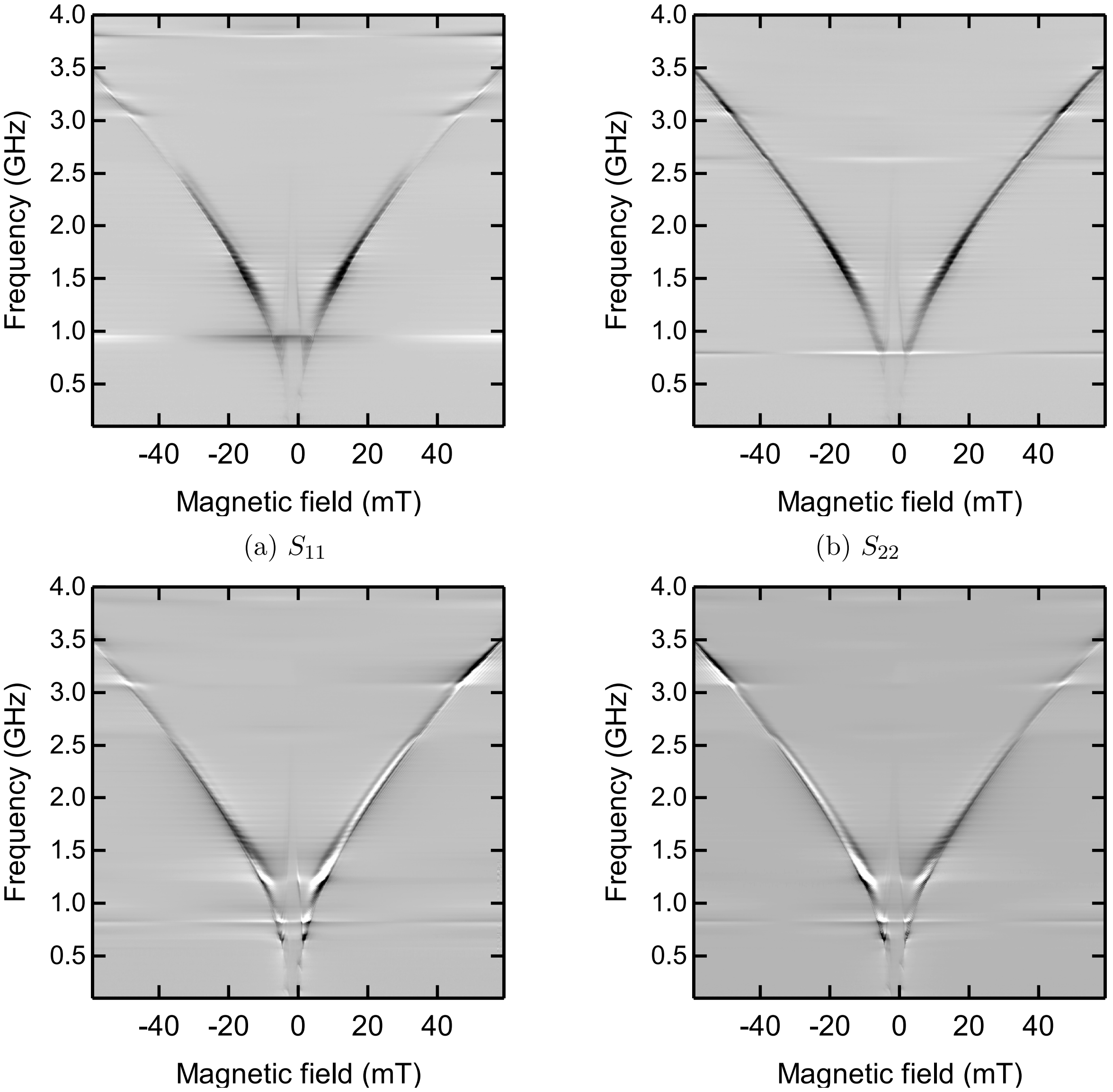

(a) S_{11} (b) S_{22}

(c) S_{21} (d) S_{12}

Fig. B.2: PSWS spectra in DE geometry of YIG film with the thickness of $t = 6\,\mu\text{m}$ grown on a GGG(111) substrate. The comparison shows spectra of SWs excited and detected by each of the VNA ports. In the ΔS_{21} and ΔS_{12} can be seen a difference between the positive and the negative halves of the map. When observed in more detail, the spectra look mirrored around the zero-field. This can be attributed to the surface character of the DE modes. A SW excited by the antenna at port 1 (left) propagates toward the antenna at port 2 along one of the YIG interfaces depending on the orientation of the bias field. Conversely, the SW excited by the other antenna (right) propagates in the same bias field along the other interface. A different quality of both interfaces then leads to a slight modification of the peak shape.

B.3 Characteristics of spin waves propagating in Permalloy film

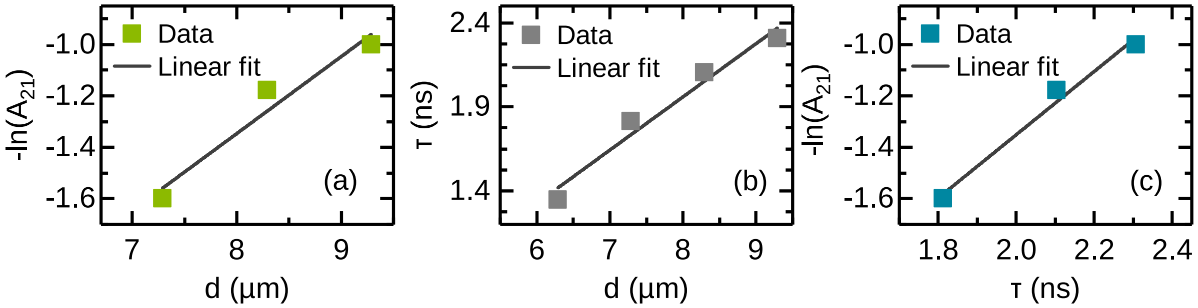

Fig. B.3: SW characteristics extracted from PSWS measurements of 100 nm thick Permalloy film. A dependence (a) of the logarithm of the normalized signal amplitude A_{21} on the signal-to-signal distance d providing δ^{-1}, a dependence (b) of the propagation time τ on the d providing a v_g^{-1} and a dependence (c) of the logarithm of A_{21} on the τ providing the value of Γ. The values extracted at 38 mT are: $\delta = (3.3\pm0.6)$ µm, $v_g = (3.2\pm0.4)$ km/s and $\Gamma = (11.3\pm1.6)\times10^8$ rad/s.

B.4 Propagating spin waves in metastable thin film

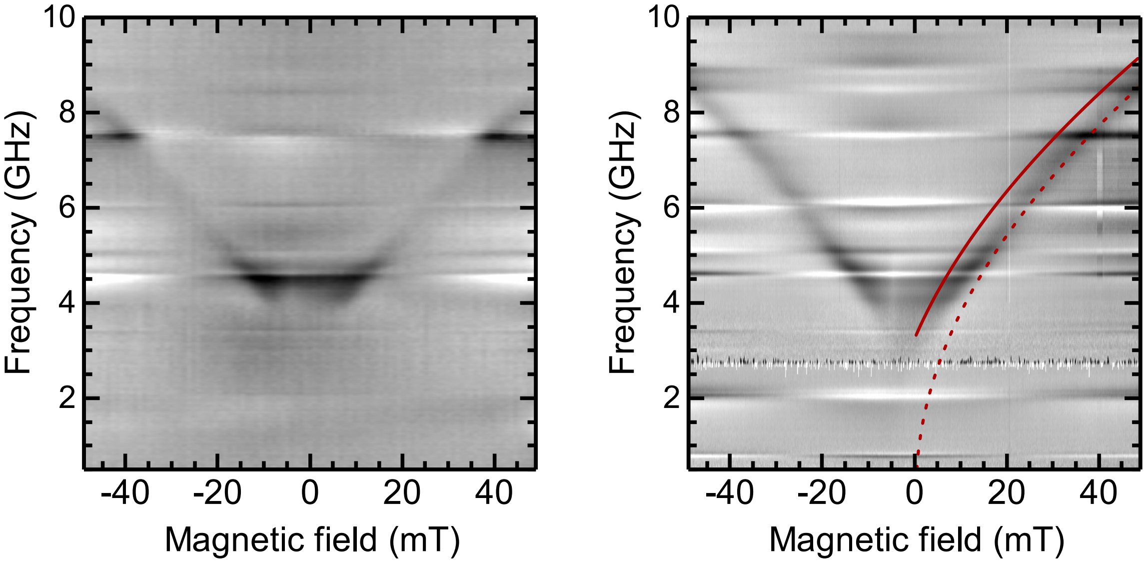

(a) ΔS_{11}

(b) ΔS_{21}

Fig. B.4: MSSW spectra of continuous FIB-transformed FeNi film with the thickness of 8 nm grown on an H-Si substrate. The SW spectra are obtained using a CPW pair from series b with the $d = 5.96$ µm. Red line indicates analytical calculation of MSSW propagating in the film characterized by the experimentally obtained parameters (Tab. 4.1). Dashed (red) line indicates the position of FMR peak for the same film.